IN-VIVO MEASUREMENT OF SKIN IRON CONCENTRATION BY X-RAY FLUORESCENCE

Designing and Evaluating a ^{109}Cd based XRF System For Skin Iron Measurements: A Validation Study in Normal and Iron Overload Conditions

By

Sami Ullah Khan Bangash,

MSc, MS.

A Thesis Submitted to the Department of Physics & Astronomy

and the School of Graduate Studies

of McMaster University

in Partial Fulfilment of the Requirements

for the Degree of

Doctor of Philosophy

TITLE: Designing and Evaluating a ^{109}Cd based XRF System For Skin Iron Measurements: A Validation Study in Normal and Iron Overload Conditions

AUTHOR: Sami Ullah Khan Bangash

MS. Radiation Sciences - Medical Physics

M.Sc. Physics

SUPERVISORS: Dr. Michael Farquharson & Dr. Fiona E. McNeill

COMMITTEE: Dr. Michelle Zeller & Dr. Bruce Charles Wainman

NUMBER OF PAGES: xi, 114

Abstract

The health impact of iron (Fe) deficiency or excess on the human body can be severe. Existing clinical methods for assessing body Fe levels have limitations. This thesis focuses on the potential of measuring skin Fe concentrations using X-ray Fluorescence (XRF) to assess body Fe levels. A portable XRF instrument based on a silicon drift detector has been developed. The instrument was calibrated using water-based phantoms, achieving a minimum detection limit of 1.35 ± 0.35 ppm (Fe) with a measurement time of 1800 s and a radiation dose of 1.1 ± 0.1 mSv to the skin surface.

The system accuracy was tested by measuring the skin Fe concentrations in 10 pig skin samples that were not loaded with Fe. The measured pig skin Fe ranged from approximately 8 to 14 ppm with an average value of 11 ppm. The XRF measurements were found to compare well with the results from Inductively Coupled Plasma Mass Spectroscopy (ICP-MS) analysis of the same skin samples. The mean difference between the Fe levels as assessed by XRF and ICP-MS was not significant, measuring at 2.5 ± 4.6 ppm.

Synchrotron μXRF mapping of 25 μm thick pig skin sections at a spatial resolution of 20 μm revealed Fe 'hot spots' through the skin, predominantly in the dermis, that were attributed to small blood vessels. The synchrotron map also showed that the Fe distribution in the skin peaks near the outer skin surface. Measurements by the system of this skin distribution were modelled using the Monte Carlo code EGS5 and indicated that if a highly elevated Fe layer is present at the surface, correction factors may be necessary for accurate estimation of skin surface Fe levels by the XRF system.

The performance of the system was tested using rat skin samples obtained from animals dosed *in vivo* with varying amounts of Fe. The system was able to distinguish between skin samples from normal rats and rats dosed with 80 mg Fe^{2+} and between rats dosed with 80 mg Fe^{2+} and 160 mg Fe^{2+} ($p = 0.001$ and $p=0.002$, respectively). The instrument also exhibited a significant linear relationship between the measured rat skin Fe concentration

and rat Fe dose (R^2 = 0.84, $p < 0.0001$). Furthermore, the measurements were validated against a laboratory XRF system, a bulk tissue measurement system ($R^2 = 0.85$, $p < 0.0001$). Overall, the work in this thesis highlights the promise of using portable XRF for precise and non-intrusive measurement of skin Fe levels in both Fe overload and Fe deficiency conditions.

Acknowledgements

I would like to express my heartfelt gratitude to Dr. Michael Farquharson and Dr. Fiona McNeill, with whom I have had the privilege of working closely over the past five years. Their unwavering guidance and support have been instrumental in shaping every aspect of my research journey, from the initial stages to the completion of my thesis. I am truly fortunate to have had such dedicated mentors who have played a significant role in my academic journey.

I am also grateful to Dr. David Chettle for his encouragement and for giving me the opportunity to start my research in his lab. His confidence in my abilities played a pivotal role in setting the foundation for my work.

I extend my gratitude to Dr. Soo Hyun Byun, who provided guidance on conducting Monte Carlo simulations, a critical component of this project.

Special thanks to Committee members Dr. Bruce Wainman and Dr. Michelle Zeller, whose expertise in iron physiology, skin structure, and clinical instrument utilization significantly enriched my understanding. Their insightful guidance has been invaluable throughout this academic venture.

A heartfelt thank you to my wife, Saher, who has been my pillar of strength, standing by me through the challenges of the academic journey. She has been with me through all the ups and downs, caring for our kids despite her demanding job.

I am indebted to my parents for their consistent support and guidance throughout my life. I fondly remember my mother (late) and her enduring encouragement to strive for excellence and pursue higher studies. Her love and guidance remain with me, and I wish she could be here to witness the completion of this thesis.

At the end I express my gratitude to my colleagues and lab mates, Erica, Bobby, Michelle, and Justin. I appreciate Erica and Michelle for serving as my editors during certain stages of my PhD. Special thanks to Bobby for assisting me in the preparation of rat skin samples. A particular acknowledgment goes to Justin, whose assistance was crucial in obtaining the printed phantoms and the aluminum window for the detector.

Declaration of Academic Achievement

I affirm that every contribution presented in this thesis is my original work, free from plagiarism or academic dishonesty.

I have thoroughly reviewed this thesis, and in my judgment, it meets the necessary standards in both scope and quality as a dissertation deserving the degree of Doctor of Philosophy.

Contents

List of Figures

Chapter 1

Introduction

1.1 RESEARCH MOTIVATION

Fe overload and Fe deficiency are common disorders globally, with over 1 billion people worldwide suffering from Fe disorders, including hemochromatosis and beta thalassemia [1]. Hemochromatosis is a disorder in which the body absorbs too much Fe from the intestine, affecting 1 in every 327 individuals [2]. There is an increase in the prevalence of beta thalassemia in North America due to the immigration of people from high prevalence regions [3], [4]. In this disease, the body does not produce enough hemoglobin, causing anemia. Beta thalassemia patients require multiple blood for treatment. However, these transfusions may result in excessive Fe accumulation in the body, which can affect vital organs and potentially cause organ damage. Consequently, chelation therapy (a treatment that uses medicine to remove Fe through urine or feces) is used as a preventive measure to manage Fe overload in these patients. It is important to note that chelation therapy's effectiveness depends on administering the correct amount of drug at the appropriate time, as excessive use of chelators can lead to Fe deficiency. Therefore, accurate measurement of Fe levels is imperative for the early detection and effective treatment of Fe disorders. The current clinical methods available for Fe measurement have certain limitations, highlighting the need for a technique that can accurately assess Fe overload.

The work presented in this thesis assumes that skin Fe concentration can be correlated with the total body Fe burden [5]–[7]. The project’s primary objective was to develop a system for measuring Fe overload through the analysis of skin Fe concentration using X-ray fluorescence (XRF) analysis.

The following sections describe concepts and provide information that may be useful to understanding this thesis' work.

1.2 REGULATION OF IRON IN THE HUMAN BODY

Fe is an essential element needed by the body for many physiological reactions. Fe's ability to easily gain and lose electrons is crucial for chemical reactions in cells. It is a transition metal and exhibits variable oxidation states, +2 and +3, allowing it to participate in redox reactions, DNA synthesis and repair, and other cell reactions [8]. Fe is a critical component of hemoglobin, a protein in red blood cells that carries oxygen to all parts of the body. Fe in hemoglobin binds it to oxygen in the lungs and releases the oxygen in the body where it is needed [9]. Approximately two-thirds of the Fe body burden is in hemoglobin, while the remaining is in the liver, bone marrow and muscles [10].

While Fe is essential in the human body, it is also important that levels are balanced. Excess Fe in the body damages cells and leads to critical organ failures, such as to the liver, heart and endocrine glands [11]. Since there is no specific mechanism for Fe excretion in the body, the liver stores excess Fe in a protein called ferritin [12]. Ferritin releases Fe from the liver in a controlled manner when it is needed for various physiological processes, such as the production of red blood cells or when the Fe is signalled as being deficient. The absorption of Fe from the intestine is controlled by hepcidin, a hormone secreted by the liver. Hepcidin reduces Fe absorption from the intestine by degrading ferroportin (a protein that transports Fe), thus controlling dietary Fe absorption. Similarly, hepcidin regulates the release of Fe from ferritin and other storage sites by the degradation of ferroportin on the surface of these cells [13]. Therefore, a balanced level of hepcidin is vital for regulating Fe in the body.

There are Fe disorders that lead to reduced body hepcidin levels and, eventually, Fe overload disease. These are discussed in the following sections.

1.2.1 Fe Overload Disorders

Hereditary Hemochromatosis

One of the most common examples of primary Fe overload disease is Hereditary Hemochromatosis (HHC), in which the body absorbs too much Fe from food. The classic presentation of HHC is usually due to a mutation in the Homeostatic Fe Regulator Protein Code Gene (HFE) on chromosome 6, which plays a role in hepcidin production [14]. These mutations can lead to reduced hepcidin levels, thus increasing Fe absorption from the diet. This disease is usually asymptomatic in the early stages. The clinical observation of patients with serious classic symptoms, such as diabetes, bronze skin and bronze diabetes, are sporadic. The most common symptoms are lethargy, weakness and arthralgias [15]. However, in the later stages of the disease, damage to critical organs such as the liver, heart and pancreas can occur. In the liver, Fe overload causes cirrhosis and is also one of the causes of hepatocellular carcinoma. Approximately six percent of patients with HHC ultimately develop hepatocellular carcinoma [15]. HHC causes irregular heartbeat, cardiomyopathy and heart failure [16]. The primary treatment of HHC is phlebotomy. Phlebotomy involves the removal of blood from the body, usually once a week, to lower the Fe level in the body [17].

Beta Thalassemia

Beta thalassemia is an inherited disease in which the body's ability to produce hemoglobin is reduced [18]. A hepcidin deficiency is considered one of the main reasons for beta thalassemia [19]. Individuals with beta thalassemia suffer from chronic anemia due to low hemoglobin levels [20]. There are different kinds of beta thalassemia, but beta thalassemia major is the most severe. Patients suffering from this form of beta thalassemia often need blood transfusions to treat the disease [21]. However, as previously discussed, repeated blood transfusions can lead to Fe accumulation in critical organs such as the heart, liver and pancreas. This Fe overload can result in organ damage and dysfunction [22].

The treatment of HHC (in cases where phlebotomy is not possible) and beta thalassemia involves chelation therapy. Since the body does not have a specific mechanism of Fe excretion, chelation therapy is used to remove Fe through urine or feces [23]. Early chelation therapy prevents Fe overload and associated complications. Therefore, detecting Fe overload in the early stages is essential to maximize the benefits of chelation therapy.

1.3 CURRENT TECHNIQUES FOR THE MEASUREMENT OF IRON OVERLOAD

Several methods are currently available for the measurement of Fe overload *in vivo*, although all current measurements have limitations and drawbacks. These methods include serum ferritin measurement, liver biopsy, magnetic resonance imaging (MRI) and superconducting quantum interference devices (SQUIDs).

Serum Ferritin

The most commonly used marker to assess Fe levels in the body is serum ferritin. As previously discussed, ferritin is a blood protein that stores/binds extra Fe in the body and releases it in a controlled manner according to the body's needs [24]. The measurement of serum ferritin is used as a test to diagnose a body's Fe overload and deficiency, anemia. High ferritin levels may indicate Fe overload and low ferritin levels may indicate Fe deficiency. However, serum ferritin values are sensitive to inflammation, infection, liver disease, and other medical conditions. This can produce false positive or false negative results [25]. It is, therefore, not always a good predictor of Fe overload in the body.

Liver Biopsy

The gold standard for assessing Fe overload is the measurement of liver Fe concentration by liver biopsy [26]. A liver biopsy can directly assess liver Fe, and liver Fe level is known to correlate closely with total body Fe stores [27]. However, this method is invasive, and many patients are reluctant to undergo this procedure due to post-operative pain and the risk of infection. A liver biopsy is also expensive and is not free of sampling error [28].

Therefore, while considered the most accurate technique, liver biopsy has never been entirely accepted as a standard clinical method for measuring Fe overload.

Magnetic Resonance Imaging (MRI)

MRI is a technique that uses strong magnetic fields and radio frequency waves to generate three-dimensional images of a body [29]. The human body mainly comprises water and fat tissues containing hydrogen atoms. The H ions or protons spin randomly, cancelling out their magnetic fields. However, when a strong external magnetic field is applied to the body, the magnetic fields of protons (H ions) align in the direction of the external magnetic field. This alignment is called longitudinal magnetization. When protons align in the direction of the external magnetic field, they precess with a frequency dependent on the external magnetic field strength. Increasing the external magnetic field makes the protons precess faster.

When a radio wave with the same frequency as the protons' precessional frequency is applied, resonance occurs, and protons absorb maximum energy. This energy absorption disrupts their longitudinal magnetization but synchronizes all the precessing protons. The synchronization of precessing protons results in transverse magnetization. The transverse magnetic field does not stay still but moves along with the precessing protons.

The changing transverse magnetic field generates a current that act as an MRI signal. When the radio frequency pulse is turned off, the protons exchange extra energy with surrounding atoms, and the system returns to its normal state. Transverse magnetization starts to disappear, which is called transverse relaxation or T2, while longitudinal magnetization grows back, known as longitudinal relaxation or T1. Different tissues have different T1 and T2 values. Liquids have a longer T1 (difficult to exchange energy) than fat tissues. However, T2 relaxation depends on the inhomogeneities of the external and local magnetic fields in the surrounding tissues. This is the basis of the detection of Fe in the liver using MRI techniques. Assessment of Fe overload in the liver relies on observing the changes in T2 relaxation times caused by the Fe paramagnetic properties. The faster T2 relaxation time

is directly proportional to the amount of Fe present and a decrease in MRI signal intensity [30].

MRI is therefore a non-invasive method of determining Fe concentrations in organs such as the liver, heart and pancreas. MRI has replaced liver biopsy to quantify liver Fe concentration in many clinical situations [31]. However, at high liver Fe concentrations, the signal intensity is reduced to the extent that it is difficult to quantify or differentiate between different liver Fe concentrations accurately. Also, fibrosis in the liver tissues can introduce variability in the estimation of liver Fe concentration by MRI [32]. Finally, as Fe detection is based on local changes in the magnetic field caused by the element's paramagnetic properties, other paramagnetic materials, e.g. gadolinium or manganese, both used as image contrast agents [33], [34], can perturb the measurement.

Superconducting Quantum Interference Device

SQUIDs are sensitive detectors that can measure magnetic fields, including the magnetic field of Fe or Fe compounds. SQUIDs comprise two superconductor loops connected through extremely thin insulating layers called Josephson junctions. When these superconductors are joined in this configuration, electrons can tunnel through the junction and results in the generation of supercurrent even in the absence of applied voltage due to the zero resistance of superconductors. However, when a magnetic flux passes through the superconductor loops, it induces a current that opposes the supercurrent and results in a voltage drop. The voltage drop across the device strongly correlates to the magnetic field applied across SQUIDs [35]. This detection principle forms the basis for employing SQUIDs to quantify liver Fe. SQUID magnetometry is a non-invasive technique that has been shown to accurately measure liver Fe concentration. However, the high cost of the procedure, limited availability of instruments and low environmental magnetic noise requirements are limitations to the widespread adoption of this technique [36].

1.4 XRF MEASUREMENT OF IRON OVERLOAD

The previous section presented arguments that the current methods of Fe measurement have limitations. Some techniques do not quantify Fe accurately, some are invasive, and some are expensive and have limited instrument availability. Therefore, a non-invasive, economical method is needed to accurately measure Fe concentrations *in vivo*.
Systems for the measurement of Fe overload by XRF spectroscopy have been previously developed. A literature review of the measurement of Fe by XRF is discussed below.

Milman *et al.* measured liver Fe concentration using a Si (Li) semiconductor detector system. They compared the liver Fe concentration in large liver samples taken with plastic knife, weighing approximately 10 g, to autopsy samples taken with Menghini needle from the same liver. The excitation source utilized in the study was an X-ray tube equipped with a variable voltage system, operating within the 20-60 kilovolts (kV) range and adjustable in 5 kV increments. The primary X-rays generated within the X-ray tube were directed toward a yttrium-based secondary target. For the experimental procedure, the liver sample was positioned perpendicular to the direction of the X-ray beam, thereby ensuring irradiation by secondary X-rays emanating from the yttrium. The study demonstrated a strong agreement in Fe content between autopsy-derived and large liver samples [37]. However, the study was conducted on cadavers and has limited applicability to *in vivo* measurements due to the invasive nature of the test procedure.

The non-invasive measurement of Fe overload was studied by Zeimer *et al*. by measuring dermal Fe content in beta thalassemia major patients receiving blood transfusions. They employed a monochromatic X-ray beam generated at approximately 45 kV and 3 mA, wherein the L_β line (11.4 keV) from a gold target was utilized as the excitation energy. The monochromatic beam was obtained via reflection from a curved crystal and precisely directed onto the patient's skin. Fe X-rays from the skin were detected using a Si (Li) detector with an effective area of 100 mm^2. A strong correlation was demonstrated between dermal Fe levels and the blood transfusion rates in these patients. In a second group of similar patients, they demonstrated a parallel rate of Fe deposition in the dermis and Fe

accumulation in the liver [38]. While these two groups of patients demonstrated significant correlations between transfusions and skin Fe levels, the authors' acknowledged that there are other sources of Fe buildup in the skin beyond blood transfusions, including elevated Fe absorption in the gastrointestinal tract among individuals with beta thalassemia. Therefore, it was impossible to attribute Fe accumulation in the skin solely to the frequency of blood transfusions.

Gorodetsky *et al.* conducted a study to examine skin Fe levels in patients with beta thalassemia major and beta thalassemia intermediate. They used a monochromatic beam of 11.4 keV X-rays emitted from an X-ray tube with a gold target material. The skin area was gradually rotated to facilitate the examination of the total area measuring 15 mm^2. The XRF generated in the skin tissues was subsequently analyzed with a Si (Li) solid state detector with an active area of 135 mm^2. Fe levels were measured at two sites on the body: the thenar eminence and the flexor surface of the forearm. This study found higher than normal levels of skin Fe in patients with beta thalassemia major. However, no correlation was established between skin Fe levels and beta thalassemia intermediate patients [39].

Friedlaender and Gorodetsky *et al*. performed further studies and monitored the excess Fe accumulation in the skin of patients undergoing regular hemodialysis treatment. They utilized the same XRF system, described above, to measure skin Fe levels in patients and in healthy people. They correlated skin Fe content with the total number of blood transfusions and transfusion frequency [40]. However, the quantification of Fe overload in patients was related only to the number of blood units they received, and Fe overload could not be measured if the number of transfusion units were less than 16.

In yet another study, Gorodetsky *et al.* demonstrated that skin Fe could be the most informative indicator of Fe clearance from parenchymal organs in patients undergoing chelation therapy [41]. However, the systems utilized in studies [30]-[34], employed an X-ray tube and a Si(Li) detector to measure fluorescence emitted from the skin. While this system was used very successfully in a number of pre-clinical studies of Fe overload

disease, the system needed liquid nitrogen for cooling. This made it bulky, and less portable and subject to the availability of liquid nitrogen.

In more recent studies, Farquharson *et al*. performed XRF analyses to investigate the relationship between skin Fe and liver Fe concentrations. Their study utilized rats who were administered Fe dextran injections to load them with Fe and then treated with chelating agents. An X-ray tube with a tungsten target operated at 25 kV and 15 mA was used as the excitation source. The X-ray beam generated by the tube was directed onto the copper plate, and the resulting fluorescence from the copper was then focused onto the skin samples. The Fe X-rays emitted from the skin samples were captured and analyzed with a lithium drifted silicon detector. A strong correlation was found between the skin and liver Fe concentrations in these animals [7]- [6]. The study, however, was confined solely to rats. The accuracy of the system is yet to be tested in different animal models whose skin closely more approximates human skin, which will be required before application in clinical settings can be considered. In addition, the system uses an X-ray tube and, in some jurisdictions, including the Province of Ontario, current legislation makes the use of the system in human research studies extremely challenging.

Esstevam *et al*. used a Si PIN photodiode detector system to detect and analyze skin Fe concentrations. The 13 and 17 keV energy lines of ^{238}Pu were utilized as the excitation energies. They calibrated their system with water phantoms and reported a dose of less than 10 mSv to the skin in a measurement time of 150 s. Subsequently, the system was employed to assess the skin Fe concentration in one individual with beta thalassemia and four healthy people. The authors demonstrated that their system accurately measures Fe levels consistent with existing literature [42]. While showing that an XRF measurement system had applicability to the assessment of skin Fe level, this study had limitations: a relatively high dose rate, a high detection limit, and a small sample size.

A study on rats [5] was carried out by Dao *et al.* They studied the Fe levels in organs of rats overloaded with Fe and assessed the Fe concentrations using both a laboratory-based XRF system and a commercial hand-held XRF system (Olympus Innov-X Delta Professional Handheld XRF Analyzer, USA) typically used in mining and construction.

The laboratory XRF system comprised a silicon drift detector which measured the beam from the sample while being positioned at a right angle to the incident X-ray beam. The X-ray tube of this system has a molybdenum target and was operated at 50 kV and 500 μA. It utilised a monochromator and beam focussing device resulting in a 2x2 mm beam of 17keV. The handheld commercial XRF system, also based on a silicon drift detector, operated at 40 kV and 0.1 μA current. Details of the target and filter used in the commercial system are proprietary and not fully available. Fe concentrations in the skin, liver, kidney, and blood were measured with both devices, revealing a strong correlation between skin and liver Fe concentrations. However, the use of the commercial XRF system resulted in a high dose rate of 30 mSv min^{-1}. Moreover, obtaining approval from the Ministry of Labour in Ontario (the regulatory body for X-ray sets used in human measurement) for the application of the commercial handheld XRF system in human measurements would be challenging due to its utilization of an X-ray tube. X-ray tube devices used in humans in Ontario must receive permits from the Ministry of Labour, and the application process is extensive. Further research using this device was suspended and the focus turned to radioisotope-based systems which are regulated by the Canadian Nuclear Safety Commission (CNSC). McMaster University holds permits from the CNSC for the application of radioisotope-based devices in human measurements.

In Paper III of this thesis, permission from the original study's authors was obtained to utilize skin samples from the same rats that had been held in long term storage in ultracold conditions (-80°C). These rat skin samples were employed to assess the performance of the the PXRF system (described in detail in this thesis) under conditions of Fe overload.

To summarise the work to date: XRF measurement of skin Fe concentrations has been shown to be a non-invasive technique that can potentially be used to monitor body Fe burden. Previous studies have shown a correlation between skin and liver Fe concentrations. Since the liver is widely acknowledged as the primary storage site for excess Fe, the assessment of skin Fe concentration by XRF should furnish valuable insights into the overall Fe load within the body.

1.5 X-RAY FLUORESCENCE ANALYSIS

The work in this thesis employs XRF spectroscopy to quantify the concentration of Fe in the skin. To understand the system development and application, an understanding of the interaction of radiation with human tissue is necessary.

1.5.1 Interaction of X-Rays with Tissues

When an X-ray photon enters human tissue, it can be absorbed or scattered. The main interaction processes of an X-ray photon (of energy 0 to 50 keV) with human tissue are the photoelectric effect, the Compton effect and Rayleigh scattering.

The Photoelectric Effect

In this interaction process, the inner shell tightly bound electron, such as the K-shell electron, absorbs incident photon. If the energy of the incident photon E_γ is greater than the binding energy of the electron E_B, the electron will be ejected from the shell, creating a vacancy. The vacancy in the K-shell is filled by the electron from higher energy levels, and the difference in energy between the two levels is released as characteristic X-rays. The ejected electron is called the photoelectron, and this effect is called the photoelectric effect. The schematic diagram of the photoelectric effect is shown in Figure 1.1.

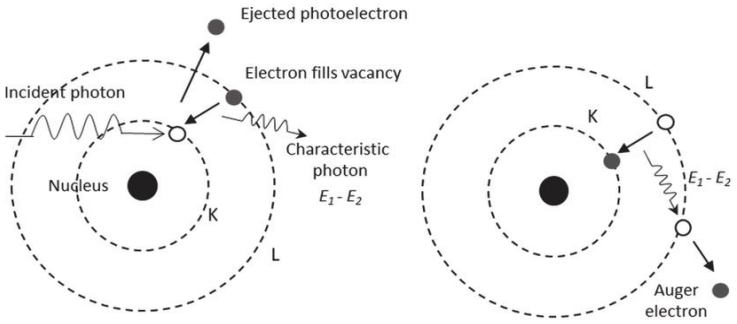

Figure 1.1: Schematic representation of photoelectric and auger effect [43].

The kinetic energy E_k of the ejected electron is given as

$$E_k = E_\gamma - E_B \quad (1.1)$$

The cross-section (probability of interaction) of the photoelectric effect depends upon the atomic number Z of the element and the energy of the incident photon. The photoelectric cross-section is expressed as [44],

$$\sigma_{ph} \propto \frac{Z^n}{E_\gamma^{3.5}} \tag{1.2}$$

Where the value of n is between 4 and 5.

Thus, the photoelectric effect is more dominant in materials with high atomic numbers and decreases with increasing energy of the incident photons. The photoelectric effect usually occurs with inner shell tightly bound electrons such as K-shell electrons, so the K-shell photoelectric cross-section $\sigma_{ph,K}$ is given as [44]

$$\sigma_{ph,K} = \left[\frac{32}{\varepsilon^7}\right]^{\frac{1}{2}} \alpha^4 Z^5 \sigma_{Th}\, cm^2 atom^{-1} \tag{1.3}$$

Where $\varepsilon = \frac{E_\gamma}{m_e c^2}$, $\sigma_{Th} = \frac{8}{3}\pi r_e^2 = 665\, mbarn$, $\alpha = \frac{e^2}{\hbar c} = \frac{1}{137}$ is the fine structure constant and σ_{Th} is the Thomson scattering cross-section.

Compton Scattering

Compton scattering is an inelastic scattering in which a photon interacts with the loosely bound electron. In this process, the photon with initial energy E_γ is scattered at an angle θ and the electron at an angle φ with the initial photon direction.

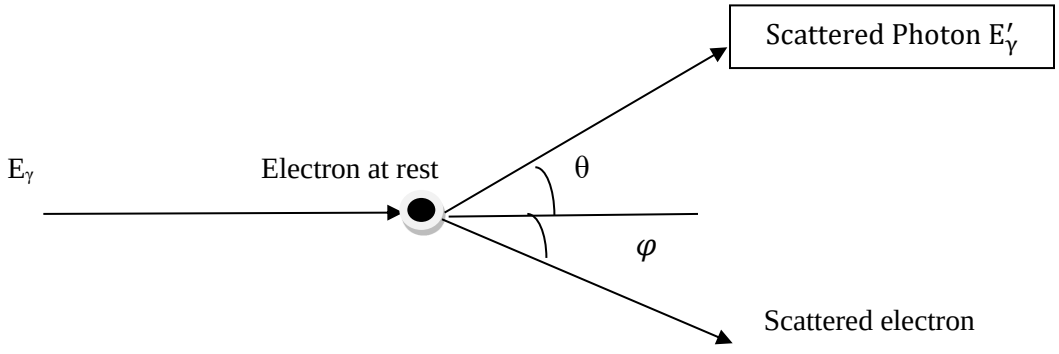

Figure 1.2: Representation of Compton scattering with the loosely bound electron.

The energy of the scattered photon is given as [44]

$$E'_\gamma = \frac{E_\gamma}{\left[1 + \frac{E_\gamma}{m_0 c^2}(1 - \cos\theta)\right]} \tag{1.4}$$

The above equation shows that the scattered photon energy depends on the initial energy of the incident photon and the scattering angle θ. Thus Compton scattering is not an isotropic process [44]. In this process, the electron is scattered with kinetic energy T, equal to the difference between the incident and the scattered photon energies. The maximum kinetic energy, $T_{max,}$ of the scattered electron, is given as [45]

$$T_{max} = \frac{2\,E_\gamma}{2 + \frac{mc^2}{E_\gamma}} \tag{1.5}$$

In the case of a beam of photons, the scattering of photons at different angles is given by the Klein-Nishina equation. The results of the Klein-Nishina equation are shown in Figure 1.3.

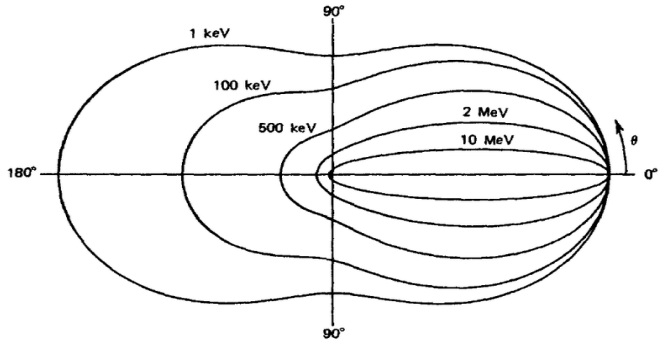

Figure 1.3: Polar plot of Compton scattering cross-section at different energies [46].

Figure 1.3 demonstrates the probability of scattered photons at different angles as a function of incident photon energies. It can be seen that higher photon energies favour more forward

scattering. However, in the low photon energy range, especially below 100 keV, the photon angular distribution peaks in the backward direction.

Rayleigh Scattering

In this type of interaction, an X or gamma ray photon interacts with all the electrons of the target atom. This type of interaction is also known as coherent scattering, as no energy is lost during the interaction process. However, the direction of photon changes after interaction and should be considered in radiation transport phenomena. This process dominates at low incident energies and for high Z materials [47].

1.5.2 Attenuation of Photons through Tissues

When a beam of photons incident on the surface, the number of photons (N) per unit area (A) perpendicular to the beam is called the radiation fluence or simply fluence (Φ) [48]

$$\Phi = \frac{\mathrm{N}}{\mathrm{A}} \tag{1.6}$$

The size of the area does not matter as long as the beam distribution is uniform. However, the fluence must be average over small areas for non-uniform beams. The fluence rate, $\dot{\Phi}$ is defined as the fluence per unit time t,

$$\dot{\Phi} = \frac{\mathrm{N}}{\mathrm{A\,T}} \tag{1.7}$$

For a beam of photons having the same energy E, the product of fluence rate and the energy is called the energy fluence rate (Ψ_o) or simply the intensity I_o [48],

$$\mathrm{I}_o = \dot{\Psi}_o = \frac{\mathrm{N.E}}{\mathrm{A.T}} \tag{1.8}$$

When a beam of photons of intensity I_o passes through tissues, it can undergo one of the interaction processes discussed in the subsection 1.5.1. Thus, if a photon does not interact

with the medium, it will not lose energy and be a part of the beam. However, as a photon beam passes through matter, its intensity decreases, which is given by the following relationship [44]

$$I = I_o\, e^{-\mu_t x} \tag{1.9}$$

Where x is the thickness of the material, I is the beam's intensity at thickness x, and μ_t is the material's total linear attenuation coefficient (cm^{-1}).

The total linear attenuation coefficient gives the interaction probability of photons per unit distance. When a photon enters the tissues, it covers some distance before interaction. This distance is called the mean free path λ_p and is related to μ_t as;

$$\lambda_p = \frac{1}{\mu_t} \tag{1.10}$$

Thus, the mean free path will be greater for high-energy photons and materials with a lower attenuation coefficient.

The probability that a photon passes through a material of thickness x without interaction is $e^{-\mu x}$. Where $e^{-\mu x}$ is the total probability and is equal to the product of probabilities that a photon does not interact by any of the interactions discussed in subsection 1.5.1. The most common interactions for Ag X-rays used for the excitation of Fe in the skin are the photoelectric effect and Compton scattering. Therefore, μ is written as

$$\mu = \sigma + \tau \tag{1.11}$$

Where σ and τ are the coefficients of Compton scattering and the photoelectric effect, respectively.

The quantity that is preferred over the linear attenuation coefficient is the mass attenuation coefficient, μ_m, measured in cm^2g^{-1}. μ_m is the linear attenuation coefficient divided by the

density of the material. Linear attenuation coefficients depend on the energy and the atomic number of the material but do not account for the material density. μ_m , on the other hand, accounts for the density of the material and is more suitable for comparing and understanding the radiation interaction properties of different materials regardless of their densities.

1.5.3 Radiation Dose from X-ray Interactions

When ionizing radiation such as X and gamma rays enter the body, they deposit energy. The energy deposited by ionizing radiation per unit mass is called a radiation dose. When X or γ-rays traverse through the tissues, some get absorbed, while others scatter at different angles. Thus, not all the energy of the incident X and γ-rays is absorbed in the tissues. The decay of ^{109}Cd generates γ-rays and Ag X-rays. The principal interaction mechanisms of these X and γ-rays in human tissues are the photoelectric effect and Compton scattering (Figure 1.4).

It is evident from Figure 1.4 that at the lowest energies (<10 keV), the main interaction process in the tissues is the photoelectric effect. As the energy increases (between 10 and 30 keV), the photoelectric cross-section drops rapidly, and the probability of incoherent scattering increases. Between 30 and 100 keV, most attenuation is due to Compton or incoherent scattering. Therefore, the Ag X-rays (22.1 keV and 24.9 keV) emitted from the decay of ^{109}Cd transfer energy to tissues through both photoelectric and incoherent scattering. These X-rays are the primary contributors to the radiation dose in human tissues.

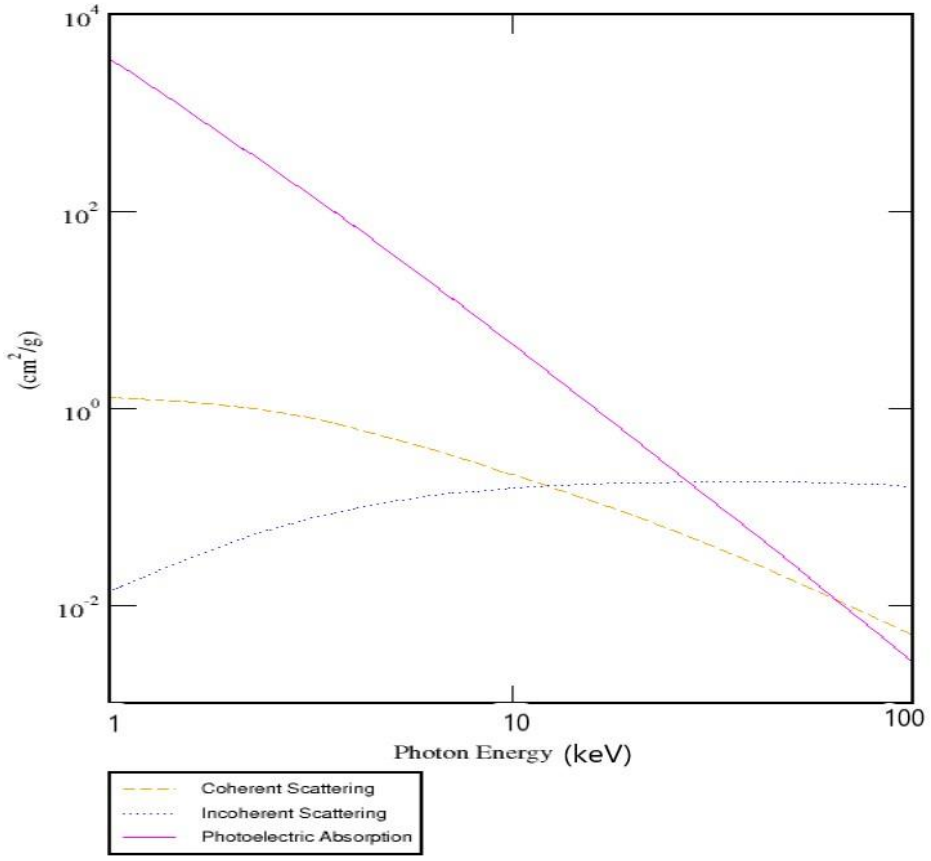

Figure1.4: Coherent, incoherent and photoelectric cross sections (cm^2g^{-1}) of human tissues up to 100 keV [49].

As discussed in section 1.5.1, the absorption of incident photons in the inner shells creates a vacancy that is filled by the higher shell electrons. The transition of electrons from higher shells results in the emission of characteristics X-rays or Auger electrons. The mass-energy transfer coefficient $\frac{\tau_{tr}}{\rho}$ for photoelectric effect is given as [45],

$$\frac{\tau_{tr}}{\rho} = \frac{\tau}{\rho}\left(1 - \frac{\Delta}{E}\right) \tag{1.12}$$

Where $\left(1-\frac{\Delta}{E}\right)$ is the fraction of incident energy transferred to photoelectrons and Auger electrons and $\frac{\tau}{\rho}$ is the photoelectric mass attenuation coefficient. Equation (1.12) gives the fraction of energy that is transferred to electrons $g^{-1}cm^{-2}$.

The mass-energy transfer coefficient for Compton scattering $\frac{\sigma_{tr}}{\rho}$ is defined as [45],

$$\frac{\sigma_{tr}}{\rho} = \frac{\sigma}{\rho}\frac{T_{avg}}{E} \tag{1.13}$$

Where $\frac{\sigma}{\rho}$ is the Compton mass attenuation coefficient. $\frac{T_{avg}}{E}$ is the average fraction of the incident photon energy converted into the Compton electron's kinetic energy.

The total mass-energy transfer coefficient $\frac{\mu_{tr}}{\rho}$ for photons with energy E is given by the sum of equations (1.12) and (1.13). The quantity that has an essential role in estimating the absorbed dose is the mass energy absorption coefficient $\frac{\mu_{en}}{\rho}$ and is related to the mass energy transfer coefficient by the following equation [50],

$$\frac{\mu_{en}}{\rho} = \frac{\mu_{tr}}{\rho}(1-g) \tag{1.14}$$

$\frac{\mu_{en}}{\rho}$ quantifies the average fraction of incident photon energy transferred to charge particles due to the interactions discussed in subsection 1.5.1; g represents the average fraction of incident energy transferred to electrons and subsequently radiated as bremsstrahlung.

The rate of energy absorption in the tissues is called the dose rate and can be approximated by the following relationship [45],

$$\dot{D} = \dot{\Psi}_o \left(\frac{\mu_{en}}{\rho}\right)_{tissues} \tag{1.15}$$

Where $\dot{D}$ is the dose rate and is equal to the product of the energy fluence rate $\dot{\Psi}_o$ and the mass energy absorption coefficient in tissues $\left(\frac{\mu_{en}}{\rho}\right)_{tissues}$.

The measurement and calculation of dose rate in tissues due to ^{109}Cd is discussed in paper I of this thesis.

1.5.4 X-ray Fluorescence

This thesis work is based on XRF, a non-destructive analytical technique that is used for the elemental analysis of materials. This technique can be used to determine the elemental composition of a material qualitatively and quantitatively. Almost all elements, from sodium (Na) to uranium (U), can be detected down to concentration levels in parts per million (ppm) or even sub-ppm [51]. The detection limit depends upon the element's atomic number and concentration in the material, but generally, heavier elements have better detection limits.

XRF is based on the interaction of X-ray photons with matter. When an X-ray photon passes through tissues, it can interact with tissue atoms with one of the processes previously discussed. If the energy of the incident X-ray photon is greater than the binding energy of inner shell electrons, it may undergo photoelectric absorption and can eject inner shell electrons. The probability of photoelectric absorption increases with decreasing energy and becomes maximum if the incident photon energy matches or is slightly greater than the binding energy of bound electrons.

The ejection of the electron from the inner shell creates a vacancy that is filled by the electron from higher shells. This rearrangement results in a release of characteristic X-ray whose energy is equal to the difference in energy between the two shells. These X-rays are characteristics of the element and serve as a fingerprint to identify an element.

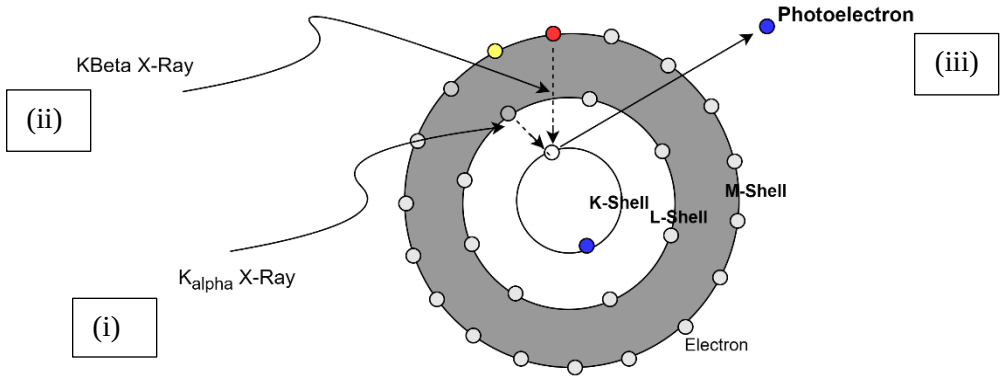

Figure 1.5: XRF is a three-step process. (i) Incident X-ray photon knocks out an inner shell bound electron, creating a vacancy (ii) The vacancy is filled by the electron from the higher shells (iii) Characteristic X-rays are emitted as a result of the transition from higher shells.

Different characteristic X-ray lines are obtained due to the electron transition between different energy levels. The observed X-ray series are named after letters of the alphabet, such as the K, L, M and N series. The letters K, L, M and N correspond to the principal quantum numbers 1, 2, 3 and 4, respectively. The K series occurs if the transition of electrons from higher levels ends at the K shell. The primary lines in this series are K_α and K_β. K_α corresponds to the transition of electrons from the L shell to the K shell, while the K_β line is obtained if the transition is from the M shell to the K shell. Similarly, the L series involves electron transition from higher shells to L shells. $L_{\alpha,}$ L_β and L_γ are the main lines of this series and are obtained when electrons from M, N, and O shells fill the vacancy in the L shell.

The K_α lines are the most prominent in the X-ray spectrum due to their high intensity. K_β lines are lower in intensity than the K_α lines. The ratio of the K_α to K_β intensities is a constant for an element but varies for different elements. This ratio is higher for light elements; for example, it is approximately 25:1 for aluminum, while it is lower for heavier elements, such as tin, where it is approximately 3:1 [52].

Fe K X-ray Emission

The most prominent X-rays of Fe are the K_α (6.4 keV) and K_β (7.06 keV) lines. The production of Fe characteristic X-rays is shown in Figure 1.6.

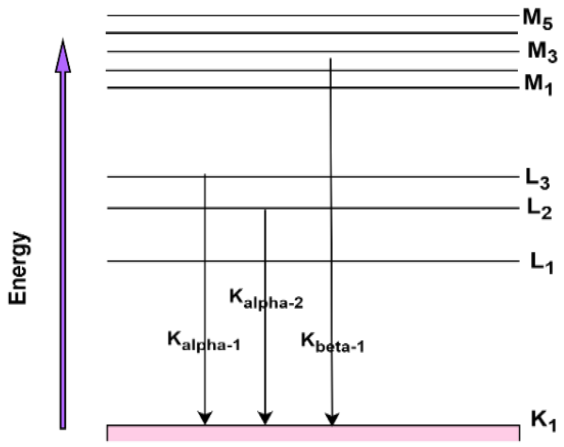

Figure 1.6: Production of Fe characteristic X-rays. $K_{\alpha 1}$ X-ray resulting from L_3 to K-shell electronic transition and $K_{\alpha 2}$ from L_2 to K-shell. The subscripts on L-shell 1,2,3 represent the subshell (s,p,d etc.).

In order to excite electrons of an atom, the excitation energy must be greater than the binding energy of inner shell electrons. The binding energy of inner shell electrons, such as K-shell, is referred to as K-edge. The K-edge of Fe is 7.11 keV. Figure 1.7 shows the photoelectric cross-section of Fe for incident energies up to 88 keV.

It is evident from Figure 1.7 that photoelectric cross section decreases with increasing energy. However, there is a sudden increase in photoelectric cross section that occurs at the K-edge. Any photon with energy surpassing the K-edge can ionize an atom, with energies slightly above the K-edge exhibiting the greatest likelihood of ionization.

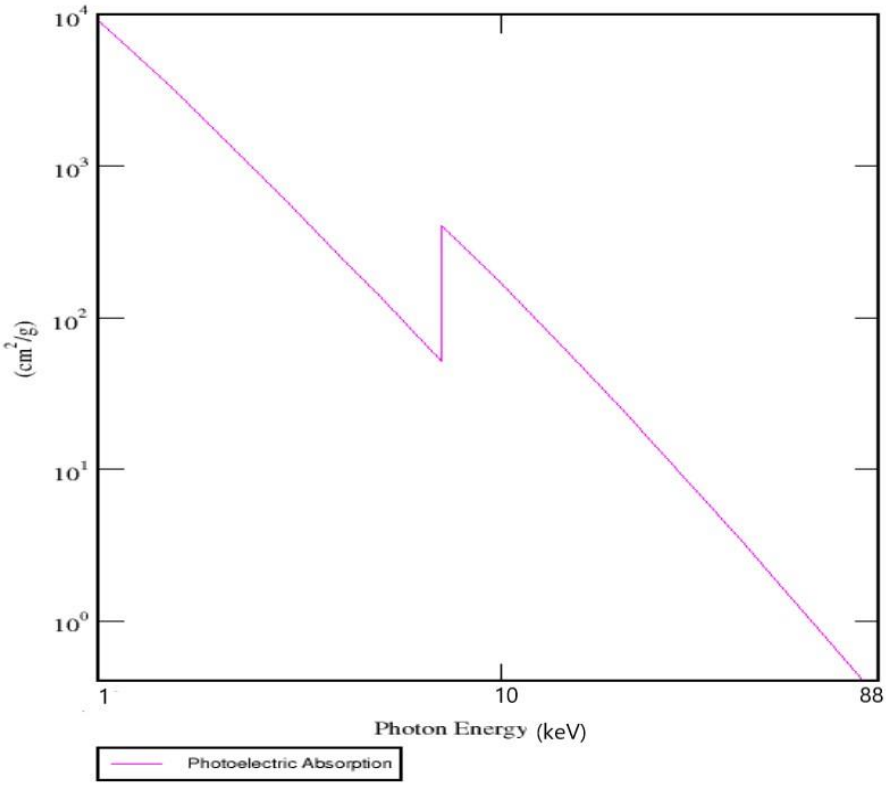

Figure 1.7: Photoelectric cross-section of Fe for incident energies up to 88 keV [49].

In an XRF system for the measurement of Fe in skin, the Fe X-rays generated in the skin must travel some distance in the tissues and hence there is a loss of intensity before entering the detector. Therefore, knowing to what depth Fe X-rays can be detected is important. The total mass attenuation coefficient of human skin at the Fe K_α energy of 6.4 keV, obtained from the National Institute of Standards and Technology (NIST) XCOM, is 18.04 cm^2g^{-1}. The density of human skin is taken as 1.1 gcm^{-3} [53], therefore the mean free path, λ_p, of Fe K_α can be calculated as,

$$\mu_t = \mu_m \times \rho$$

$$\mu_t = 19.84\ cm^{-1}$$

$$\lambda_p = \frac{1}{\mu_t} = 0.5 \text{ mm}$$

Hence a decrease of 63 % in the intensity of Fe K X-rays occurs at a depth of 0.5 mm within the skin. This establishes a spatial limit for the detection of Fe X-rays within the skin. In XRF analysis, the path length for measuring elements is generally deemed practical if it is within four to five mean free paths. The thickness of the skin's outer layer exhibits variability, ranging from 0.06 mm at the eyelids to 0.8 mm at the palm of the hand [54]. Research indicates that the concentration of Fe in the skin peaks at the stratum granulosum, which is the second layer of the epidermis from the surface [55]. Consequently, the depth at which Fe in the skin reaches its peak is less than the mean free path of Fe. Therefore, detection of Fe in the superficial layers of the skin should be feasible. Chapters 3 and 4 of this thesis explore some effects of the spatial distribution of Fe on XRF measurements.

Auger Electrons and Fluorescence Yield

The competing process for the X-rays measured in X-ray fluorescence is the Auger effect. The Auger effect is a radiationless electronic transition in which electrons with specific energies are expelled from the atoms when another electron within the atom undergoes a downward transition [56]. In this process, the inner K-shell vacancy is filled by a next higher shell, such as the L-shell. The energy released during this transition can be transferred to another electron within the atom, leading to the ejection of an Auger electron (Figure 1.1). The probability of this effect increases for elements with low atomic numbers. As a result of the Auger effect, the number of characteristic X-ray photons decreases. Fluorescence yield is the probability that fluorescence photons are emitted due to transition in the excited atom [57]. The K-shell fluorescence yield ω_k is

$$\omega_k = \frac{N_k}{V_k} \tag{1.16}$$

Where N_k is the number of fluorescence X-rays emitted from the K shell of the atom as a result of V_k vacancies in the K-shell.

The Fe K-shell fluorescence yield is 0.35 [58], meaning 35 % of the inner shell vacancies in Fe result in K-shell X-ray emission rather than other processes. The fluorescence yield of Fe is not as high as other elements, such as gold or lead; this low fluorescence yield is one of the reasons that XRF measurements of Fe are challenging.

1.5.5 Instrumentation

XRF instrumentation usually consists of (i) an excitation source used to excite sample atoms, (ii) a sample to be analyzed and (iii) a detector that measures the energies and intensities of fluorescence X-rays emitted by the sample, as shown in Figure 1.8.

The following section discusses the properties of the excitation source and the detector system utilized in the work in this thesis. Details of the samples (i.e., the phantoms and skin) are discussed in the three papers of this thesis.

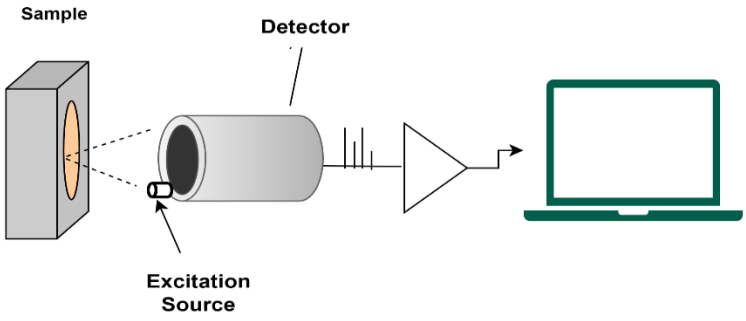

Figure 1.8: The detection system used for the measurement of Fe-characteristic X-rays.

1.5.5.1 Excitation Source

The work presented in this thesis utilizes ^{109}Cd to excite Fe atoms in the skin. The half-life of ^{109}Cd is 464 days. It decays by electron capture (100 % probability) to the isomeric state of ^{109}Ag. ^{109}Ag being unstable, it then decays to ground state by emitting 88 keV (3.72 %) gamma rays or by the emission of an electron by internal conversion (96.24 %). The higher

shell electrons fill the vacancy created due to electron capture by ^{109}Cd and by the internal conversion of ^{109}Ag. In this process, Ag X-rays of $K_{\alpha 1}$= 22. 16 keV (55.1%), $K_{\alpha 2}$= 21.99 keV (29.2%) and K_{β}= 24.9 keV (17.92 %) are emitted. For every 88 keV emission, there are approximately 15 $K_{\alpha 1}$,8 $K_{\alpha 2}$ and 5 K_{β} Ag X-rays. Thus, in the decay of ^{109}Cd, Ag X-rays dominate, and there are more Ag X-rays than 88 keV gamma rays. The decay scheme of ^{109}Cd is shown in Figure 1.9.

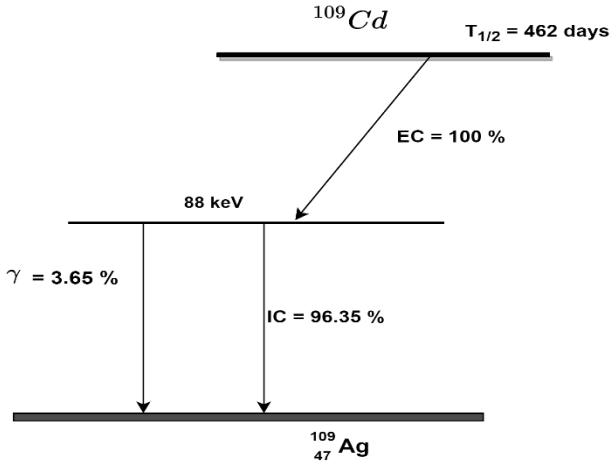

Figure 1.9: Decay scheme of ^{109}Cd

The photoelectric cross section measures how likely a photon is to interact with a material through the photoelectric effect. For Fe, the cross section of the 88 keV gamma ray is 0.48 cm^2g^{-1}. At the lower energies of the 22.1 keV and 21.99 keV Ag X-rays, the cross sections for Fe are to 19.4 cm^2g^{-1} and 19.7 cm^2g^{-1}, respectively. Comparatively, Ag X-rays have a much higher cross section, around 40 times greater than that of 88 keV gamma rays. Moreover, since there are more Ag X-rays than 88 keV gamma rays emitted as a result of the decay, most photoelectric interactions in Fe from a ^{109}Cd source are caused by Ag X-rays rather than by 88 keV gamma rays.

1.5.5.2 Detector System

Choice of a Detector for Fe X-Ray Measurement

The present study employs the silicon drift detector (SDD), a semiconductor detector, as the primary detection device. Detector selection for an XRF system depends upon several factors which are explained here through a comparative analysis between the SDD and alternative detector types. The comparison will start by contrasting semiconductor detectors with gas and scintillation detectors. Also, the advantages of Si-based semiconductor detectors in measuring low energy X and gamma rays, particularly in comparison to Ge detectors are discussed.

Comparison of Semiconductor Detectors with Gas and Scintillation Detectors

Semiconductor detectors are better than gas-filled detectors for measuring X and gamma rays. The average energy required to produce ionization in gas detectors is 30 eV, while it is approximately 3 eV to produce electron-hole pairs in semiconductor detectors. Additionally, semiconductor detectors exhibit higher charge collection and are made of high-density material (absorption of X and gamma rays is higher in high Z and density materials) compared to gas detectors. As a result, semiconductor detectors offer superior detection efficiency, energy resolution and count rate capability than gas detectors [46].

On the other hand, crystal scintillation detectors have higher atomic number (Z) and density than semiconductor detectors. Therefore, scintillation detectors such as NaI exhibits higher detection efficiency than semiconductor detectors. However, the average energy needed to produce an electron-hole pair is 100 times less in semiconductor detectors than in scintillation detectors. Consequently, the energy resolution and low energy gamma response of scintillation detectors is poorer than semiconductors detectors [59].

Comparison of Si and Ge Semiconductor Detectors

For X and gamma-ray detection, high atomic number materials (such as germanium) are commonly used as detectors. The gamma ray absorption coefficient and Compton scattering coefficient in silicon are very small due to its low atomic number and reduced electron density. Furthermore, it is worth noting that the energy threshold at which photoelectric absorption becomes comparable to Compton scattering is relatively low, only at 60 keV. Consequently, Si is not the most suitable choice for applications in high energy gamma ray spectrometry. However, an advantageous feature of silicon is that its K-absorption edge is at 1.838 keV, which is lower than the Ge K-absorption edge at 11.103 keV. The K-absorption edge of the detector material introduces a nonlinearity in the changes in the detector's efficiency with energy. This effect becomes more noticeable in detectors with higher K-absorption energies. Therefore, the nonlinearity is less pronounced for silicon compared to germanium. Additionally, the property of silicon to have fewer interactions with high energy gamma rays serves to minimize background effects [60]. Therefore, Si has a significance advantage in X-ray fluorescence analysis, particularly at energies below 50 keV.

Another property of Si that makes it better than Ge for low-energy X-ray measurement is the width of the energy bandgap. The energy bandgap E_g of a semiconductor is [60]

$$E_g = kT \ln\left[\frac{N_C N_V}{n_i^2}\right] \tag{1.17}$$

This can also be written as

$$n_i = \sqrt{N_C N_V}\ e^{-E_{g/2kT}} \tag{1.18}$$

Where, n_i is the intrinsic charge carrier concentration, and N_C and N_V are the effective density of state in the conduction band and in the valence band, respectively. K is Boltzmann's constant, and T is the absolute temperature.

Equations (1.17 and 1.18) show that the bandgap E_g has a significant effect on carrier concentration n_i. Thus, a material with a wide bandgap, such as Si (1.17 eV at 0K), has a lower charge carrier concentration and, therefore, less leakage current than Ge (0.74 eV at 0K) [61].

For all the reasons, Si detectors stand out as better for measuring low-energy X and gamma rays. In this study, SDD is employed due to its superior energy resolution, high count rate capability and high detection efficiency for low energy X and gamma rays.

Silicon Drift Detector

Silicon drift detectors are a modern type of semiconductor detector which are now more commonly used to measure low-energy X-rays. The concept of SDDs was first introduced by Emilio Gatti, an engineer at the Polytechnic Institute of Milan, and Pavel Rehak a Physicist at Brookhaven National Laboratory, in 1984 [62]. SDD is a semiconductor detector comprising a high-purity sensitive area of silicon, a cathode, a very small anode and annular electrodes. SDDs have become preferable because they have better energy resolution, higher count rate capability, better detection limits and improved sensitivity compared to Si(Li) semiconductor detectors [63]. They can also be cooled using Peltier cooling rather than using an external liquid nitrogen cooling system, and so are compact and can be made portable, which makes them more suitable for in-field or in-clinic applications.

The research work in this thesis utilized an SDD manufactured by KETEK Germany. The detector's energy resolution is $\leq$ 136 eV at Mn K_α and it has a peak to background ratio of greater than 15000. The absorption depth of the detector is 450 μm and has a sizeable collimated area of 150 mm^2. The detector has a thin beryllium window of 25 μm that allows low-energy X-rays to be detected [64]. The beryllium window is very delicate, and to protect the window, the manufacturers provide an approximately 3 mm thick Teflon cap to protect the window when the detector is not in use. However, for the safe operation of the detector a new aluminum ring cap was designed for the detector with styrene glued on the

top face as an entrance window. The styrene was thin enough to allow almost 80 % of the Fe K_α X-rays through to the detector and rigid enough to protect the thin, delicate beryllium window.

The basic detection principle of the SDD is the reverse-biased operation mode of semiconductor detectors. In this mode, when an X-ray photon enters the depletion region of the detector, it can undergo one of the X-ray interaction processes discussed earlier. The dominant interaction process for low-energy photons in an SDD, such as Fe X-rays, is the photoelectric effect. This interaction will create an electron-hole pair in the depletion region. The electric field created by the bias voltage causes the electron and holes to move to their respective electrodes. When equipped with appropriate electronics, the collected charge generates a pulse that can be recorded.

1.5.6 Detection of Fe X-Rays in Skin

Section 1.5 covers the technical background of XRF analysis. However, to study the detection process of Fe X-rays, it is necessary to examine the energies being measured in the context of the associated detector properties.

The incident Ag X-rays from the decay of ^{109}Cd are used to excite Fe atoms in the sample. However, the maximum probability of photoelectric absorption occurs when the incident energy is slightly above the binding energy of K-shell electrons. As previously discussed, this binding energy, known as the K-edge, is 7.11 keV for Fe. At an incident energy of 22.16 keV, the photoelectric cross section for Fe is 19.4 cm^2g^{-1}, which is approximately 16 times smaller than the photoelectric cross section just above the K-edge. An excitation source with photon energies closer to the edge should result in high Fe X-ray production. However, factors other than photoelectric cross-section are also part of the measurement process and must be considered while selecting an XRF source. ^{109}Cd has some advantages as a source when these factors are considered. For example, the Compton scattering of 22.16 keV and 24.9 keV does not interfere with the Fe K X-rays in the spectrum. The Compton backscattering of 88 keV γ-rays in the phantom results in a 65.5 keV

backscattered photon. The 65.5 keV scattered photon can undergo further Compton scattering and generates electrons in the detector with a maximum energy of 13.3 keV. This leads to a slight increase in the background under Fe K_α. However, 88 keV occurs only in 3.6 % of decays and the probability of Compton scattering of 65.5 keV photon in 0.450 mm thick SDD is very low, approximately 1.6%. The contribution to the background under the K_α X-ray peak is relatively small. Therefore, using ^{109}Cd as the excitation source for measurement of Fe results in a 'clean' spectrum, with a lower spectral background in the region of interest. A low background allows a higher signal-to-noise ratio, improved sensitivity, better detection limit and increased resolution.

When the characteristic X-rays of Fe interact with the detector material, they create an electron-hole pair. The collected charge at the electrode produces a pulse that can be detected using suitable electronics. The absorption efficiency of a detector increases with increasing thickness of a detector. The tenth value layer (TVL) defines the length of a material that can attenuate 90 % of the photons. The following relation calculates the TVL for Fe K_α (6.4 keV) in silicon [44].

$$\mathrm{TVL} = \frac{\ln(10)}{\mu} \tag{1.19}$$

Where μ (cm^{-1}) is the linear attenuation coefficient of silicon. The TVL for Fe K_α (6.4 keV) in silicon is 0.08 mm. The absorption depth of the SDD used in the current study is 0.45 mm.

By utilizing the linear attenuation coefficient of Si at 6.4 keV, which is measured to be 285.425 cm^{-1}, $1 - e^{-\mu x}$ equals 0.999. Thus, a detector of thickness 0.45 mm can absorb 99.9 % of Fe X-rays.

The absorption efficiency of SDD is shown in Figure 1.10 [65]. It can be seen that the absorption in Si is almost 95.4 % for energies up to 10 keV and reduces to ~50 % at 20 keV.

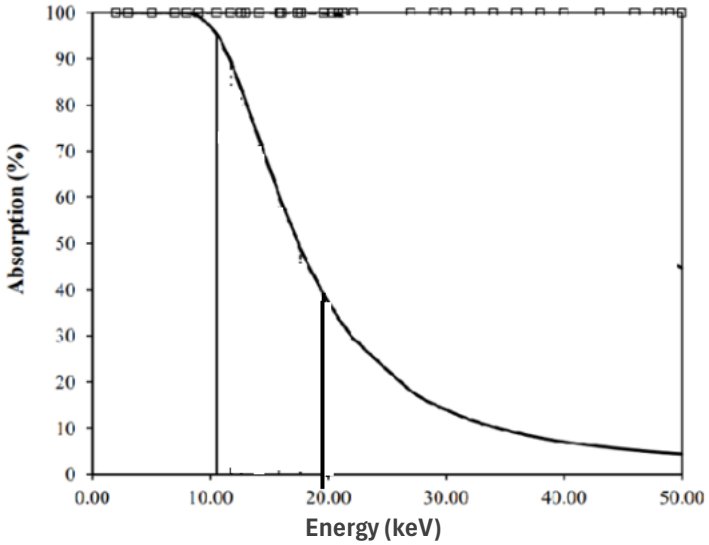

Figure 1.10: Absorption efficiency of 0.45 mm Si wafer at different energies.

1.6 MONTE CARLO SIMULATION

In addition to the experiments presented in this thesis, some aspects of the XRF detection of Fe in skin were modelled using Monte Carlo modelling. Monte Carlo simulation got its name from a famous gambling spot in Monaco as it relies on chance and randomness, much like games such as dice and slot machines. This technique was first developed by a Mathematician, Stanislaw Ulam. He was working on the Manhattan Project for the development of the atomic bomb. He discussed his idea with a fellow scientist, John Von Neumann, and the two worked together to improve the Monte Carlo simulation method [66].

Monte Carlo simulations represent a valuable tool with diverse applications across various domains of radiation physics, particularly in addressing complex geometries and analytical challenges that are difficult to solve experimentally. In fields like XRF and other radiation related disciplines, Monte Carlo simulations can accurately model X-ray interactions in complicated geometries and heterogenous materials.

Despite possessing a comprehensive understanding of the fundamental physics of photons and electron interactions within a medium, the formulation of an analytical expression to accurately describe particle transport within that medium is challenging. In response to this challenge, Monte Carlo simulation offers a solution. In Monte Carlo simulation, the knowledge of probability distributions that dictate the interactions between electrons and photons, enable us to accurately simulate the particle trajectories in a medium [67]. Additionally, Monte Carlo simulations find application in parametric studies, allowing for the manipulation of input parameters. For instance, in XRF analyses, changing the sample compositions and source parameters enables the study of different scenarios and facilitates a deeper understanding of the analytical process, which may be impossible or not practical to conduct experimentally.

Numerous Monte Carlo simulation codes are used in different areas of radiation physics, such as Electron Gamma Shower5 (EGS5) for photon and electron coupled transport [68], Monte Carlo N-Particle (MCNP), a general-purpose code for simulating the transport of many particles, including neutrons [69] and Geometry And Tracking (GEANT4) toolkit that simulate the passage of particles and radiations through matter [70].

Electron Gamma Shower (EGS5)

The work in this thesis uses the EGS5 code. This code was chosen for the current work because it has dedicated physics models for low-energy electron and photon interactions, including features like the introduction of Compton broadening [68], which are more specialized for low-energy photon interactions compared to MCNP and GEANT codes that were originally designed primarily for high energy particle interactions.

EGS5 is a general-purpose code for Monte Carlo simulation written in FORTRAN for radiation transport and developed at the Stanford Linear Accelerator Center (SLAC). It couples photons and electrons, having energy ranges from a few keV to several hundred GeV [71]. The original EGS code system, named EGS1, was developed by Richard Ford

and Ralph Nelson [71]. Over the years, subsequent versions of the code system were released.

This software facilitates the simulation of radiation transport within elements, compounds and mixtures characterized by atomic numbers ranging from 1 to 100. The program underwent expansion under the KEK National Laboratory for High Energy Physics in Japan, wherein significant enhancements were incorporated to precisely depict photon and electron interactions within the low-energy spectrum. Notable inclusions are the Compton broadening, the modelling of linearly polarized photon scattering, the generation and propagation of K and L fluorescence photons and photoelectrons and the electron impact ionization [72].

When conducting simulations using EGS code (or other Monte Carlo codes), it is very useful to be able to examine the geometry and particle trajectories visually. This visual validation of the geometry can play a vital role in confirming the accuracy of the calculation parameters. Furthermore, employing a graphical interface can prove to be highly beneficial for the understanding of the radiation interactions [73]. For these purposes, there is a useful tool in EGS5 called CGVIEW. CGVIEW can display three-dimensional trajectories of electrons, photons and positrons. Figure 1.11 displays an example of a detector geometry used in the work in this thesis as displayed by the CGVIEW interface.

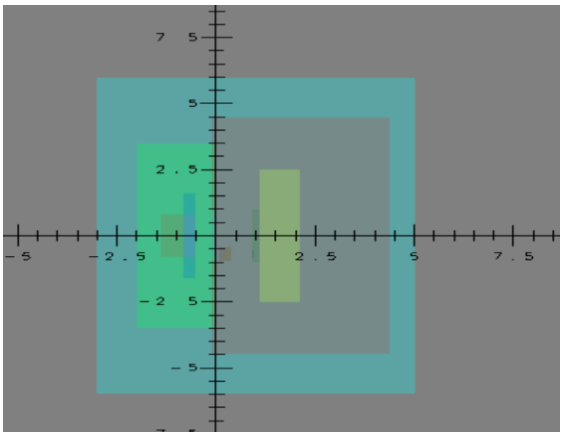

Figure 1.11: The geometry setup depicted in CGVIEW serves to simulate the actual geometry utilized in the study.

1.7 PROJECT GOAL AND THESIS OUTLINE

Previous work has shown that XRF measurement of skin Fe concentration is a non-invasive technique that can potentially be used to monitor body Fe burden. Application of the technique has shown a correlation between the skin and liver Fe concentrations, as discussed in section 1.4. Since the liver is widely acknowledged as the primary storage site for excess Fe, this suggests that the assessment of skin Fe concentration can provide an assessment of the overall Fe load within the body.

While there has been work by others using XRF to study Fe prior to the work in this thesis, there was still a need for improvements before such systems can be employed clinically. Detection limits needed to be improved, measurement times reduced, and doses were required to be as low as possible. Furthermore, system accuracy needed to be demonstrated by validation against a 'gold standard' technique. The current study thus describes the development and validation of an XRF system to measure skin Fe concentration. The next few chapters will show that the system demonstrates a superior detection limit compared to prior systems and the accuracy has been validated against established standards. Additionally, they will describe how the system offers the advantages of low radiation dose and portability, further demonstrating its potential for utilization in clinical settings. Due to its portability, the system is named as portable XRF (PXRF) through much of this work.

Objectives

The thesis describes the achievement of the following objectives.

Objective 1: Design and development of an XRF system capable of measuring Fe characteristic X-rays with improved detection limits with the capability to permit future use in clinics. The system employs a robust calibration methodology by utilizing a new design of phantoms to mimic human skin and a normalization that makes measurement independent of sample distance from the detector. This work is described in Chapter 2.

Objective 2: The system was validated to demonstrate its accuracy by measuring Fe concentration in the skin of healthy normal pigs. XRF results were compared with the

inductively coupled plasma mass spectroscopy (ICP-MS) measurements performed by an independent commercial company (Kinectrics Inc, Mississauga, Ontario). This work is described in Chapter 3.

Objective 3: Studies of rat skin demonstrated that the system could determine whether Fe dosed animals were from Fe overload or normal treatment groups and, further, was able to identify the specific treatment group of animals from measurement of skin alone. This work was accomplished by comparison of PXRF measurements of excised rat skin against results obtained with an 'in house' laboratory based XRF system. This work is described in Chapter 4.

Objective 4: The effect on a PXRF measurement of the variability/heterogeneity of Fe distribution in human skin was modelled using Monte Carlo simulation and the results were found to compare well to experiment validation studies. This work is described in both Chapters 3 and 4.

Bibliography

[1] A. J. Schwartz *et al.*, "Hepatic hepcidin/intestinal HIF-2α axis maintains iron absorption during iron deficiency and overload," *J. Clin. Invest.*, vol. 129, no. 1, pp. 336–348, Jan. 2019, doi: 10.1172/JCI122359.

[2] "Hemochromatosis - Canadian Liver Foundation." https://www.liver.ca/patients-caregivers/liverdiseases/hemochromatosis/(accessed Jun. 16, 2023).

[3] E. P. Vichinsky, E. A. MacKlin, J. S. Waye, F. Lorey, and N. F. Olivieri, "Changes in the Epidemiology of Thalassemia in North America: A New Minority Disease," *Pediatrics*, vol. 116, no. 6, pp. e818–e825, Dec. 2005, doi: 10.1542/PEDS.2005-0843.

[4] F. A. Sayani and J. L. Kwiatkowski, "Increasing prevalence of thalassemia in America: Implications for primary care," *https://doi.org/10.3109/07853890.2015.1091942*, vol. 47, no. 7, pp. 592–604, Oct. 2015, doi: 10.3109/07853890.2015.1091942.

[5] E. Dao, M. P. Zeller, B. C. Wainman, and M. J. Farquharson, "Feasibility of the use of a handheld XRF analyzer to measure skin iron to monitor iron levels in critical organs," *J. Trace Elem. Med. Biol.*, vol. 50, pp. 305–311, Dec. 2018, doi: 10.1016/j.jtemb.2018.07.024.

[6] M. J. Farquharson and A. P. Bagshaw, "Monitoring body iron burden using X-ray fluorescence (XRF)," *Radiat. Phys. Chem.*, vol. 61, no. 3–6, pp. 599–601, Jun. 2001, doi: 10.1016/S0969-806X(01)00344-9.

[7] M. J. Farquharson, A. P. Bagshaw, J. B. Porter, and R. D. Abeysinghe, "The use of skin Fe levels as a surrogate marker for organ Felevels, to monitor treatment in cases of iron overload," *Phys. Med. Biol.*, vol. 45, no. 5, p. 1387, May 2000, doi: 10.1088/0031-9155/45/5/320.

[8] B. T. Paul, D. H. Manz, F. M. Torti, and S. V. Torti, "Mitochondria and Iron: Current Questions," *Expert Rev. Hematol.*, vol. 10, no. 1, p. 65, Jan. 2017, doi: 10.1080/17474086.2016.1268047.

[9] "Iron and iron deficiency - Better Health Channel." https://www.betterhealth.vic.gov.au/health/conditionsandtreatments/iron (accessed Jun. 25,

2023).

[10] N. Abbaspour, R. Hurrell, and R. Kelishadi, “Review on iron and its importance for human health,” *J. Res. Med. Sci.*, vol. 19, no. 2, p. 164, 2014, Accessed: Jun. 25, 2023. [Online]. Available: /pmc/articles/PMC3999603/.

[11] M. Godbold and P. D. McFarland, “Iron Overload,” *Essentials Blood Prod. Manag. Anesth. Pract.*, pp. 433–437, Apr. 2022, doi: 10.1007/978-3-030-59295-0_45.

[12] Y. Kohgo, K. Ikuta, T. Ohtake, Y. Torimoto, and J. Kato, “Body iron metabolism and pathophysiology of iron overload,” *Int. J. Hematol.*, vol. 88, no. 1, p. 7, Jul. 2008, doi: 10.1007/S12185-008-0120-5.

[13] E. Nemeth and T. Ganz, “The Role of Hepcidin in Iron Metabolism,” *Acta Haematol.*, vol. 122, no. 2–3, p. 78, Nov. 2009, doi: 10.1159/000243791.

[14] A. Pietrangelo, “Hereditary Hemochromatosis — A New Look at an Old Disease,” *https://doi.org/10.1056/NEJMra031573*, vol. 350, no. 23, pp. 2383–2397, Jun. 2004, doi: 10.1056/NEJMRA031573.

[15] B. K. CROWNOVER and C. J. COVEY, “Hereditary Hemochromatosis,” *Am. Fam. Physician*, vol. 87, no. 3, pp. 183–190, Feb. 2013, Accessed: Apr. 27, 2023. [Online]. Available: https://www.aafp.org/pubs/afp/issues/2013/0201/p183.html.

[16] W. S. Aronow, “Management of cardiac hemochromatosis,” *Arch. Med. Sci.*, vol. 14, no. 3, p. 560, 2018, doi: 10.5114/AOMS.2017.68729.

[17] “Patient education: Hereditary hemochromatosis (Beyond the Basics) - UpToDate.” https://www.uptodate.com/contents/hereditary-hemochromatosis-beyond-the-basics (accessed Jun. 26, 2023).

[18] A. T. Taher and A. N. Saliba, “Iron overload in thalassemia: different organs at different rates,” *Hematology*, vol. 2017, no. 1, pp. 265–271, Dec. 2017, doi: 10.1182/ASHEDUCATION-2017.1.265.

[19] E. Nemeth, “Hepcidin in β-thalassemia,” *Ann. N. Y. Acad. Sci.*, vol. 1202, p. 31, 2010, doi: 10.1111/J.1749-6632.2010.05585.X.

[20] A. Cao and R. Galanello, “Beta-thalassemia,” *Genet. Med.*, vol. 12, no. 2, pp. 61–76, Feb.

2010, doi: 10.1097/GIM.0B013E3181CD68ED.

[21] John Hopkins Medicine, "Beta Thalassemia | Johns Hopkins Medicine," *The Johns Hopkins University, The Johns Hopkins Hospital, and Johns Hopkins Health System*. https://www.hopkinsmedicine.org/health/conditions-and-diseases/beta-thalassemia (accessed Jun. 26, 2023).

[22] M. Rasel and S. K. Mahboobi, "Transfusion Iron Overload," *StatPearls*, Apr. 2023, Accessed: Jun. 26, 2023. [Online]. Available: https://www.ncbi.nlm.nih.gov/books/NBK562146/.

[23] S. Entezari *et al.*, "Iron Chelators in Treatment of Iron Overload," *J. Toxicol.*, vol. 2022, 2022, doi: 10.1155/2022/4911205.

[24] "Ferritin test - Mayo Clinic." https://www.mayoclinic.org/tests-procedures/ferritin-test/about/pac-20384928 (accessed Jun. 17, 2023).

[25] E. Poggiali, E. Cassinerio, L. Zanaboni, and M. D. Cappellini, "An update on iron chelation therapy," *Blood Transfus.*, vol. 10, no. 4, p. 411, 2012, doi: 10.2450/2012.0008-12.

[26] M. Ali, M. A. Yassin, and M. Aldeeb, "Iron Overload in a Patient with Non-Transfusion-Dependent Hemoglobin H Disease and Borderline Serum Ferritin: Can We Rely on Serum Ferritin for Monitoring in This Group of Patients?," *Case Rep. Oncol.*, vol. 13, no. 2, p. 668, 2020, doi: 10.1159/000507653.

[27] J. C. Wood, "Guidelines for quantifying iron overload," *Hematology*, vol. 2014, no. 1, pp. 210–215, Dec. 2014, doi: 10.1182/ASHEDUCATION-2014.1.210.

[28] J. C. Wood, "Magnetic resonance imaging measurement of iron overload," *Curr. Opin. Hematol.*, vol. 14, no. 3, p. 183, May 2007, doi: 10.1097/MOH.0B013E3280D2B76B.

[29] U. Tipnis and A. Joshi, "Magnetic resonance imaging (MRI)," in *ISA TECH/EXPO Technology Update Conference Proceedings*, 2001, vol. 416, pp. 339–348, doi: 10.1007/978-3-319-61540-0_9.

[30] J. M. Alústiza Echeverría, A. Castiella, and J. I. Emparanza, "Quantification of iron concentration in the liver by MRI," *Insights Imaging*, vol. 3, no. 2, pp. 173–180, May

2012, doi: 10.1007/S13244-011-0132-1/FIGURES/7.

[31] R. Labranche *et al.*, "Liver Iron Quantification with MR Imaging: A Primer for Radiologists," *https://doi.org/10.1148/rg.2018170079*, vol. 38, no. 2, pp. 392–412, Mar. 2018, doi: 10.1148/RG.2018170079.

[32] E. Angelucci *et al.*, "Limitations of Magnetic Resonance Imaging in Measurement of Hepatic Iron," *Blood*, vol. 90, no. 12, pp. 4736–4742, Dec. 1997, doi: 10.1182/BLOOD.V90.12.4736.

[33] H. Bin Na, I. C. Song, and T. Hyeon, "Inorganic Nanoparticles for MRI Contrast Agents," *Adv. Mater.*, vol. 21, no. 21, pp. 2133–2148, Jun. 2009, doi: 10.1002/ADMA.200802366.

[34] A. Venter, D. A. Szulc, S. Loai, T. Ganesh, I. E. Haedicke, and H. L. M. Cheng, "A manganese porphyrin-based T1 contrast agent for cellular MR imaging of human embryonic stem cells," *Sci. Reports 2018 81*, vol. 8, no. 1, pp. 1–11, Aug. 2018, doi: 10.1038/s41598-018-30661-w.

[35] R. Newrock, "What are Josephson junctions? How do they work? - Scientific American," *Scientific American*, 1997. https://www.scientificamerican.com/article/what-are-josephson-juncti/ (accessed Aug. 06, 2023).

[36] M. Weyhmiller *et al.*, "Liver Iron Concentration Assessed by SQUID Biosusceptometry Compared to Heat-dried Liver Biopsy: A Blinded Study," 2021, doi: 10.21203/rs.3.rs-1135845/v1.

[37] N. Milman, J. Laursen, J. Pødenphant, and P. Staun-Olsen, "Iron, copper, zinc and selenium in human liver tissue measured by x-ray fluorescence spectrometry," *Scand. J. Clin. Lab. Invest.*, vol. 43, no. 8, pp. 691–697, 1983, doi: 10.1080/00365518309168851.

[38] R. Zeimer, M. Belkin, E. Leitersdorff, and E. A. Rachmilewitz, "A noninvasive method for the evaluation of tissue iron deposition in beta-thalassemia major.," *J. Lab. Clin. Med.*, vol. 91, no. 1, pp. 24–31, Jan. 1978, Accessed: Jul. 02, 2023. [Online]. Available: https://europepmc.org/article/med/618988.

[39] R. Gorodetsky, A. Goldfarb, I. Dagan, and E. A. Rachmilewitz, "Noninvasive analysis of skin iron and zinc levels in β-thalassemia major and intermedia," *J. Lab. Clin. Med.*, vol.

105, no. 1, pp. 44–51, Jan. 1985, doi: 10.5555/URI:PII:0022214385900873.

[40] M. M. Friedlaender, B. Kaufman, D. Rubinger, J. Moreb, M. M. Popovtzer, and R. Goredetsky, "Noninvasive Assessment of Skin Iron Content in Hemodialysis Patients. An Index of Parenchymal Tissue Iron Content?," *Am. J. Kidney Dis.*, vol. 12, no. 1, pp. 18–25, Jul. 1988, doi: 10.1016/S0272-6386(88)80066-0.

[41] R. GORODETSKY, E. LOEWENTHAL, A. GOLDFARB, and E. A. RACHMILEWITZ, "Non-Invasive Evaluation of Iron Load and Clearance in Patients with β-Thalassemia," *Ann. N. Y. Acad. Sci.*, vol. 612, no. 1, pp. 568–572, 1990, doi: 10.1111/J.1749-6632.1990.TB24369.X.

[42] M. Estevam and C. R. Appoloni, "Use of portable x-ray fluorescence (PXRF) in vivo as an alternative technique for the assessment of iron levels in patients with thalassemia and hemochromatosis," *Health Phys.*, vol. 104, no. 2, pp. 132–138, Feb. 2013, doi: 10.1097/HP.0B013E3182667721.

[43] A.-L. Manninen, "Clinical applications of radiophotoluminescence (RPL) dosimetry in evaluation of patient radiation exposure in radiology : determination of absorbed and effective dose."

[44] S. Naeem Ahmed, "Physics and engineering of radiation detection," *Choice Rev. Online*, vol. 45, no. 02, pp. 45-0892-45–0892, 2007, doi: 10.5860/choice.45-0892.

[45] J. E. Turner, *Atoms, Radiation, and Radiation Protection: Third Edition*. Wiley-VCH, 2007.

[46] K. Debertin and R. Helmer, "Gamma-and X-ray spectrometry with semiconductor detectors," 1988, Accessed: Jun. 29, 2023. [Online]. Available: https://inis.iaea.org/search/search.aspx?orig_q=RN:20046286.

[47] G. E. Knoll, A. Arbor, and J. Wiley, "Radiation Detectibn and Measurement Third Edition," 2000.

[48] E. Samei and D. J. Peck, "Hendee's physics of medical imaging," *Hendee's Phys. Med. Imaging*, pp. 1–469, Jan. 2019, doi: 10.1002/9781118671016/FORMAT/EPUB.

[49] "NIST XCOM: Element/Compound/Mixture."

https://physics.nist.gov/PhysRefData/Xcom/html/xcom1.html (accessed Sep. 12, 2022).

[50] J. H. Hubbell, "Photon Mass Attenuation and Mass Energy-Absorption Coefficients for H, C, N, O, Ar, and Seven Mixtures from 0.1 keV to 20 MeV," *Radiat. Res.*, vol. 70, no. 1, pp. 58–81, Apr. 1977, doi: 10.2307/3574732.

[51] "What is X-ray Fluorescence (XRF) - HORIBA." https://www.horiba.com/gbr/scientific/technologies/energy-dispersive-x-ray-fluorescence-ed-xrf/what-is-x-ray-fluorescence-xrf/ (accessed Apr. 30, 2023).

[52] R. Jenkins and J. L. De Vries, "Practical X-Ray Spectrometry," *Pract. X-Ray Spectrom.*, 1970, doi: 10.1007/978-1-349-00055-5.

[53] "Composition of SKIN (ICRP)." https://physics.nist.gov/cgi-bin/Star/compos.pl?matno=250 (accessed Aug. 18, 2023).

[54] H. A. E. Benson and A. C. Watkinson, "Transdermal and Topical Drug Delivery: Principles and Practice," *Transdermal Top. Drug Deliv. Princ. Pract.*, Jan. 2012, doi: 10.1002/9781118140505.

[55] E. D. Desouza *et al.*, "Characterization of the depth distribution of Ca, Fe and Zn in skin samples, using synchrotron micro-x-ray fluorescence (SμXRF) to help quantify in-vivo measurements of elements in the skin," *Appl. Radiat. Isot.*, vol. 77, pp. 68–75, Jul. 2013, doi: 10.1016/J.APRADISO.2013.02.019.

[56] "Auger Effect." http://hyperphysics.phy-astr.gsu.edu/hbase/Atomic/auger.html (accessed Jul. 14, 2023).

[57] R. van (René) Grieken and A. Markowicz, *Handbook of X-ray spectrometry*. Marcel Dekker, 2002.

[58] J. L. Campbell, "Fluorescence yields and Coster-Kronig probabilities for the atomic L subshells. Part II: The L1 subshell revisited," *At. Data Nucl. Data Tables*, vol. 95, no. 1, pp. 115–124, 2009, doi: 10.1016/J.ADT.2008.08.002.

[59] S. R. Cherry, J. A. Sorenson, and M. E. Phelps, "Pulse-Height Spectrometry," *Phys. Nucl. Med.*, pp. 141–154, 2012, doi: 10.1016/B978-1-4160-5198-5.00010-1.

[60] D. S. McGregor and J. K. Shultis, "Radiation Detection : Concepts, Methods, and

Devices," Aug. 2020, doi: 10.1201/9781439819401.

[61] "Semiconductor Band Gaps." http://hyperphysics.phy-astr.gsu.edu/hbase/Tables/Semgap.html (accessed Jul. 13, 2023).

[62] E. Gatti and P. Rehak, "Semiconductor drift chamber — An application of a novel charge transport scheme," *Nucl. Instruments Methods Phys. Res.*, vol. 225, no. 3, pp. 608–614, Sep. 1984, doi: 10.1016/0167-5087(84)90113-3.

[63] "A Comparison Between SDD and PIN Detector." https://www.azom.com/article.aspx?ArticleID=19338 (accessed Dec. 09, 2021).

[64] "VITUS H150 - Silicon Drift Detector (SDD) - KETEK GmbH." https://www.ketek.net/sdd/vitus-sdd-modules/vitus-h150/ (accessed May 04, 2023).

[65] E. Desouza, "COMPARISON OF METHODS FOR DETECTION OF ARSENIC IN SKIN USING XRF," 2014.

[66] W. Kenton, "Monte Carlo Simulation: History, How it Works, and 4 Key Steps," *Investopedia*, 2022. https://www.investopedia.com/terms/m/montecarlosimulation.asp (accessed Aug. 20, 2023).

[67] D. W. O. Rogers, "Monte Carlo Techniques in Radiotherapy," *Med. Phys. Spec. Issue*, vol. 58, no. 2, pp. 63–70, 2002, Accessed: May 30, 2023. [Online]. Available: http://www.irs.inms.nrc.ca/inms/irs/irs.html.

[68] H. Hirayama, Y. Namito, A. F. Bielajew, S. J. Wilderman, and W. R. Nelson, "THE EGS5 CODE SYSTEM 1," Accessed: May 28, 2023. [Online]. Available: http://www.kek.jp.

[69] C. John *et al.*, "Title: MCNP Version 6.2 Release Notes Intended for."

[70] M. Asai, "INTRODUCTION TO GEANT4."

[71] H. Hirayama, Y. Namito, A. F. Bielajew, S. J. Wilderman, and W. R. Nelson, "THE EGS5 CODE SYSTEM 1," Accessed: May 09, 2023. [Online]. Available: http://www.kek.jp.

[72] M. Zamburlini, A. Pejović-Milić, and D. R. Chettle, "Coherent normalization of finger strontium XRF measurements: Feasibility and limitations," *Phys. Med. Biol.*, vol. 53, no. 15, Aug. 2008, doi: 10.1088/0031-9155/53/15/N02.

[73] Y. Namito, H. Hirayama, and S. Ban, "KEK, Tsukuba, Japan The First International Workshop on EGS4 was held at KEK during August 26-29, 1997 and the Second International Workshop on EGS was held at KEK during," 2005.

Chapter 2

2.1 Summary of Papers

The goal of this research is to develop and validate an XRF system that would be portable and could be used to accurately measure skin iron concentrations in patients suffering from Fe overload and Fe deficiency. The core of this research is presented in the following three chapters, with each chapter dedicated to one of three papers. These papers represent crucial milestones in the thesis' development. The journey begins with the introduction and development of an XRF detection system, specifically designed for the measurement of Fe levels in the skin. It continues with studies aimed at the validation of the XRF system by comparison of XRF and ICP-MS measurements on the pigskin samples and ends with testing of the systems ability to distinguish Fe levels in the skin of rats under normal and Fe overloaded conditions. To guide the reader, each chapter is preceded by a project summary, offering an overview of the research and highlighting my contributions to each aspect of the project.

The three papers concentrate on the development of a PXRF-based detection system comprised of a ^{109}Cd excitation source and a silicon drift detector. As previously mentioned, this system was subsequently employed to perform *ex vivo* measurements of Fe in the skins of pigs and rats. In the first publication presented in this thesis (Paper I), a phantom-based study was conducted to measure skin Fe concentration. The study utilized water-based phantoms to determine the Minimum Detectable Limit (MDL) of the system. These phantoms were printed shells of polylactic acid (PLA) plastic filled with solutions of increasing Fe concentrations, coupled with a silicon drift detector system. The paper explored the feasibility of normalization of Fe K_α X-rays to nickel K_α X-rays to address changes in sample position during phantom measurements. The findings from this study suggest that an XRF detection system is feasible and with further development has potential

to conduct Fe measurements in the skin of patients with Fe overload and Fe deficiency in clinical settings. Nevertheless, the system's performance and accuracy must undergo further testing before being employed for *in vivo* measurements on human skin. The system performance and accuracy are then tested in the second and third publications in this thesis (Papers II and III).

Paper II discusses the cross-validation of the PXRF system against the commonly used benchmark of ICP-MS measurements which were performed by a commercial service. This validation was performed by measuring skin samples from pigs not loaded with iron, demonstrating the potential suitability of the PXRF system for human measurements. The paper additionally investigates the distribution of Fe in normal pig skin, which may influence measured XRF signals. The impact of Fe distribution on the measured XRF signal is further explored through Monte Carlo simulations. However, this research raised some questions regarding the distribution of Fe in the skin that need further exploration. The system performed well compared to ICP-MS measurements of normal pig skin samples, but there was a need to test the system's performance on Fe overload skin samples. In Paper III, the performance and accuracy of the PXRF system in rat skin samples from animals loaded with varying amounts of Fe are discussed. Further, the portable system measurements were validated against a laboratory-based XRF system. The study demonstrated that the PXRF could predict the Fe dosage level in the skin of animals from different groups of rats.

While the system demonstrated effective performance and was able to distinguish between Fe levels both in normal and Fe-overload skin samples, thus showing potential for measurement of skin Fe concentration in cases of Fe overload or deficiency, there are certain recommendations that must be taken into account before utilizing the system in clinical settings. These recommendations are discussed in Chapter 5 of this thesis.

2.2 Introduction to Paper I

Feasibility of a ^{109}Cd-based portable XRF device for measuring skin Fe concentration in anemic and β−Thalassaemic patients

[1]Sami Ullah Khan Bangash, [1]Fiona E McNeill, [2]Michael J Farquharson and [1]David R Chettle,

[1]Department of Physics and Astronomy, [2]School for Interdisciplinary Sciences, McMaster University, Hamilton, ON, L8S 4K1, Canada

Published in Biomed. Phys. Eng. Express 8 (2022) 065034

In this study, a detection system employing the XRF technique is utilized for the quantification of Fe X-rays in phantoms designed to simulate human skin. The detection system is comprised of a silicon drift detector, which has been adapted for PXRF applications to facilitate the assessment of Fe X-rays in patients' skin within clinical settings. An aluminum cap has been designed to safeguard the detector's sensitive Beryllium (Be) window and a 0.25 mm thick layer of styrene serves as a secondary window attached to the face of the aluminum window, further enhancing protection for the detector's Be window. While Kapton was initially considered for the role of a secondary window due to its common use as a window material, its higher density (1.42 gcm^{-3}) in comparison to styrene (0.91 gcm^{-3}) would lead to greater attenuation. Consequently, styrene was selected as the secondary window over Kapton to facilitate the passage of statistically significant Fe X-rays for measurement purposes.

The next step involved calibration of the main detector with phantoms. These new phantoms were printed in PLA plastic. The phantoms were filled with a $FeCl_3$ solution, and different phantoms were created with concentrations ranging from 0 to 150 ppm. During the calibration process, the activity of the excitation source was approximately 0.2 GBq.

The scattering of X-radiation within the sample and from the surroundings increases the background in the low energy region of the spectrum. To reduce the background, the source is enclosed in a tantalum collimator. Encasing the source in the collimator and the low activity of the source at the time of measurement reduces the number of incident radiations and so the measurement time was set to1800 seconds, enabling the more precise detection of prominent peaks in the Fe X-ray spectrum thus improving the performance of the detector system.

A Ni peak due to Ni in the detector material was used for normalization of the X-ray signal. The advantage of the normalization is evident from the system calibration lines. Regressions of Fe X-ray counts plotted against Fe concentration yielded a linear fit with χ^2 = 56.7 and R^2 = 0.982 and regression of the ratio of Fe X-ray/Ni X-ray against Fe concentration yielded $\chi 2$ = 6.54 and R2 = 0.997. Further, regression of the average Fe X-ray/Ni X-ray counts ratio (calculated from multiple phantom measurements) against Fe concentration, yielded a calibration line with a χ^2 value of 0.77 and R^2 = 0.999. This calibration line determines a MDL of 1.35 ± 0.35 ppm with a low radiation dose of 1.1 ± mSv to the skin surface.

The research presented in this first paper highlights the capability of the system to effectively conduct XRF measurements for skin Fe concentrations as assessed using these phantoms. The dose administered during the measurement has been established as safe, further indicating the system's suitability for practical application. Moreover, the portability of the system enables its convenient transportation to clinical settings for on-site measurements. However, the system's performance and accuracy require thorough evaluation, preferably through testing on skin samples, prior to its application in human measurements. This step is crucial to ensure the reliability and precision of the system in real-world scenarios. Therefore, testing and validation procedures, particularly on skin samples, are recommended as a prerequisite before the system is employed for human-centric measurements.

Michael Farquharson, David Chettle, and Fiona McNeill proposed this project as an initial phase in creating a system for the in vivo measurement of Fe. Fiona McNeill assisted in obtaining LiF chips for the dosimetry study mentioned in this paper and provided guidance on statistical tests. I independently handled the experiment design and phantom development under the guidance of my supervisors. I created the 3D printing phantom design, and phantoms were printed by Justin Bennet to my specifications. All spectral analysis was conducted by me using Origin Pro software, and I created calibration lines and estimates of MDL. I penned the initial draft of this paper which was reviewed and revised by the co-authors.

Corrigendum

After publication, the authors noticed an error in paper I, "Feasibility of a ^{109}Cd-based portable XRF device for measuring skin Iron concentration in anaemic and β−Thalassaemic patients" (Biomed. Phys. Eng. Express 8 (2022) 065034).
In the Discussion section of the paper, the following sentences are incorrect:

In addition, the Compton scattering of the 88 keV γ-rays in the phantom results in the production of electrons in the detector whose maximum energy is 22 keV. Therefore, after scattering, both the X- and γ-rays from ^{109}Cd do not contribute to the iron x-ray region background.

A corrigendum will be submitted to the journal asking for this paragraph to be changed to read as follows:

However, Compton scattering of the 88 keV γ-ray in the phantom can result in a backscattered photon of energy of 65.5 keV. It is possible for this scattered photon to undergo further Compton scattering in the detector, producing Compton scattered electrons with a maximum energy of 13.3 keV. These electrons result in an increase in the background under the Fe K_α X-ray. However, this is the only gamma-ray that is emitted by ^{109}Cd; it occurs in only 3.6% of decays; and the probability of a Compton scattering interaction of 65.5 keV γ-rays in the 0.450 mm thick silicon of the SDD is low, approximately 1.6%. The contribution to the background under the K_α X-ray peak is

relatively small. This is in contrast to sources like ^{238}Pu, where there are several X and γ-rays that can increase the background under Fe K_α due to the production of Compton-scattered electrons.

We will submit this correction to the Journal, and it will appear on the website of Biomedical Physics and Engineering Express.

PAPER • **OPEN ACCESS**

Feasibility of a ^{109}Cd-based portable XRF device for measuring skin iron concentration in anaemic and β−Thalassaemic patients

To cite this article: Sami Ullah Khan Bangash *et al* 2022 *Biomed. Phys. Eng. Express* **8** 065034

Biomedical Physics & Engineering Express

PAPER

Feasibility of a ^{109}Cd-based portable XRF device for measuring skin iron concentration in anaemic and β–Thalassaemic patients

Sami Ullah Khan Bangash , Fiona E McNeill, Michael J Farquharson and David R Chettle

Department of Physics and Astronomy, School for Interdisciplinary Sciences, McMaster University, Hamilton, ON, L8S 4K1, Canada

E-mail: bangashs@mcmaster.ca

Keywords: XRF, iron, minimum detectable limit

OPEN ACCESS

RECEIVED
23 June 2022

REVISED
30 September 2022

ACCEPTED FOR PUBLICATION
27 October 2022

PUBLISHED
8 November 2022

Abstract

Iron is an essential element vital for growth and development. The severe effects on the body due to iron deficiency or overload have prompted sustained research into accurate *in vivo* iron measurement techniques for the past several decades. X-ray fluorescence (XRF) analysis of iron in the body has been investigated in this work because of the non-invasive nature of the technique. A system has been designed using a silicon drift detector to measure the low-energy iron K_α x-rays excited in the samples by the silver x-rays from ^{109}Cd of energy 22 keV and 25 keV. The source is contained within a tantalum shielding cap designed to reduce the spectral background. The system was calibrated against 3D printed polylactic acid (PLA) phantoms filled with solutions of iron at various concentrations. The iron x-ray signals were normalized to a nickel x-ray signal which improved the system's reproducibility. The 3D phantoms and normalisation resulted in a linear calibration line ($p < 0.001$ and $r^2 > 0.999$). For a real-time measurement of 1800 s, the minimum detectable limit for the system was measured to be 1.35 ± 0.35 ppm which is achieved with a low radiation dose of 1.1 mSv to the skin surface. This low detection limit and low dose mean the system is feasible for application to human measurements in both iron deficiency and overload disease. The system will proceed to post-mortem validation studies prior to *in vivo* system efficacy testing.

1. Introduction

1.1. Iron overload and deficiency conditions

Iron is essential for humans and plays a vital role in the body's growth and development. Oxygen from the lungs is transported to the cells or tissues by iron [1]. It acts as a catalyst for many enzymes in the cell due to its occurrence in two stable oxidation states, the ferrous state (Fe^{+2}) and the ferric state (Fe^{+3}) [2]. The deficiency or excess of iron can result in different diseases. Thalassemia is an iron disorder in which the body cannot make enough haemoglobin in red blood cells. Patients suffering from Thalassemia need multiple blood transfusions that result in an accumulation of iron in critical organs. Hemochromatosis is another iron overload condition. In this disease, the body absorbs too much iron from food. The extra iron is stored mainly in the liver, heart and pancreas, causing damage to these organs [3]. Currently, clinicians use blood tests to assess patients, but the accurate measurement of stored iron, the iron body burden, would provide additional important clinical information. The alternative currently available methods of measuring iron all have their limitations. Serum ferritin values can be readily assessed but can vary due to infection or inflammation in the body [4]. The liver can be biopsied with low risk: the mortality rate in liver biopsy is 0.01%–0.17% [5]. However, the heterogeneity of the distribution of iron in the liver and the sampling error are limitations of this method [6, 7]. In addition, liver biopsy is not recommended in patients with a risk of uncontrolled bleeding due to myelodysplastic syndrome [8]. Superconducting quantum interference devices (SQUIDs) have been shown to accurately measure iron in the liver and spleen, but this method is expensive and rarely available [9]. Studies have shown that measuring the iron level in the skin is a good surrogate for measuring the stored iron in the liver [10, 11].

A portable device that could quickly assess blood and skin iron levels in real-time could thus be convenient and useful for clinicians. This manuscript describes the development of such an iron measurement system.

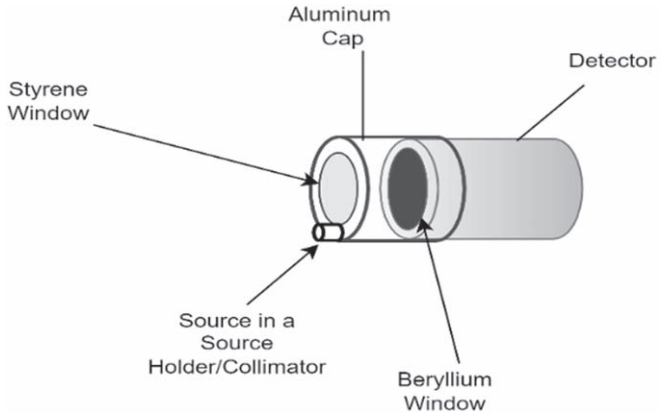

Figure 1. Aluminium cap for the detector with styrene window and collimator glued on the front face.

1.2. X-ray Fluorescence (XRF)

The technique of bulk x-ray Fluorescence (XRF) has been used to measure lead in bone [12–14] and cadmium and Mercury in the kidney and liver [15, 16], *in vivo* measurement of manganese and Mercury in toenails [17], *in vivo* quantification of strontium in bones [18]. In recent years there has been focus on the development of the systems to permit *in vivo* XRF imaging [19–21]. Previously, other authors have demonstrated the potential of devices to measure iron levels *in vivo* by XRF. However, high detection limits meant their research could only focus on assessment in the range from normal to iron overload [22, 23]. This work aims to improve the detection limit and provide a faster measurement with a portable device that would measure the iron levels over the entire clinical range from iron deficit anaemia to iron overload.

Previous studies that showed the iron body burden is proportional to the concentration of iron in the skin were performed using XRF [22, 24, 25]. This work uses the same technique, employing a silicon drift detector (SDD) to measure the iron K-shell characteristic x-rays. This detector was used because the SDD is a semiconductor detector that can deal with high count rates, has good energy resolution, and is efficient for detecting low-energy x-rays.

2. Methods and materials

2.1. Silicon drift detector

A KETEK VITUS H150 x-ray silicon drift detector was used in the experiment. The detector has an excellent energy resolution of $\leqslant$ 136 eV even at very short rise times down to 0.1 μs. The detector has a 170 mm^2 SDD chip collimated down to a 150 mm^2 active area. SDD detectors such as this can deal with very high-count rates up to 2 Mcps and have a high peak to background ratio of $\geqslant$ 15,000.

2.2. Styrene window

A new aluminium cap has been developed for this instrument, as shown in figure 1. A 0.25 mm thick styrene window is glued on the open end of the aluminium cap to protect the delicate beryllium window on the detector. The protective layer does mean detection losses but this styrene window allows almost 80 percent transmission of iron K_α (6.4 keV) x-rays.

2.3. ^{109}Cd Source

A ^{109}Cd source is used for the excitation of iron atoms in phantoms. ^{109}Cd decays by an electron capture with a half-life of 464 days to an isomeric state of ^{109}Ag. The ^{109}Ag nucleus then decays by emitting 88 keV γ-rays. The vacancy created in the shell as a result of electron capture by a ^{109}Cd nucleus results in the emission of 22.1 keV and 24.9 keV characteristic x-rays of silver atoms, figure 2 shows the decay scheme of 109Cd. The source capsule is cylindrical, having a diameter and height each of 3mm. The source activity is described as being 0.2 GBq (7.2 mCi) on 16th June 2021. However, this means that the emitted fluence of 88 keV γ-rays at the source surface is equivalent to the fluence from a bare 0.2 GBq ^{109}Cd source. The source is encapsulated with a 100 μm titanium window. The ^{109}Cd is plated onto a silver metal matrix which is 30 μm thick with a 1 mm active diameter. There is attenuation through the encapsulation and the source material itself. The silver x-ray fluence is, therefore, approximately a factor of four less than would be expected from a bare ^{109}Cd source.

The measured backscatter spectrum when an iron-doped water phantom was excited using ^{109}Cd is shown in figure 3. This figure also shows the additional x-ray transitions observed in the spectrum arising from the photoelectric effect in other elements. The titanium K_α and K_β peaks are from the source capsule material. A nickel peak is observed in the spectrum due to the presence of nickel in the detector capsule. The magnitude of this nickel peak is dependent on the backscatter fluence incident on the detector. The iron

Type of Radiation	Intensity (%)	Energy of Radiation (keV)
Auger-L	87	2.6
Auger-K	13.4	18.5
X-ray L	5.8	3
X-ray $K_{\alpha 2}$	18.6	21.99
X-ray $K_{\alpha 1}$	35.3	22.16
X-ray K_{β}	11.4	24.9

^{109}Ag IT Decay Mode (39.6 s)

Type of Radiation	Intensity (%)	Energy of Radiation (keV)
X-ray $K_{\alpha 2}$	9.9	21.99
X-ray $K_{\alpha 1}$	18.7	22.16
X-ray K_{β}	6.03	24.9
γ	3.72	88.03

Figure 2. Decay scheme of ^{109}Cd showing the relevant energies only [26].

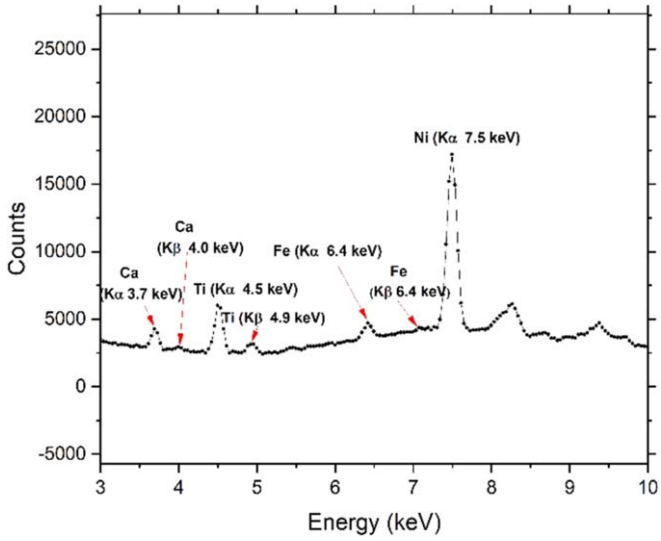

Figure 3. The obtained spectrum when a cylindrical plastic water phantom doped with iron is excited using the ^{109}Cd source. (K-edge energies of the elements in the graph are Ca = 4.038 keV, Ti = 4.966 keV, Fe = 7.112 keV and Ni = 8.333 keV [27]).

K x-ray peak area and the nickel x-ray peak area vary in exactly the same way with changes in source-detector-sample distance. The iron signal can thus be normalized to the nickel signal to account for small changes in distance. The titanium peak could also theoretically be used for normalization, but the current

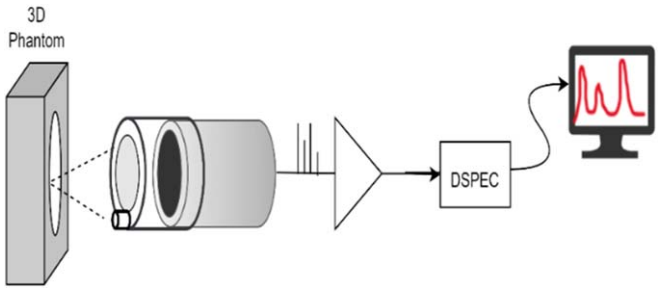

Figure 4. Experimental arrangement for the measurement of iron x-rays.

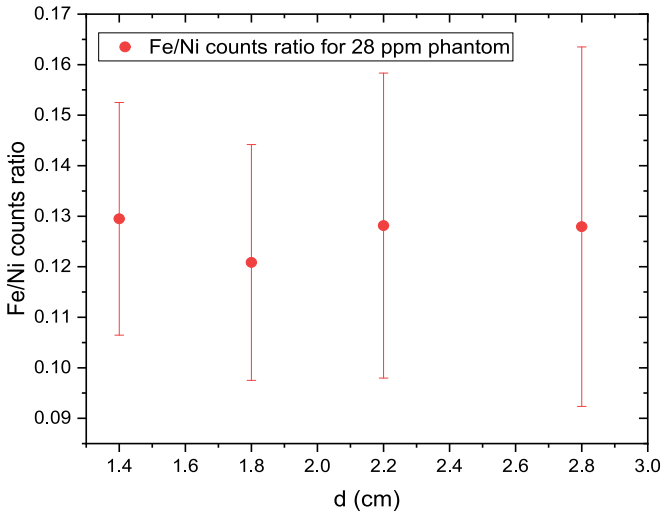

Figure 5. Graph plotted for the ratio of Fe/Ni counts of a 28 ppm phantom at different distances from the detector. The ratio does not change with distance, suggesting the normalization of Fe/Ni will reduce the effects of positioning and motion.

study utilizes the nickel K_α peak because it is more evident in the spectrum.

2.4. Phantoms and source holder/collimator

An initial set of iron-doped water-based phantoms was developed. These phantoms were initially used in experiments to explore the best materials for the source holder/collimator. The phantoms were cylindrical plastic containers of a volume 25 ml with a 4 μm thin film (3525 Ultraline) window. The system was set up in backscattering geometry. Phantoms were measured for a live time of 1800 s.

The XRF spectrum was analyzed using OriginPro® software, where a mathematical model was fitted to the spectrum. The iron x-ray peaks were fitted using Gaussian functions, and the area of the Gaussian was used as the estimate of the iron signal. As previously mentioned, the prominent nickel peak arising from nickel in the detector capsule is used to normalize measurements. As shown below we determined that the normalization of the iron x-ray signal to the nickel x-ray signal creates a more robust measurement system where the accuracy is not strongly dependent on phantom distance from the detector. The iron and the nickel signals vary in the same way with distance, so while the individual signals can vary, the ratio of iron to nickel x-ray signals remains constant. The measurement accuracy is thus not dependent on distance, although the measurement precision does, of course, vary. The normalization also corrects for the decay of the radioactive source.

Figure 5 shows plot of the Fe/Ni signal ratio for different distances (d) of a 28 ppm phantom from the detector. The distances are measured from the styrene window to the phantom. As shown, the ratio of Fe/Ni signals for a 28 ppm phantom does not change significantly over distances between 1.4 and 2.8 cm of the phantom from the detector. The normalization thus accounts for changes in phantom distance. This will be important while taking measurements on human volunteers, where it is not easy to exactly position the person and keep them completely still though the measurement.

The spectral background is reduced by using a source holder/collimator. After testing several materials, lead and tantalum were found to be excellent source holder/collimator materials. A 1 mm thick and 3 mm long cylindrical tantalum holder/collimator is currently used in experiments.

At this stage in the system development, a new set of iron phantoms was created using holders made via 3D printing. These were hollow square phantoms,

filled with iron-doped solutions of various concentrations, with a 4 μm thin film (3525 Ultraline) holding the solution in the phantom. The phantom material is thus iron-doped water solution which is measured through a 4 μm thin window. This phantom design was used for all further experiments because it was more stable when placed in position, easier to fill, and less prone to leakage.

2.5. Experiment

The schematic diagram of the experimental setup is shown in figure 4. The 3D printed iron-doped water-based phantoms were placed at 2.6 cm from the Be window of the detector and irradiated with the collimated ^{109}Cd source. The collimator was attached to one side of the detector to attain a geometry close to 180 degrees while not covering any of the detector surface area. The iron x-rays were detected by the SDD and were fed as pulses to the preamplifier. The pulses from the preamplifier were processed by an Ortec Digital Gamma-Ray Spectrometer (DSPEC), and data were acquired and analyzed through Gamma Vision software. The average dead time for each phantom measurement was low, approximately 11 percent.

3. Dosimetry

The radiation dose delivered by the system was estimated in two ways.

The dose from an 1800 s live time measurement was estimated using the formula [28],

$$\dot{D} = \dot{\Phi}\, h\upsilon\, \frac{\mu_{en}}{\rho} \tag{1}$$

Where $\dot{D}$ is the dose rate, $\dot{\Phi}$ is the fluence rate, $h\upsilon$ is the photon energy and $\frac{\mu_{en}}{\rho}$ is the mass energy absorption coefficient for soft tissue. Fluence rate was estimated from the known source strength and corrected for attenuation through the source matrix and encapsulation. We used the design drawings from the manufacturer to estimate material thicknesses and mass attenuation coefficients from NIST data tables [29] in the attenuation calculations. We assumed that the 1 mm active area of source could be considered a spot source and used the source to skin distance, irradiation area and manufacturer measured fluence rate of the 88 keV photons at 1 metre to calculate the 88 keV fluence rate. The relative emission probabilities for 22 keV, 25 keV and 88 keV photons were then used to calculate the 22 keV and 25 keV photon fluence rates with attenuation through source materials taken into account. The relative γ- and x-ray emission probabilities were those published in Xialong *et al* 2010 [30]. Fluence was then estimated from the fluence rate using the measured real measurement time estimated by the Gamma Vision software for a live measurement time of 1800 s. Mass energy absorption coefficients for 22 keV, 24 keV and 88 keV in ICRU-44 soft tissue were calculated from the NIST mass attenuation and mass-energy absorption coefficient tables [29].

The dose was measured using lithium fluoride (LiF) dosimeters from Mirion Technologies. These were placed in an array corresponding to the area on the phantom expected to be irradiated. They were irradiated for 17 h and then shipped back to Mirion Technologies for reading, who provided a dose estimate from calibration against appropriate standards.

4. Results

4.1. Calibration line and minimum detectable limit

Each 3D phantom was measured for 1800 s. We measured phantoms with concentrations from 0 to 150 ppm. Each phantom was measured five times. After each individual measurement the phantom was removed then placed back in position in order to obtain an estimate of the reproducibility of this simple measurement arrangement.

Figure 6(A) shows the calibration plot of individual iron x-ray counts versus concentration in ppm, while figure 6(B) shows the calibration plot of the individual iron/nickel x-ray count ratios versus concentration in ppm. Figure 6(C) shows the plot of the average iron/nickel x-ray count versus concentration. The calibration line of the average Fe-K_α/Ni-K_α counts against the concentration in parts per million (ppm) as shown in figure 6(C) shows excellent linearity with $p < 0.001$ and $r^2 > 0.999$. The variation in the iron/nickel ratio is explained almost entirely by the variation in concentration.

As can be seen from the curves in figures 6(A) and (B), the plot of the iron/nickel ratio versus concentration provides a more robust and reproducible calibration line than the plot of iron x-ray signal versus concentration. The ratio is less subject to changes in position than the iron x-ray signal alone. Repeated measurements of the 150 ppm phantom determined that using the iron x-ray peak area alone, the standard deviation of the signal estimates was 12%. This is larger than would be expected from Poisson statistical fluctuations, as slight differences in phantom position also affect the data. Using the iron/nickel ratio, the standard deviation of the estimates was found to be 4%. This is lower because the Fe/Ni ratio is unchanged with position, and effects resulting from variations in positioning are reduced. The use of the normalization does, therefore, appear to result in a more reproducible measurement system.

The minimum detectable limit (MDL) was calculated from the uncertainty of the ratio of the iron K_α x-ray area to nickel x-ray peak area of the 0 ppm phantom using the following relationship

$$\mathrm{MDL} = \frac{2 \times \sigma_{0ppm}}{\mathrm{m}} \tag{2}$$

Where, $\sigma_{0\mathrm{ppm}}$ is the uncertainty in the 0 ppm phantom, and m is the slope of the calibration line. The K_β iron x-ray is not used because of its low intensity. From measurements of the 0 ppm phantom and the

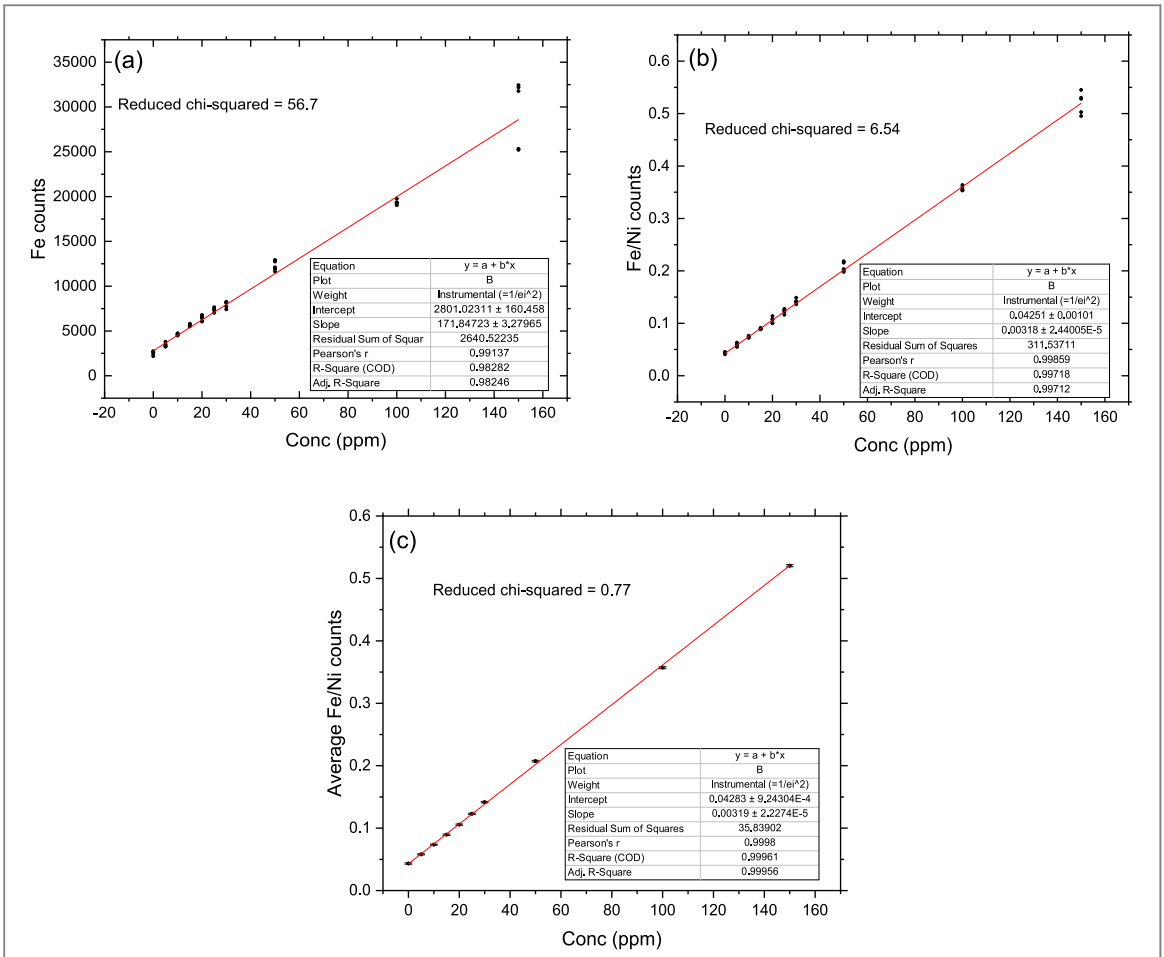

Figure 6. (A) Calibration line for individual iron counts against concentration in ppm. (B) Calibration line for Fe/Ni counts against concentration. The line shows improved r^2 when plotting the ratio of Fe to Ni against concentration. (C) Calibration line obtained for 3D PLA-based water phantoms. The calibration is strongly linear ($p < 0.001$), and individual phantom measurements are highly reproducible.

calibration line, the instrumental detection limit of this iron measurement system is estimated as 1.35 ± 0.35 ppm

For a straight line $y = mx + c$ and the measured $y \pm \delta y$, an estimate of the unknown $\hat{x}$ is given by

$$\hat{x} = \frac{(y - c)}{m} \tag{3}$$

Where m is the slope and c is the y-intercept of the line. The uncertainty $\sigma^2_{\hat{x}}$ in the estimated value of $\hat{x}$, is given as

$$\sigma^2_{\hat{x}} = \left(\frac{\partial \hat{x}}{\partial y}\right)^2 \sigma^2_y + \left(\frac{\partial \hat{x}}{\partial c}\right)^2 \sigma^2_c + \left(\frac{\partial \hat{x}}{\partial m}\right)^2 \sigma^2_m + 2\left(\frac{\partial \hat{x}}{\partial y}\right)\left(\frac{\partial \hat{x}}{\partial c}\right) COV_{y,c} + 2\left(\frac{\partial \hat{x}}{\partial y}\right)\left(\frac{\partial \hat{x}}{\partial m}\right) COV_{y,m} + 2\left(\frac{\partial \hat{x}}{\partial m}\right)\left(\frac{\partial \hat{x}}{\partial c}\right) COV_{m,c}$$

Where, COV is the covariance, σ_m and σ_c represent the uncertainties in slope and intercept.

However, $COV_{y,c} = COV_{y,m} = 0$ and

$$\left(\frac{\partial \hat{x}}{\partial y}\right) = \frac{1}{m}; \left(\frac{\partial \hat{x}}{\partial c}\right) = -\frac{1}{m}; \left(\frac{\partial \hat{x}}{\partial c}\right) = -\frac{(y - c)}{m^2}$$

so the above equation is reduced to

$$\sigma^2_{\hat{x}} = \frac{1}{m^2}\sigma^2_y + \frac{1}{m^2}\sigma^2_c + \frac{(y - c)^2}{m^4}\sigma^2_m + 2\frac{(y - c)}{m^3} COV_{m,c} \tag{4}$$

The above equation describes the calculation of the uncertainty in the estimated value of x.

4.2. Radiation dosimetry

The estimated skin dose for an 1800 s live time measurement from first principle calculations was 3.0 mSv and the measured dose estimate was 1.1 ± 0.1 mSv. The first principle calculation is an approximation, which did not include self-shielding within the source material, so was not expected to perfectly agree with the measured results. However, the similarity in estimates provided confidence in the measured value. The radiation dose to a 0.8 cm^2 area of the skin is

1.1 mSv for an individual measurement. This is comparable to the skin dose delivered by other *in vivo* XRF measurement systems [22, 31] which have been used in prior human studies. This level of dose has been considered ethical for use by human ethics review boards, being significantly less than, for example, the maximum permissible annual skin dose of 50 mSv permitted for members of the public in Canada [32]. The dose from this system is thus acceptable for human studies.

5. Discussion

Studies on patients have shown that the normal level of iron in the skin ranges from 5.6 ppm to 14 ppm, and for patients with β-thalassemia, it ranges from 13.7 ppm to 150 ppm [33]. The MDL of 1.35 $\pm$ 0.35 ppm of our system would be able to measure the skin iron levels in normal and overload ranges as attained by previous devices. However, this system is also likely able to measure levels in anaemic conditions.

Some of the reasons for the improved performance include the type of detector. The SDD has a better energy resolution ,40 eV lower than PIN detectors for the same active area [34]. This better energy resolution results in the SDD having a better detection limit with a low dose compared to previous studies [22, 35]. In addition, the SDD can also deal with a higher count rate than Si-PIN detectors. This makes it possible to reduce the true measurement time when using a high activity source as there is less dead time. There are also fewer pulse pile-up losses.

Our selection of the silver x-rays from ^{109}Cd for excitation of samples may also be an important factor in our improved performance compared to other systems. There are a number of different sources and x-ray tubes that could be used for XRF. X-ray tubes with suitable currents and accelerating voltages can provide high fluence rates. Different studies have thus used x-ray tubes for in-vivo XRF measurement [36–38]. An advantage is that x-ray generators are compact and usually have a high fluence rate, and the x-ray field can be switched off which allows for simpler radiation protection. A disadvantage is the generation of Bremsstrahlung which can cause an increased background signal. High Bremsstrahlung fields are so intense that the signal to background ratio in the detector spectrum can be poorer. Discrete x or γ-ray sources are other options for XRF with the advantage of being small, easy to handle, and simple to operate. However, the use of a radioactive source means that radiation protection must be considered even when the machine is not in use. ^{109}Cd has proved to be an excellent choice of source. If the excitation x-rays (of energy 22 and 24 keV) are incoherently (Compton) scattered from the phantom, the signal registered by the detector does not affect the region of interest around the iron k x-rays. In addition, the Compton scattering of the 88 keV γ-rays in the phantom results in the production of electrons in the detector whose maximum energy is 22 keV. Therefore, after scattering, both the x- and γ-rays from ^{109}Cd do not contribute to the iron x-ray region background. This has permitted a better detection limit. Other studies [22] have used ^{238}Pu which has a lower excitation energy of 13 keV. This should provide an approximately factor of four improvement in the photoelectric cross-section compared to our system [32]. However, these authors reported a poorer detection limit and a higher dose. ^{238}Pu emits a series of x- and γ-rays. These create background in the iron x-ray region. For example, the ^{238}Pu 43.5 keV γ-ray can be backscattered and create Compton electrons in the detector in the iron x-ray region. In addition, the higher energy x- and γ-rays increase the dose, The 'cleaner' spectrum from ^{109}Cd confers a measurement advantage in that a lower dose can be delivered during the measurement and the iron x-ray signal extracted from a lower spectral background. The dose and detection limits are both low enough that the system could be used to study the skin iron concentration of volunteers.

This system employs a normalization by creating the calibration line by plotting the iron/nickel net peak areas against the phantom concentration. This normalization permits more flexibility in the position, improves the measurement reproducibility, and maintains the accuracy of the measurement. The data show that this normalization procedure should permit a robust *in vivo* measurement that would be independent of the distance between the hand and the source during measurements. This will become extremely important when the system moves on to *in vivo* measurements.

6. Conclusion

A new system with the potential for *in vivo* measurement of iron in the skin has been developed. The system's MDL of 1.35 $\pm$ 0.35 ppm in phantoms is low enough that the system is determined to be feasible for studies of skin iron levels *in vivo*. Further testing, including validation, is required before *in vivo* measurements can be performed. The current study has been performed on homogenous iron-doped water phantoms, but the distribution of iron in the skin and blood vessels and depth distribution of iron will complicate the measurements. Further studies, particularly on skin samples or volunteers, are required before the system can be considered for patients. However, the low detection limit, low dose, short counting time and portability of our instrument means it has good potential to ultimately enable clinicians to perform fast, in-office, non-invasive measurements of skin iron concentration in patients suffering from both iron overload and deficit conditions.

Acknowledgments

The authors thank Justin Bennett, who helped print the phantoms. The funding for the project was provided by the Natural Sciences and Engineering Research Council of Canada (NSERC), Research Tools and Instruments Grants.

Data availability statement

The data that support the findings of this study are available upon reasonable request from the authors.

ORCID iDs

Sami Ullah Khan Bangash https://orcid.org/0000-0003-3229-857X

References

[1] Shaffer C 2019 Iron functions in the body *News Medical Life Sciences* (https://news-medical.net/health/Iron-Functions-in-the-Body.aspx)accessed May 06, 2021
[2] Anderson G J and Vulpe C D 2009 The cellular physiology of iron in 'Iron Biochemistry and Metabolism' *Iron Deficiency and Overload* (Totowa, NJ: Humana Press) 3–29
[3] Powell L W, George D K, McDonnell S M and Kowdley K V 1998 Diagnosis of hemochromatosis *Ann. Intern. Med.* **129** 925–31
[4] Ill I C A V, Cob A J A and Woo R 1986 Diagnostic methods for iron status
[5] Grant A and Neuberger J 1999 Guidelines on the use of liver biopsy in clinical practice *Gut* **45** IV1–V1
[6] Wood J C *et al* 2005 MRI R2 and R2* mapping accurately estimates hepatic iron concentration in transfusion-dependent thalassemia and sickle cell disease patients *Blood* **106** 1460–5
[7] Obrzut M *et al* 2020 Value of liver iron concentration in healthy volunteers assessed by MRI *Sci. Reports 2020 101* **10** 1–8
[8] Hernando D, Levin Y S, Sirlin C B and Reeder S B 2014 Quantification of liver iron with MRI: state of the art and remaining challenges *J. Magn. Reson. Imaging* **40** 1003–21
[9] Crichton R 2016 *Iron Metabolism: From Molecular Mechanisms to Clinical Consequences* 4th edn (West Sussex, UK: Wiley)
[10] Farquharson M J, Bagshaw A P, Porter J B and Abeysinghe R D 2000 The use of skin Fe levels as a surrogate marker for organ Felevels, to monitor treatment in cases of iron overload *Phys. Med. Biol.* **45** 1387
[11] Youssry I *et al* 2009 *Skin Iron Concentration: a Simple, Highly Sensitive Method for Iron Stores Evaluation in Thalassemia Patients* **31** 357–65
[12] Hoppin J A, Aro A C A, Williams P L, Hu H and Ryan P B 1995 Validation of K-XRF bone lead measurement in young adults *Environ. Health Perspect.* **103** 78–83
[13] Nie H, Chettle D, Luo L and O'Meara J 2006 *In vivo* investigation of a new 109Cd γ-ray induced K-XRF bone lead measurement system *Phys. Med. Biol.* **51** 351
[14] Todd A C, McNeill F E and Fowler B A 1992 *In vivo* x-ray fluorescence of lead in bone *Environ. Res.* **59** 326–35
[15] Nilsson U, Ahlgren L, Christoffersson J-O and Mattsson S 1990 Further improvements of XRF analysis of cadmium *in vivo* *Basic Life Sci.* **55** 297–301
[16] Skerfving S *et al* 1987 Biological monitoring, by *in vivo* XRF measurements, of occupational exposure to lead, cadmium, and Mercury *Biol. Trace Elem. Res. 1987 131* **13** 241–51
[17] Specht A J *et al* 2021 Validation of *in vivo* toenail measurements of manganese and Mercury using a portable x-ray fluorescence device *J. Expo. Sci. Environ. Epidemiol. 2021 323* **32** 427–33
[18] Zhang X, Wells E M, Specht A J, Weisskopf M G, Weuve J and Nie L H 2022 *In vivo* quantification of strontium in bone among adults using portable x-ray fluorescence *J. Trace Elem. Med. Biol.* **74** 127077
[19] Jung S *et al* 2020 Dynamic *in vivo* x-ray fluorescence imaging of gold in living mice exposed to gold nanoparticles *IEEE Trans. Med. Imaging* **39** 526–33
[20] Hara D *et al* 2021 Prostate cancer targeted x-ray fluorescence imaging via gold nanoparticles functionalized with prostate-specific membrane antigen (PSMA) *Int. J. Radiat. Oncol.* **111** 220–32
[21] Shaker K *et al* 2020 Longitudinal in-vivo x-ray fluorescence computed tomography with molybdenum nanoparticles *IEEE Trans. Med. Imaging* **39** 3910–9
[22] Estevam M and Appoloni C R 2013 Use of portable x-ray fluorescence (PXRF) *in vivo* as an alternative technique for the assessment of iron levels in patients with thalassemia and hemochromatosis *Health Phys.* **104** 132–8
[23] Shukri A, Green S and Bradley D A 1995 A feasibility study: *In vivo* x-ray fluorescence of iron using 109Cd *Appl. Radiat. Isot.* **46** 625
[24] Farquharson M J and Bagshaw A P 2001 Monitoring body iron burden using x-ray fluorescence (XRF) *in Radiation Physics and Chemistry* **61** 599–601
[25] Dao E, Zeller M P, Wainman B C and Farquharson M J 2018 Feasibility of the use of a handheld XRF analyzer to measure skin iron to monitor iron levels in critical organs *J. Trace Elem. Med. Biol.* **50** 305–11
[26] Kocher D C 1981 Radioactive decay data tables
[27] NIST XCOM: Element/Compound/Mixture (https://physics.nist.gov/PhysRefData/Xcom/html/xcom1.html) accessed Sep. 12, 2022
[28] Turner J E 2007 *Atoms Radiation and Radiation Protection* 3rd edn (Weinheim, Germany: Wiley-VCH) 1–585
[29] Hubbell J H and Seltzer S M 1995 Tables of x-ray mass attenuation coefficients and mass energy-absorption coefficients from 1 keV to 20 MeV for Elements Z = 1 to 92 and 48 additional substances of dosimetric interest *National Inst. of Standards and Technology* PL Gaithersburg, MD (United States) Ionizing Radiation Div.
[30] Xiaolong H, Shenggui Y and Chunsheng D 2010 Evaluation of the decay data of 109Cd *Nucl. Instruments Methods Phys. Res. Sect. A Accel. Spectrometers, Detect. Assoc. Equip.* **621** 443–6
[31] Nie L H, Sanchez S, Newton K, Grodzins L, Cleveland R O and Weisskopf M G 2011 *In vivo* quantification of lead in bone with a portable x-ray fluorescence system—methodology and feasibility *Phys. Med. Biol.* **56** N39
[32] Radiation Protection Regulations 2022 (https://laws-lois.justice.gc.ca/eng/regulations/sor-2000-203/FullText.html) accessed Feb. 24
[33] Gorodetsky R, Goldfarb A, Dagan I and Rachmilewitz E A 1985 Noninvasive analysis of skin iron and zinc levels in β-thalassemia major and intermedia *J. Lab. Clin. Med.* **105** 44–51
[34] A Comparison Between SDD and PIN Detector 2021 (https://azom.com/article.aspx?ArticleID=19338)accessed Dec. 09
[35] Farquharson M J and Bradley D A 1999 The feasibility of a sensitive low-dose method for the *in vivo* evaluation of Fe in skin using K-shell x-ray fluorescence (XRF) *Phys. Med. Biol.* **44** 955
[36] Roy C W, Gherase M R and Fleming D E B 2010 Simultaneous assessment of arsenic and selenium in human nail phantoms using a portable x-ray tube and a detector *Phys. Med. Biol.* **55** N151
[37] Fleming D E B, Gherase M R and Alexander K M 2011 A miniature x-ray tube approach to measuring lead in bone using L-XRF *X-Ray Spectrom.* **40** 343–7
[38] Fleming D E B and Gherase M R 2007 A rapid, high sensitivity technique for measuring arsenic in skin phantoms using a portable x-ray tube and detector *Phys. Med. Biol.* **52** N459

Chapter 3

Paper II: Investigation of the Accuracy of a Portable ^{109}Cd XRF System for the Measurement of Fe in Skin

Sami Ullah Bangash[1], Fiona E McNeill[1], and Michael J Farquharson[2]

[1]Department of Physics and Astronomy, [2]School for Interdisciplinary Sciences, McMaster University, Hamilton, ON, L8S 4K1, Canada

3.1 Introduction to Paper II

This paper is a continuation of the work presented in Paper I, where I introduced the design of a PXRF system for the measurement of Fe in skin. The system's accuracy needed to be tested on skin before it could be used in human studies. This paper describes the validation of the PXRF system against ICP-MS measurements of the same skin samples and discusses the potential effect on the measurement accuracy of the distribution of Fe in the skin.

The system's accuracy is assessed by measuring the Fe content in ten skin samples from healthy pigs obtained (not dosed with Fe) from a local butcher. The results of the Fe levels in the pig skin samples, as measured using the PXRF, were then compared with the ICP-MS measurements.

Despite the variation in the depths measured into the samples by ICP-MS and XRF, the two techniques were found to be comparable on average to within 95% confidence intervals. However, a notable difference in Fe estimates between the two individual samples prompted us to conduct further investigations into the skin samples.

By chance, a different set of pig skin samples had been prepared for μXRF scanning multiple elements at the Bio-XAS beamline of the Canadian Light Source for a different project in our laboratory. The results were made available and revealed patterns of Fe distribution that I then simulated using the EGS5 Monte Carlo code.

I independently prepared the pig skin samples, performed the experiments, and subsequently analyzed the data, under the supervision of my advisors. Fiona McNeill obtained the skin samples and arranged for measurements of total Fe content by ICP-MS at the Analytical and Environmental Services Laboratory of Kinectrics Canada. Additionally, students under Fiona McNeill's guidance prepared the samples for elemental analysis through μXRF, and Fiona McNeill and Mic Farquharson and their students performed the μXRF scans at the Canadian Light Source. Fiona McNeill performed the PyMCA analysis to obtain Fe maps through the samples. I performed the task of modelling the system and the skin geometry by Monte Carlo simulations using the EGS5 code. The simulation results were evaluated with guidance from my supervisors.

Dr. Gosia Korbas and Dr. Ibi Bondici provided advice and assistance with our work on the BioXAS beamline. Guidance on Fe distribution, skin structure, and Fe overload diseases came from my committee members, Dr. Bruce Wainman and Dr. Michelle Zeller. I, as the primary author, crafted the initial draft of this manuscript, with all subsequent authors contributing feedback and editorial revisions for the research submission.

An original version of this article was submitted to Applied Radiation and Radioisotopes. However, 12 months post-submission, the reviews had not been completed by the journal and so we withdrew the submission. This article has now been rewritten and submitted for publication to Biomedical Physics and Engineering Express on January 28th, 2024.

Investigation of the Accuracy of a Portable ^{109}Cd XRF System for the Measurement of Fe in Skin

Sami Ullah Bangash[1], Fiona E McNeill[1], and Michael J Farquharson[2]

[1]Department of Physics and Astronomy, [2]School for Interdisciplinary Sciences, McMaster University, Hamilton, ON, L8S 4K1, Canada

E-mail: bangashs@mcmaster.ca

Key Words: Fe, XRF, ICP-MS, Synchrotron μXRF, Pig Skin, Minimum Detectable Limit

Abstract

We have previously reported the design of a portable ^{109}Cd XRF skin Fe measurement system with a low detection limit of 1.35 μg Fe g^{-1} of tissue, which delivers a skin surface dose of 1.1 mSv in Fe overload and Fe deficiency disease. The system has been found to be precise but must also provide accurate measurements of Fe levels in the skin.

This article describes testing of the system's accuracy. Ten pigskin samples were measured using both the PXRF system and ICP-MS analysis. The two techniques reported a non-significant mean difference of 2.5 ± 4.6 μg Fe g^{-1}.

However, the ICP-MS measurements reported a wider range of values than determined by XRF, with two individual samples having ICP-MS results that were significantly elevated ($p < 0.05$) compared to XRF. Synchrotron μXRF maps of Fe in pigskin, obtained at the BioXAS beam line of the Canadian Light Source, indicated small areas of high Fe levels in the skin, mainly in the dermis, attributed to small blood vessels. Monte Carlo models (using the EGS5 code) determined that if these Fe 'hot spots' were towards the back of the skin, they would be measured by the ICP-MS analysis but not by the XRF system,

potentially explaining the discrepancies between ICP-MS and XRF results in the two samples.

The synchrotron μXRF maps also showed higher Fe concentration at the skin surface than in deeper skin layers. Monte Carlo models verified that the XRF system was most sensitive to these skin layers. The results indicate that when there are significantly high levels of Fe on the skin surface, the XRF system may not accurately estimate the average skin Fe levels. However, if the front Fe layer is constant in thickness, then with correction factors, it could accurately estimate the Fe levels in the surface layers of the skin.

Introduction

Fe Overload and Skin Fe Storage

We have previously described the development of a PXRF system for the *in vivo* measurement of Fe in the skin [1]. The system was designed to measure the potentially elevated Fe levels in the skin of patients suffering from hemochromatosis or thalassemia [2]. The liver is the primary storage site and a target organ for excess Fe in the body, with excess Fe in the liver causing cirrhosis, hepatic fibrosis and carcinoma [3]. However, it is difficult to measure the liver. Studies have shown a strong correlation between skin Fe and liver Fe concentrations [2], [4], and so a measure of Fe levels in the skin by XRF is intended as a surrogate measurement for Fe overload in the liver (and potentially other organs).

The system is fully described in our previous work [1]. However, to summarise: the Ag X-rays from the electron capture decay of ^{109}Cd to ^{109}Ag are used as a fluorescing source. The source is combined with a silicon drift detector to detect the characteristic X-rays from Fe in the sample in an approximate 180° backscatter geometry as shown in Figure 3. The system was calibrated against water-based Fe phantoms, and achieved a phantom-based MDL of 1.35 μg Fe g^{-1} in a 30-minute (real-time) measurement delivering a dose of 1.1 mSv to the skin.

The precision of the system in phantom measurements is thus well known. However, before the system can be used for *in vivo* measurements, it is necessary to test whether XRF measurements of the Fe levels in the skin are accurate. In addition, we wanted to know

whether our phantoms can be considered a good calibration model for skin and whether the MDLs of an *in vitro* skin model differ from the MDL in phantoms. Our system is calibrated using homogenous water phantoms, but the structure of skin is more complicated. Skin consists of three main layers, the epidermis, dermis and hypodermis (Figure 1). The epidermis is the skin's outermost layer and is further divided into five layers. The stratum basale lies deep and close to the dermis; the stratum spinosum, the stratum granulosum, and stratum lucidum are present in thick skin like palms and soles, and the stratum corneum, which is the outermost layer of skin. The deep skin layer, the dermis, contains blood vessels and nerve endings [5]. The hypodermis is the inner most layer of skin and consists of mostly fat tissues [6].

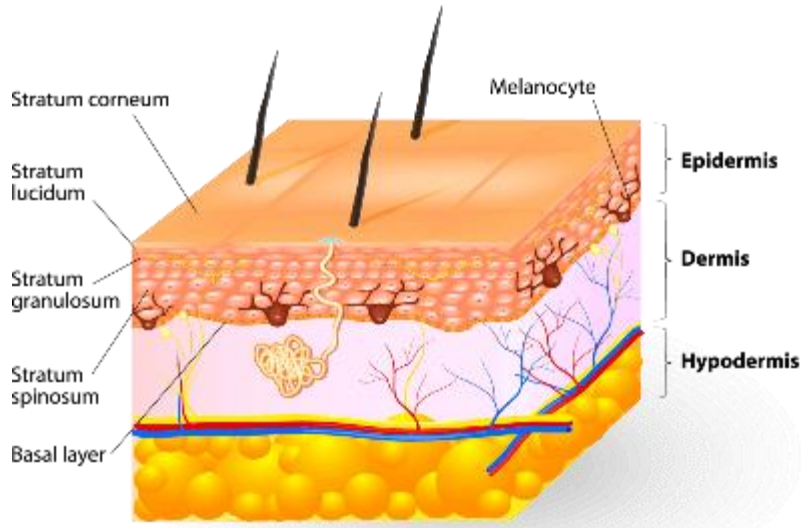

Figure 1: Illustration of different layers of human skin [7].

The depth distribution of Fe and the presence of blood vessels in the skin may complicate the measurement of Fe by XRF. The distribution of Fe is still not well known: one study of cadaver samples showed that the maximum Fe content was found in the deep layer of the epidermis, the stratum basale; a further study of Fe levels in patients with hemochromatosis indicated raised Fe levels in the stratum corneum and epidermis during different phases of the disease [8], [9].

The XRF system does not detect Fe in the different layers of skin equally well. The sensitivity of the system, i.e., the detected number of Fe counts per mg of Fe, falls with

increasing depth, and Fe at sites deeper than 0.5 – 1 mm is not detected. It is not known if the XRF measurement of Fe can be considered an accurate measurement of the 'bulk' sample in real skin. Hence, it is essential to test the XRF instrument's performance and accuracy prior to clinical applications.

This article describes work that is the first step in assessing whether the ^{109}Cd-based PXRF system can accurately measure Fe levels in skin, and whether homogenous water-based phantoms can be considered a good calibration model for XRF measurements of Fe in skin. We compare the measurement precision of phantoms and skin and describe validation studies performed to compare XRF analysis of pig skin Fe concentrations against the total Fe content of the same samples measured with ICP-MS. We provide new information on Fe distribution in pigskin assessed using synchrotron μXRF, and show, through the use of Monte Carlo models of varying skin Fe concentration, the factors which may impact the accuracy of the XRF measurement system.

Methods and Materials

Pigskin as a Model for Human Skin Measurement

Human skin is generally not very readily available and requires human research ethical approval prior to use. In addition, the Public Health Agency of Canada recommends that work with human samples be performed to biosafety level 2 standards. In the current study, Fe concentrations were therefore measured in ethically sourced pig skin due to the similarities of pig skin with human skin [10]. Pig skin is composed of an epidermis and dermis, similar to human skin, and the ratios of their epidermis thickness are comparable [11], [12]. Numerous studies have used pig skin as a substitute for human skin [10], [11], [13] and so the substitution of pigskin for human skin was considered acceptable for system validation.

As this work did not involve live animals, ethical approval from an animal research ethics board was not required for the study. Fresh skin of domestic pigs was sourced from a local butcher. This is considered ethical sourcing as the skin was marked for disposal. The

pigskin was thus food grade and this work did not require biosafety approval, although samples were disposed of into the biohazard waste stream after use.

PXRF and ICP-MS Comparison

Our *a priori* expectation of the comparison of Fe levels as measured by ICP-MS and XRF was that the two techniques would measure the same Fe concentrations if a) the two techniques measured the identical surface areas of the same samples and b) Fe in the pigskin could be considered to be relatively homogeneously distributed. The techniques might not match if the Fe had a strong spatial distribution with depth through the skin.

This assumption was made because the two techniques sample slightly different volumes. The working principle behind XRF analysis is the photoelectric effect. Ag photons from our ^{109}Cd radioactive source can create a vacancy in an Fe atom in the sample when an inner shell electron absorbs the photon energy and is emitted from the atom. The electronic transitions from the higher shells to the lower shells to fill the vacancies can result in X-rays being emitted, the energy of which is the difference in the energy of the transition shells involved. The X-rays are characteristic of and specific to Fe and are then measured with a suitable detector. The ^{109}Cd Ag X-rays that are used as the fluorescing source in this system are 22 and 25 keV, while the characteristic $K_{\alpha 1}$ X-rays from Fe are of energy 6.4 keV. These Ag and Fe X-rays are highly attenuated by soft tissue. The intensity of an Fe signal received at the detector from a sample in our XRF measurement is a strong function of depth. To a first approximation, the drop off in Fe signal with depth depends on the attenuation of the Ag X-rays as they enter the tissue multiplied by the attenuation of the Fe X-rays as they exit the tissue. There are additional geometric factors as the angle subtended by the detector from a point in the sample varies with depth. The XRF measurement, therefore, does not sample equally through the depth of the tissue. A higher proportion of the overall XRF signal comes from volumes near the surface of the skin sample than volumes further back.

XRF measurements were compared to analysis of Fe content of the same samples by inductively coupled plasma mass spectroscopy, because it is a relatively standard technique

for the elemental analysis of biological and environmental samples [14]. ICP-MS has many advantages for measuring elemental concentrations in a sample: high sensitivity and low detection limits for most elements down to parts per billion (ppb) levels [15]. The limitation of ICP-MS as a comparison to XRF is that it measures the average concentration of Fe over a bulk sample, as tissue samples are homogenized and digested in acid prior to measurement.

Pigskin Sample Preparation

The whole skin layer plus the underlying layer of subcutaneous fat, was cut and included in the measurement. The pigskin samples consisted of both the skin and the subcutaneous fat behind the skin and were approximately 5 mm deep, with the skin layer being approximately 2 mm thick. The volume of the phantom behind the skin was filled with paraffin wax before inserting the skin samples (Figure 2).

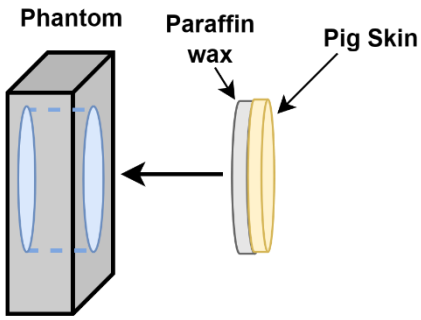

Figure 2: The phantom is filled with pig skin sample, with paraffin wax positioned behind the skin to replicate similar scattering properties to those of tissues.

Paraffin wax is composed of carbon and hydrogen and has X-ray scattering properties similar to human (and pig) soft tissue. Ten samples of fresh pigskin, each a 4 cm diameter circle cut to fit into the front phantom face, were cut and stored in the freezer prior to measurement. The ten samples were cut from two larger sheets of pigskin. It was not known if the two pigskin sheets came from one or two pigs.

Portable System Pigskin Experiment

The XRF system details have been fully described previously in other work, but we provide some information here to explain the pigskin measurements. A ^{109}Cd source was used to irradiate the 4 cm diameter skin samples that had been inserted into the front-face of the phantoms. The source is in a tantalum collimator, attached to one side of the detector onto a styrene window, as shown in Figure 3. The collimator ensures that the detector cannot see direct emissions from the source. The system is said to be in a 180° or backscatter geometry. The source activity at the time of measurement was 0.109 GBq.

Fe characteristic X-rays produce a signal in the detector and, after amplification, are processed by an Ortec Digital Gamma-Ray Spectrometer (DSPEC). The acquisition of the data is carried out with Gamma Vision software. The dead time during measurement was low, approximately 5 %. The samples were measured for a live time of 1800 s, and each measurement was repeated three times to get a better estimate of the uncertainty in a measurement.

The source is collimated and so only irradiates a small surface area of skin. To compare the XRF and ICP-MS samples, it was important to ensure both techniques measured the same skin sample areas. The skin samples were cut to 4 cm in diameter to fit in the phantom but were cut down further, to the beam sample area, before being sent for analysis by ICP-MS. The area irradiated by the ^{109}Cd source on the larger 4 cm diameter skin samples was estimated using chromatograph films. As the irradiation area at the sample surface is dependent on the distance between the sample and the source, the same geometry was used for beam size measurement and XRF measurements on the skin samples. A circular dark spot of 1 cm diameter appeared on the chromatograph film after exposure to the X- and γ-rays from ^{109}Cd and the darkened spot on the film permitted identification of the measurement area.

After the XRF measurements the circular surface area of 1 cm diameter that matched the measured irradiation area was cut from the skin samples, and the subcutaneous fat layer underneath the skin was removed, before sending the samples to the Analytical and

Environmental Services Laboratory of Kinectrics Canada to measure total Fe content by ICP-MS.

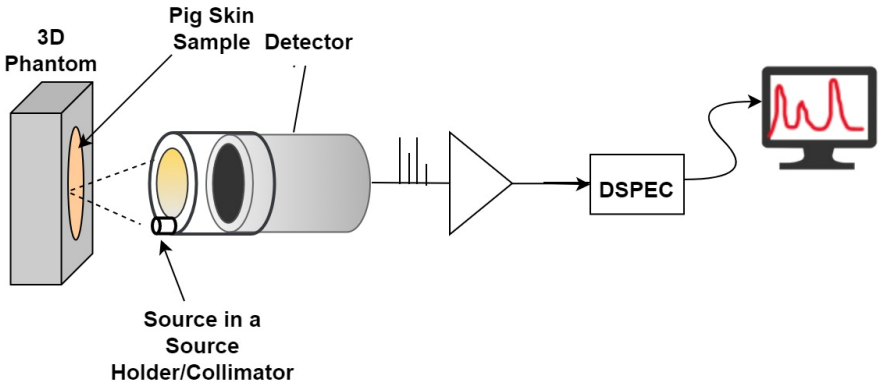

Figure 3: Experimental setup for measuring pig skin concentration. The skin sample is mounted at 0.5 cm from the source [1].

A typical spectrum resulting in the skin measurement is shown in Figure 4. The prominent peak from Ni K_α X-rays in the spectrum is due to the presence of Ni in the detector. This Ni peak is used to normalize the measurement system, which allows for a more robust XRF measurement. We have shown that the ratio of Fe X-ray signal to Ni X-ray signal does not change with distance from the detector [1].

µXRF Measurements of Fe Distribution in Skin

A µXRF image of Fe distribution in pigskin was made available from a separate ongoing study in our laboratory. That study is of percutaneous absorption of Pb in pigskin (CLS project number 37G12956). However, pigskin samples from the same source as previously described for PXRF and ICP-MS measurements, were measured as blank standards as part of that study. The samples were trimmed and had the subcutaneous layer of fat removed. They were not exposed to lead, instead samples had 100 µl of phosphate buffered saline placed on the skin surface and left to diffuse into the skin for 24 hours. After saline diffusion, the samples were freeze microtomed to 25 µm thick sections and placed onto 4 µm thick XRF film microscope slides. The sample was XRF scanned at 20 µm resolution

using the Bio-XAS beam line of the Canadian Light Source with an excitation energy of 13.45 keV. The Fe signals were extracted from each measurement pixel using the PyMCA code and a 2-dimensional map of the relative Fe level in the skin was obtained.

Monte Carlo Simulations

The effects of variations in Fe distribution that differed from the *a priori* assumption that Fe in pigskin was homogeneously distributed in pigskin were not known. Monte Carlo simulations of the system were performed to test the effects of Fe distribution on XRF measurement. The XRF system was simulated using the EGS5 Monte Carlo code. This is a well developed code frequently used for X-ray studies, that permits the coupled transport of electrons, positrons and photons within a given geometry. The simulation modelled the experimental system geometry illustrated in Figure 3. The model incorporated the detector geometry, comprised of the Si detector with an aluminum cap and a tantalum source collimator, as utilized for the XRF analysis of pig skin Fe. The X-ray excitation energies were set to those of the Ag X-rays (22.1 keV and 24.9 keV) and the 88 keV gamma rays from the source were also incorporated into the model.

The model performance was first tested against the experimental calibration of the PXRF instrument to assess the accuracy of the simulation. The experimental system uses a normalized calibration line of Fe K_α X-ray peak area to the Ni K_α X-ray peak area. Ideally, the experimental and modelled system comparisons would have been of this ratio. However, in this instance, the full details of the experimental system were not known. The detector manufacturer considers certain information proprietary, and the information is not disclosed. For example, the experimental system utilizes a Ni X-ray signal from the detector for normalization to compensate for both the variations in phantom-to-detector distance and the radioactive decay of the source. However, the exact location, mass etc. of the Ni in the system is uncertain. Attempts were made to simulate the presence of the Ni in the detector setup, but an exact match between experiment and model could not be obtained without the knowledge of the location, mass and distribution of the Ni. Instead, the simulated model was verified by showing that experiment and simulation Fe K_α counts

were correlated for a fixed geometry, and the simulation could thus be used to predict measurement system results.

The experimental calibration of the PXRF instrument was based on water-based phantoms and so water-based phantoms of volume 25 ml with varying Fe concentrations were simulated using the EGS5 code, and a calibration line was developed from simulated data. The validated Monte Carlo model was then used to simulate distributions of Fe that were indicated from synchrotron μ-XRF measurements of Fe in pigskin. These included simulations of hotspots created by blood vessels in the skin, and heterogeneous distributions of Fe across the skin layers.

ICP-MS and PXRF Measurement Results

Pigskin and Phantom Spectral Comparison

The XRF spectrum obtained from one of the pigskin samples is shown in Figure 4. A phantom spectrum is shown in the same chart for comparison. As can be seen, the phantom and the skin sample have approximately the same spectral shape and background. The average uncertainty in repeat measurements of a 10 ppm calibration phantom and the pig skin samples was found to be similar: 12.7 ± 0.6 μg Fe g^{-1} and 11.3 ± 1.8 μg Fe g^{-1}, respectively. Thus, the water-based phantom appears from spectral examination, and comparison of measurement reproducibility, to be a relatively good model for XRF measurements of skin. It also has the benefits of being low-cost and simple to create.

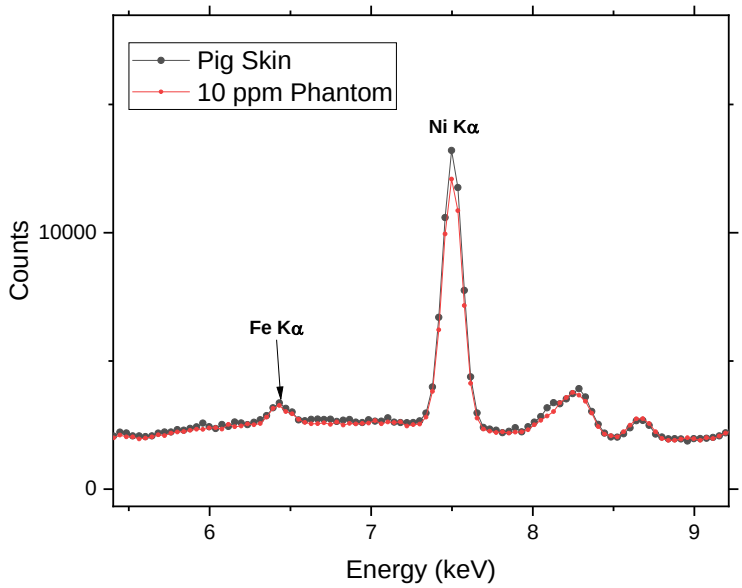

Figure 4: A comparison of a pigskin XRF spectrum and a 10 ppm water-based calibration phantom. The phantom and skin spectra display the similar spectral features and are of a similar intensity.

Our previous published work on this system found a detection limit in phantoms of 1.35 ± 0.35 μg Fe g^{-1} in a 30-minute (real-time) measurement. The phantom detection limit at the time of this work was found to be slightly higher, but not significantly so: 1.48 ± 0.99 μg Fe g^{-1}. A small increase was expected due to the decay of the radioactive source since the previous set of published data.

Comparison of Fe Analysis by XRF and ICP-MS

The comparison of the results from the PXRF system and the reported concentrations from ICP-MS measurements for the 10 pig skin samples is summarized in Table 1.

As can be seen in Table 1, XRF results are similar to ICP-MS results with the difference in estimate between the ICP-MS estimate and the XRF estimate being significant at the 95% confidence level in only two samples; S2 and S6 (shaded grey in the table). In addition, the differences between the individual sample estimate from XRF and ICP-MS vary from

-14.7% to 44.1% (-1.6 to 8.9 μg Fe g^{-1}), with the ICP-MS estimates being on average 13.4% (2.5 μg Fe g^{-1}) higher than the XRF estimates.

The Fe concentration distributions of the two data sets from XRF and ICP-MS are shown in Figure 5. Anderson-Darling normality tests were applied (using Minitab 21.4.2, Minitab USA) to the two distributions; XRF estimates and ICP-MS estimates. Given the limited number of samples, the test was set to reject the normality hypothesis if the p-value was less than 0.05.

It was found that both the ICP-MS (p = 0.068) and XRF data (p=0.892) could be considered normally distributed. Paired t-tests were applied to determine whether the mean of the ICP-MS and the mean of the XRF data are the same, i.e., whether on average, the two sets of skin Fe estimates are comparable. The results of the paired t-test are shown in Table 2.

Sample	XRF Mean Estimate	XRF Standard Error	ICP-MS Estimate	% Difference
S1	11.7	6	10.2	-14.7
S2	13	3	20.9	37.7
S3	14.2	5.1	12.6	-12.7
S4	9.3	5.3	10.4	10.6
S5	11.4	4.4	15.5	26.5
S6	11.3	4.7	20.2	44.1
S7	7.7	3.4	8.8	12.6
S8	10.8	4.3	10.2	-5.9
S9	10.1	5.1	13	22.3
S10	10.4	4.8	12	9.6

Table 1: Results in μg Fe g^{-1} of XRF and ICP-MS analysis of pig skin samples. XRF results are reported as the average of three measurements, and the XRF uncertainty is reported as the standard error of the mean. ICP-MS results were not reported with uncertainty but were quoted as having a detection limit of 1 μg Fe g^{-1}, from which it is inferred that each sample should be considered to have a measurement uncertainty of 0.3 – 0.5 μg Fe g^{-1}.

The paired t-test result found that a mean XRF estimate of the XRF measurements of 11.0 ± 1.8 μg Fe g^{-1} compared to a mean ICP-MS estimate of 13.5 ±4.2 μg Fe g^{-1} (p= 0.034, one-tailed test and p = 0.068, two tailed test). The one-tailed paired t-test is significant at the 5% level, which would suggest that the mean ICP-MS estimate of Fe in the pigskin samples is higher than the XRF estimate. However, there was no prior expectation that ICP-MS estimates would always be higher, so a one-tailed test is possibly unfair. The two-tailed t-test indicates that the two sample means are not different at the p = 0.05 level. In this small sample, the XRF can be considered, on average, to accurately assess Fe levels at a 95% confidence interval level in the skin as estimated by ICP-MS. However, while the one-tailed paired t-test is not fair given prior expectations, it may suggest a pattern to the data. As shown in Figure 5, the two samples that were measured as having a significantly different Fe content by ICP-MS compared to XRF are both much higher than the XRF result.

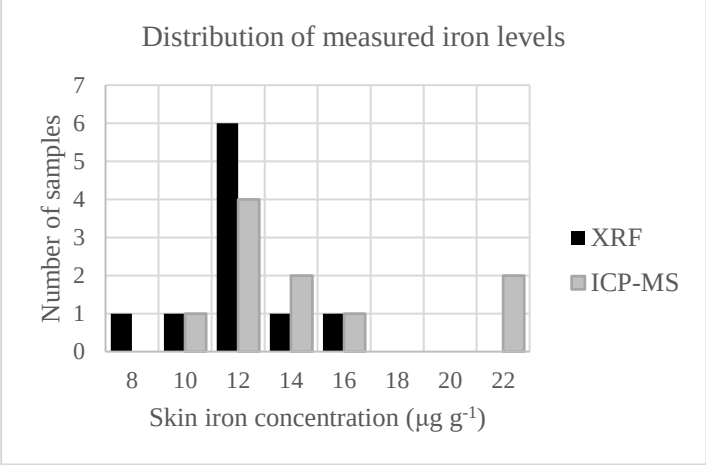

Figure 5: The distributions of skin Fe levels measured by XRF and ICP-MS

	XRF	ICP-MS
Distribution Mean (μg Fe g^{-1})	11.0	13.48
Variance	3.3	17.8
t Stat	-2.06	
P(T<=t) one-tail	0.035	
P(T<=t) two-tail	0.070	

Table 2: Paired t-test analysis for XRF and ICP-MS data

There was no evidence of a pattern to the data when a linear regression analysis was performed of the XRF estimates against the ICP-MS estimates, p = 0.14. However, when a linear regression was performed of the difference between the ICP-MS values and XRF values against the ICP-MS values, it was found to be highly significant, p= 0.0004. This regression is plotted in Figure 6. The graph shows that the difference between the XRF and ICP-MS values increases with increasing ICP-MS values. When the difference between the XRF estimate and the ICP-MS estimate was regressed against the XRF estimate, the relationship was found to not be significant, p = 0.83.

Overall, the data show that the ICP-MS estimates show more variation and a wider range of Fe concentration values, than the XRF estimates, and the difference between estimates is dependent on the ICP-MS measurements. This may suggest that there may be Fe in specific skin samples that is measured by ICP-MS but is not measured by XRF because of the decreasing sensitivity of the XRF measurement with depth.

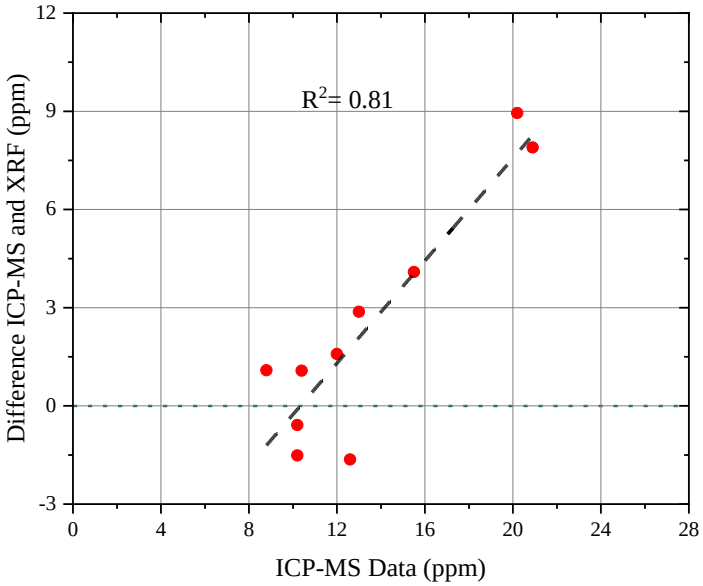

Figure 6: A plot of difference in concentration as assessed by ICP-MS and XRF versus ICP-MS

µXRF Maps of Fe in Skin

The possibility of areas of increased Fe towards the back of the sample is confirmed by the synchrotron µXRF image (Figure 7). It can be seen that there are Fe 'hot spots' at points in the sample that possibly relate to microvasculature in the skin. Figure 7 also suggests that Fe is not homogenously distributed but more concentrated at the skin surface. The synchrotron µXRF data suggests a layer of higher Fe level of approximate thickness 100 µm at the surface of the skin.

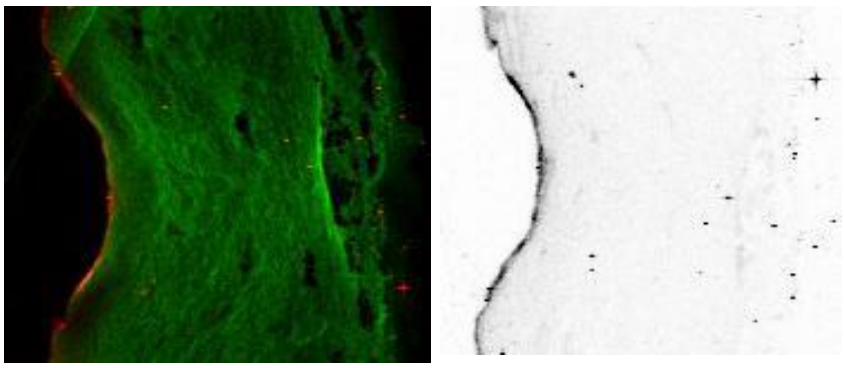

(a) (b)

Figure 7. The distribution of Fe in pigskin as assessed by synchrotron μXRF. These are two images of the same sample measurement. The skin surface, the stratum corneum, is on the left in each image. The resolution of both these images is 20 μm per pixel. The colour image (a) shows the distribution of Fe in red, and to outline the skin, the distribution of chlorine in green. The black and white image (b) is of the Fe distribution only.

Simulation Results

The initial Monte Carlo simulations modelled measurement of homogeneously distributed water-based Fe doped phantoms. The simulated Fe K_α X-ray signals for specific concentrations were strongly correlated with the experimental Fe K_α X-ray signals, $p < 0.0001$ and $R^2 = 0.946$. The slope of the regression was 1.13 ±0.12, so the peak area per unit concentrations were found to be the same to with uncertainties. The experimentally measured Fe concentration in non-homogeneous phantoms should be predictable from the simulation as long as the experimental geometry remains fixed.

Using the verified EGS5 model, simulations were performed to investigate whether remnants of blood vessels (presumed to be the source of Fe 'hot spots') at various skin depths could produce the results that would explain observed differences in the pigskin Fe levels measured by XRF and ICP-MS. The presence of small blood vessels were modelled using a circular cylinder of thickness of 0.2 cm and diameter 2 cm with a total mass of 0.6284 g to represent the skin. Pig skin samples were previously found, on average, to contain approximately 11 ppm of Fe, and so the concentration of Fe in the cylinder was set

to this value. In comparison, whole blood has an average Fe content of 50.3 mg Fe dl^{-1} which approximately equivalent to 500 ppm [16]. Small spheres of diameter 0.29 cm filled with tissue with Fe concentrations of 500 ppm were therefore modelled at various points through the skin to determine the locations where hot spots would be measurable in a PXRF measurement. Hot spots would of course be measured in all locations in a hypothetical ICP-MS measurement of the same sample.

Figure 8 illustrates a 2D contour plot showing the impact of an Fe hot spot at various positions within the skin. The x-axis denotes the depth into the skin, while the y-axis represents the length of circular face of the skin. Changes in the measured Fe level are shown on a colour scale. Blue indicates no change in measured signal, while red indicates a large change in measured signal. It can be seen that XRF will likely not detect residual blood vessels beyond a skin depth of 0.5 mm. In addition, there are locations off-axis from the source where blood vessels closer to the surface than 0.5 mm remain undetected. The maximum effect of the presence of small blood vessels on the PXRF measurement is when the vessels are near the skin surface. These data therefore align with the hypothesis that dependant on location, small fragments of blood vessels, e.g., not removed with the fat at the back of the skin or small vessels within the skin, would be detectable by ICP-MS but not by XRF.

In addition to hot spots, the synchrotron images suggest a high Fe layer at the skin surface. A Monte Carlo simulation was performed to model the effect of a 100 μm thick high Fe layer at the front of the skin. The skin behind this layer was modelled by a lower Fe concentration. The goal of this simulation was to investigate the impact of an inhomogeneous distribution of Fe within the skin on the XRF signal, and the accuracy of measurement if this XRF signal was used to estimate skin Fe level using homogenous phantoms. Various Fe concentrations in the front layer were simulated, while keeping the concentration in the back layer constant at 11 ppm.

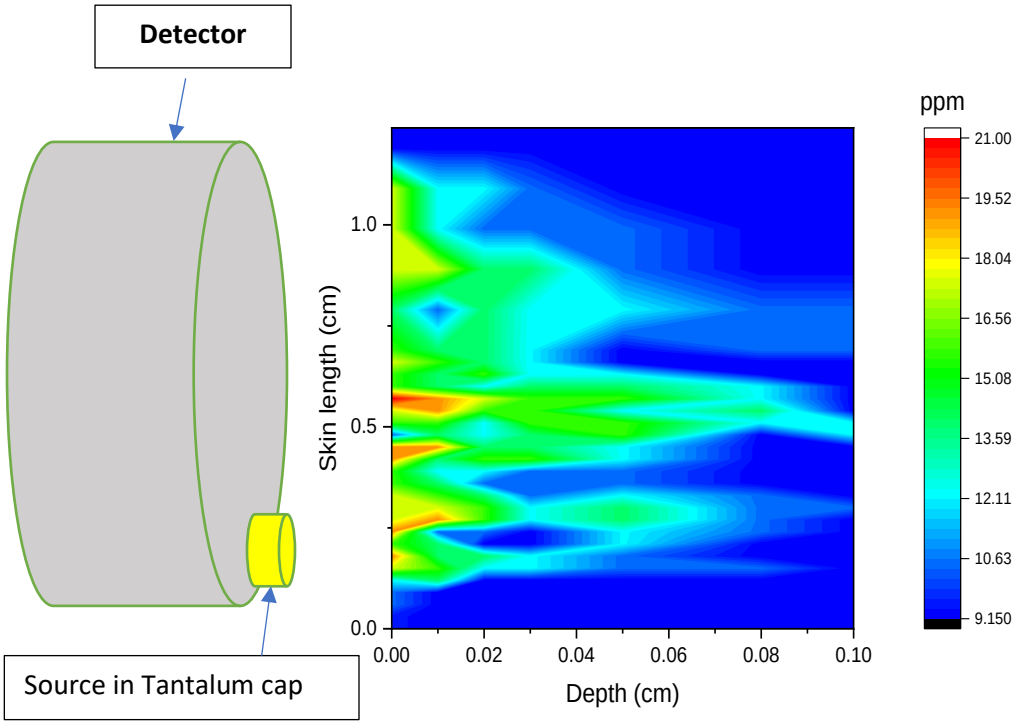

Figure 8: 2D contour plot representing the effect of Fe hot spots on an XRF measurement at various locations in the skin.

Table 3 provides a comparison between the average Fe concentration that would be hypothetically measured by ICP-MS and the XRF estimated Fe concentration using homogeneous phantoms for calibration.

The results presented in Table 3 demonstrate that the XRF primarily detects the Fe in the front layer. This observation highlights the higher sensitivity of the PXRF system towards the front layer in comparison to ICP-MS, which quantifies the average Fe concentration across the entire skin sample.

Front Layer Fe content (ppm)	Average Fe content (ppm)	Simulated XRF estimate of Fe content (ppm)
12.8	12.2	11.9
16.3	13.4	14.3
20.0	14.0	16.9
42.8	19.7	36.7
51.5	21.9	45.5
55.9	23.0	52.2
61.5	24.4	57.9
72.2	27.0	67.3
79.7	34.6	74.0
203.5	75.8	184.3

Table 3: Results of the simulation comparing surface layer Fe concentration, average Fe concentration and XRF estimate of Fe concentration The high Fe layer at the skin surface is assumed to be 100 µm thick and the back layer is assumed to have a concentration of 11 ppm. At low surface Fe concentrations, the XRF and ICP-MS are predicted to produce estimates that are the same to within experimental measurement uncertainties.

Figure 9 shows the Fe concentration of front layer plotted against the XRF estimate of Fe concentration as calculated from the simulation.

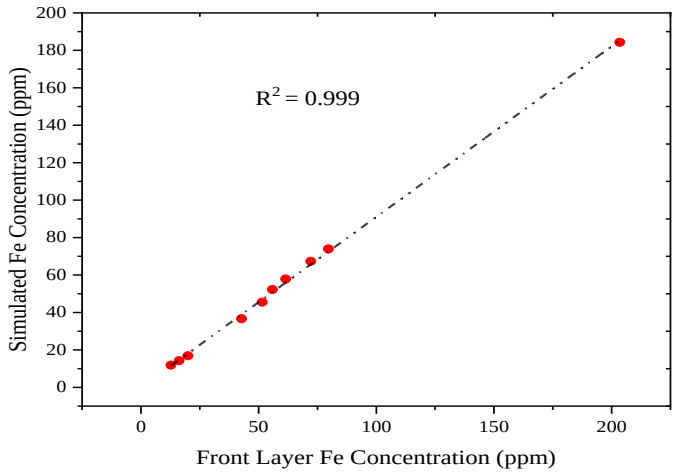

Figure 9: The observed correlation between the Fe concentration estimated by XRF and the front Fe layer concentration as simulated using the Monte Carlo code EGS5.

Discussion

XRF measurements in pigskin samples sample a thinner layer of the skin than ICP-MS measurements. The PXRF system probes approximately the first 0.5 mm of skin, while the ICP-MS analysis measures the whole 2 mm depth. Despite this difference, XRF and ICP-MS analyses of Fe levels in skin were found to be the same on average to within 95% confidence levels in 10 pigskin samples. However, in two individual samples, the ICP-MS estimates of Fe content were significantly higher than the XRF estimate, and over the 10 samples the ICP-MS measurements identified a wider variation in Fe content in the skin samples than XRF measurements. Synchrotron μXRF measurements of Fe distribution in skin and Monte Carlo simulations support the hypothesis that the higher Fe content measured by ICP-MS is likely due to Fe deposits (possibly from blood vessels) deeper in the skin. These 'hot spots' would not be measured by XRF, but would be measurable by ICP-MS.

In this study, skin samples were cut down from the skin surface to the bottom of the dermis, and there may have been small amounts of subcutaneous tissue, containing vascular and capillary tissue, left on the back of the sample. The ICP-MS measurements may therefore not be estimates of Fe content in skin only. However, μXRF measurements of Fe distribution in skin do suggest the possibility of small blood vessels within the epidermis and dermis. These would be measured by ICP-MS at all depths, but only by XRF if they are located near the surface of the skin.

The synchrotron μXRF map of Fe distribution in pig skin suggests not only that there are hot spots in skin, but that there is a layer of higher Fe concentration at the surface of skin. This result is different than observed in prior studies of human cadaver data, where the highest Fe concentrations were at the epidermal/dermal boundary. However, in another biopsy sampling studies of people suffering from hemochromatosis, a similar pattern of elevated Fe in the stratum corneum and outer layers of skin was observed in certain stages of the disease [8], [9].

The observation of a high Fe surface layer in μXRF measurements led to Monte Carlo of this Fe distribution. The Monte Carlo models predicted a strong correlation between Fe concentration in the front layer of the skin and the estimated Fe concentration measured by the PXRF system, $R^2 = 0.99$ and $p < 0.0001$. The slope of the relationship is 0.91 ± 0.01. The relationship is not 1:1 which suggests that while the XRF estimate is dominated by the signal from the front Fe layer, there is a contribution to the XRF estimate from the lower concentration tissues further back in the skin. The XRF estimate is therefore not accurate at solely determining the Fe content of the front layer, nor is it completely accurate compared to ICP-MS in estimating the average Fe content over a 2 mm depth of skin. However, if the Fe layer is of a relatively constant thickness in all skin samples, then this relationship suggests that applying a correction factor to the XRF estimate could result in an accurate estimate of the level of Fe in the surface layer. If correction factors are possible, then the current homogeneous water-based calibration phantoms could be used. This would make phantom construction simple as they are readily manufactured, reproducible and straightforward to measure. They can be made quickly and are low-cost.

The application of a correction factor depends on verification of this distribution of Fe in skin. The evidence is however scant. Further studies of Fe distribution in skin are required, especially under conditions of Fe overload disease, to verify Fe distribution in order to fully assess the accuracy of this PXRF system *in vivo*.

However, the Monte Carlo model of a high Fe surface skin layer predicts that at low Fe levels estimates by ICP-MS and XRF would be the same to within measurement uncertainties. This prediction matches the experimental data where 80% of samples had XRF and ICP-MS estimates that were within uncertainties of each other. However, if the Fe level increases substantially in the front layer, then at high Fe levels, the ICP-MS and XRF estimates are expected to diverge. Under these conditions, the estimate from the PXRF system is expected to be higher than the ICP-MS estimate and would be a better estimate of the Fe level in the surface layer, rather than an estimate of the average Fe level in a sample.

However, further studies must be conducted of Fe distributions in skin to verify raised skin surface levels. If this Fe distribution is validated, there are yet further studies must be performed with this system. While previous studies have determined that increases in Fe level in skin can be observed under conditions of Fe overload, this PXRF system has never been tested under those conditions. Studies must be performed using this XRF system on skin from Fe overload studies to determine the system's ability to distinguish between 'normal' and overloaded groups or individuals.

Conclusion

The accuracy of a hand-held XRF measurement was tested using XRF measurements of healthy pigskin, which were analyzed by ICP-MS. The system performed well, with the mean difference between XRF and ICP-MS being 2.5 ± 4.6 μg Fe g^{-1}. Two individual samples had ICP-MS estimates that were significantly higher than XRF estimates. Synchrotron μXRF maps of Fe in skin and Monte Carlo models are consistent with a hypothesis that small blood vessels towards the back of the skin can be observed by ICP-MS but not PXRF. Furthermore, μXRF mapping suggests that Fe may be increased in a narrow layer at the surface of the skin. Monte Carlo models predict that if Fe is higher at the skin surface then the PXRF estimate will reflect the raised Fe levels at the surface and may be a clinically useful measurement. However, further studies of Fe distribution in skin are required to verify this distribution of Fe.

Acknowledgements

The Government of Canada's NSERC Discovery program and the Higher Education Commission Pakistan provided funding for this research.

μXRF measurements were performed at the Bio-XAS beam line of the Canadian Light Source. The authors are very grateful to Dr. Gosia Korbas and Dr. Ibi Bondici for their advice and help with our work on this beamline.

The authors thank Dr. Bruce Wainman of the Department of Pathology and Molecular Medicine, McMaster University and Dr. Michelle Zeller of the Division of Hematology & Thromboembolism, Department of Medicine, McMaster University, for their ongoing support of this project. Their advice on Fe distribution, skin structure, Fe overload disease and the implementation of devices in clinical environments has been invaluable in the development of this device.

References

[1] S. U. K. Bangash, F. E. McNeill, M. J. Farquharson, and D. R. Chettle, "Feasibility of a 109Cd-based portable XRF device for measuring skin iron concentration in anaemic and β−Thalassaemic patients," *Biomed. Phys. Eng. Express*, vol. 8, no. 6, p. 065034, Nov. 2022, doi: 10.1088/2057-1976/AC9E02.

[2] M. J. Farquharson, A. P. Bagshaw, J. B. Porter, and R. D. Abeysinghe, "The use of skin Fe levels as a surrogate marker for organ Felevels, to monitor treatment in cases of iron overload," *Phys. Med. Biol.*, vol. 45, no. 5, p. 1387, May 2000, doi: 10.1088/0031-9155/45/5/320.

[3] J. C. Barton, "Handbook of iron overload disorders," p. 376, 2010, Accessed: Oct. 24, 2022. [Online]. Available: https://books.google.com/books/about/Handbook_of_Iron_Overload_Disorders.html?id=BUVBcNkAdrwC.

[4] I. Youssry *et al.*, "Skin Iron Concentration: a Simple, Highly Sensitive Method for Iron Stores Evaluation in Thalassemia Patients," *http://dx.doi.org/10.1080/03630260701503833*, vol. 31, no. 3, pp. 357–365, Jul. 2009, doi: 10.1080/03630260701503833.

[5] S. Agarwal and K. Krishnamurthy, "Histology, Skin," *StatPearls*, Feb. 2019, Accessed: Oct. 26, 2022. [Online]. Available: http://europepmc.org/books/NBK537325.

[6] C. Stecco, W. Hammer, A. Vleeming, and R. De Caro, "Subcutaneous Tissue and Superficial Fascia," *Funct. Atlas Hum. Fascial Syst.*, pp. 21–49, 2015, doi: 10.1016/B978-0-7020-4430-4.00002-6.

[7] Disabled World, "Human Skin Conditions and Diseases," *Disabl. World.*, p. 1, 2020, Accessed: Mar. 04, 2024. [Online]. Available: https://www.disabled-world.com/health/dermatology/skin/.

[8] E. D. Desouza *et al.*, "Characterization of the depth distribution of Ca, Fe and Zn in skin samples, using synchrotron micro-x-ray fluorescence (SμXRF) to help quantify in-vivo measurements of elements in the skin," *Appl. Radiat. Isot.*, vol. 77, pp. 68–75, Jul. 2013, doi: 10.1016/J.APRADISO.2013.02.019.

[9] I. Guinote *et al.*, "Using skin to assess iron accumulation in human metabolic disorders," *Nucl. Instruments Methods Phys. Res. Sect. B Beam Interact. with Mater. Atoms*, vol. 249, no. 1–2, pp. 697–701, Aug. 2006, doi: 10.1016/J.NIMB.2006.03.120.

[10] A. Summerfield, F. Meurens, and M. E. Ricklin, "The immunology of the porcine skin and its value as a model for human skin," *Mol. Immunol.*, vol. 66, no. 1, pp. 14–21, Jul. 2015, doi: 10.1016/j.molimm.2014.10.023.

[11] F. Meurens, A. Summerfield, H. Nauwynck, L. Saif, and V. Gerdts, "The pig: a model for human infectious diseases," *Trends Microbiol.*, vol. 20, no. 1, pp. 50–57, Jan. 2012, doi: 10.1016/J.TIM.2011.11.002.

[12] Y. Liu *et al.*, "Light Microscopic, Electron Microscopic, and Immunohistochemical Comparison of Bama Minipig (Sus scrofa domestica) and Human Skin," *Radiology*, vol. 27, no. 6, pp. 651–655, Dec. 1936, doi: 10.1148/27.6.651.

[13] A. M. Barbero and H. F. Frasch, "Pig and guinea pig skin as surrogates for human in vitro penetration studies: A quantitative review," *Toxicol. Vitr.*, vol. 23, no. 1, pp. 1–13, Feb. 2009, doi: 10.1016/J.TIV.2008.10.008.

[14] K. L. Nuttall, I. H. Gordon, K. Ow, and E. N. Ash, "Inductively Coupled Plasma Mass Spectrometry for Trace Elem ent Analysis in the Clinical Laboratory*," 1995.

[15] "Elemental analysis by ICP-MS, icp-ms for metal analysis, icp-ms vs icp-qqq | Agilent." https://www.agilent.com/en/product/atomic-spectroscopy/elemental-analysis-by-icp-ms (accessed Nov. 01, 2022).

[16] A. Sachs, V. E. Levine, F. C. Hill, and R. Hughes, "COPPER AND IRON IN HUMAN BLOOD," *Arch. Intern. Med.*, vol. 71, no. 4, pp. 489–501, Apr. 1943, doi: 10.1001/ARCHINTE.1943.00210040048006.

Chapter 4

Paper III: Performance testing a portable ^{109}Cd XRF system for the measurement of *ex vivo* skin Fe content in a rat Fe overload model

Sami Ullah Bangash[1], Fiona E McNeill[1], and Michael J Farquharson[2]

[1]Department of Physics and Astronomy, [2]School for Interdisciplinary Sciences, McMaster University, Hamilton, ON, L8S 4K1, Canada

4.1 Introduction to Paper III

In Paper II, we demonstrated the potential of a PXRF system to accurately measure skin Fe levels. However, the skin samples utilized were sourced from healthy pigs and were not samples from Fe overloaded animals. Rat skin samples from an earlier study conducted by Dao *et al.* were made available and employed to assess the performance of the system in measurements of the skin of animals in Fe overloaded conditions. The rats underwent Fe overload via peritoneal Fe dextran injections, with varying levels of injected Fe ranging from 0 mg Fe^{+2} to 160 mg Fe^{+2}.

In her study, Dao measured the skin samples of the rats using a laboratory-based XRF system. The measurement results were shared with us. For the measurements in this thesis, we used new skin samples from the same rats for measurements using the PXRF system. Each sample underwent a single measurement in both studies, but there was a difference in the duration of the measurements. The laboratory XRF measured the samples for a live time of 3600 seconds per sample, while each sample was measured for a live time of 1800 seconds with the PXRF system.

Our findings suggest that PXRF not only effectively differentiated between various Fe level dose groups but also demonstrated a robust linear correlation of measured Fe level with rat Fe doses. Additionally, the PXRF measurements exhibited a strong correlation with the laboratory XRF results. This correlation is considered noteworthy as the previous study conducted by Dao *et al*. revealed a strong correlation between skin Fe concentration and liver Fe concentration using laboratory XRF. The liver is the primary storage site for Fe overload, and the strong correlation between the PXRF and laboratory XRF measurements indicates the potential of the PXRF system's measurements of skin being a surrogate measure of liver Fe level and thus suitable for diagnosing Fe overload conditions. This could make for a suitable clinical measurement. Nevertheless, while the system shows potential, there will be several layers of further study, e.g. a clinical trial for safety, followed by a small trial of *in vivo* measurements on human skin and finally, a large-scale clinical trial before implementing the system in clinical settings.

I, as the first-named author, prepared the rat skin samples for PXRF measurement, and I conducted the measurement and analysis of these samples under the supervision of my advisors. Additionally, I authored the initial draft of this paper, incorporating feedback and editorial comments from my supervisors before finalizing it for research submission.

The paper is ready for submission.

Performance testing a portable ^{109}Cd XRF system for the measurement of *ex vivo* skin Fe content in a rat Fe overload model

Sami Ullah Bangash[1], Fiona E McNeill[1], and Michael J Farquharson[2]

[1]Department of Physics and Astronomy, [2]School for Interdisciplinary Sciences, McMaster University, Hamilton, ON, L8S 4K1, Canada

E-mail: bangashs@mcmaster.ca

Abstract

A ^{109}Cd-based portable X-ray fluorescence (PXRF) system has been designed to measure skin Fe concentration in thalassemia and hemochromatosis patients. The system's performance was tested via measurements of the skin of rats dosed (via intraperitoneal injection) with varying levels of Fe. T-tests between mean group Fe levels determined that the system was able to distinguish between groups of normal rats and rats dosed with 80 mg Fe^{2+} and between rats dosed with 80 mg Fe^{2+} and 160 mg Fe^{2+} ($p = 0.001$ and $p=0.002$ respectively.) In addition, linear regressions determined that there was a strong correlation, $R^2= 0.84$, $p < 0.0001$, between PXRF rat skin measurements and rat Fe dose.

The portable system measurements were found to be linearly correlated ($R^2 = 0.85$, $p <0.0001$) with measurements of a laboratory based XRF system. As the laboratory system skin Fe levels had previously been shown to correlate with liver Fe levels in individual animals, this suggests the PXRF skin measurements can act as predictors for elevated Fe levels in organs at risk.

The demonstrated ability of the PXRF system to distinguish between groups of rats and to determine the dosage level of an individual rat in these *ex vivo* measurements suggests the system has the potential to be used in clinical measurements. Further work should be done to study the system performance *in vivo*.

Introduction

Fe is an essential element that regulates many physiological functions in the body. The Fe level in the body must be kept within prescribed limits, as Fe toxicity can cause critical organ failure. Peak serum levels of Fe of less than 350 μg dl^{-1} are considered minimally toxic, while levels greater than 500 μg dl^{-1} are classed as severe toxicity [1]. The two diseases, β-thalassemia and hemochromatosis, require the monitoring of Fe levels in patients. β-thalassemia, a genetic disease in which the formation of hemoglobin protein is reduced, is managed clinically through blood transfusion. However, in individuals undergoing multiple blood transfusions, this can lead to Fe accumulation in and damage to vital organs such as the liver, heart, and pancreas. Hemochromatosis is also a genetic disorder in which the body absorbs too much Fe from the intestine, accumulating excess Fe in critical organs [2]. Accurate monitoring of Fe levels is essential in both these groups of patients. There are currently limitations of the available clinical methods for the assessment of Fe overload [3] and new technologies that permit point-of-care assessment of Fe levels *in vivo* would be useful for treatment providers.

Epidermis in Human and Rat Skin

The epidermis, the outer layer of skin, is subdivided into four distinct sublayers: the basal layer (deepest), spinous layer, granular layer, and stratum corneum (surface) [4]. The stratum corneum is a thin layer of cells that have ceased their metabolic activities. In both human and rat skin, the keratinocytes within this layer have lost their nuclei and organelles. These cells, called keratinocytes, are filled with a protein called keratin and contain lipids. The primary function of this layer in both skins is to prevent excessive water loss and to act as a protective barrier[5]. In rats and humans, keratinocytes in the basal layer proliferate and migrate toward the skin's uppermost surface and both rat and human basal layers contain melanocytes (responsible for pigmentation and protection against UV sunlight) and Merkel cells (accountable for touch or sensation) [6].

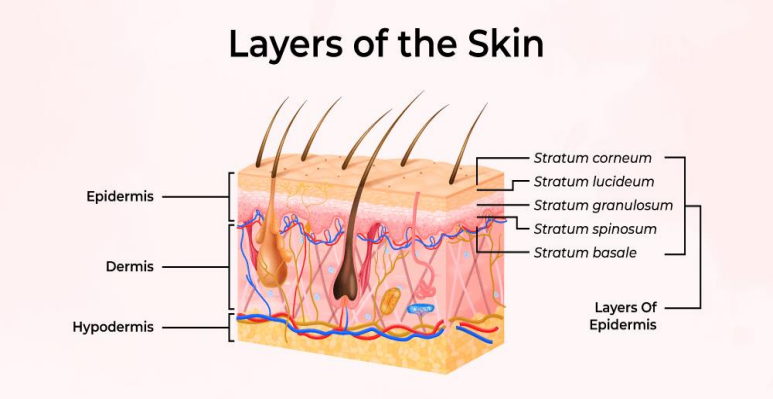

Figure 1: An Illustration of Human Skin Structure: Depicting Distinct Layers of the Skin [7].

Skin Fe as Surrogate for Liver Fe Concentration

Studies have shown that skin Fe concentration could correlate to liver Fe concentration [8], [9] and a technology that can accurately identify whether Fe levels in the skin are 'elevated' could be predictive of risk to critical organs. Measurement of Fe in the skin using a portable ^{109}Cd based XRF system has shown potential [3], and the study reported here was designed to test the performance of the PXRF system in assaying the Fe skin levels of rats dosed with varying levels of Fe. The portable system was used to measure the Fe levels of *ex vivo* rat skin samples obtained from a prior study and tested to see if it could be intercalibrated with a laboratory XRF system. Rat skin sample measurements would allow the predictive capabilities of the system to be tested, while intercalibration aimed to show whether the PXRF results could be predictive of levels in organs at risk. The goal was to determine whether the system was able to distinguish between the skin Fe levels of groups of rats dosed with varying levels of Fe or possibly whether the system was able to distinguish between the Fe levels of individual animals.

Materials and Methods

Rat Skin as Model to Human Skin

Rats are used to study human diseases due to their genetic similarity to humans, and skin permeability measurements and drug efficacy tests are modelled using rats because of their presumed similarity [10]. The choice of an animal as a model in a pre-clinical study depends on how easily they can be handled, their cost and availability. Since rats are inexpensive, readily available, and have skin similarities to humans, they have been used as a model to study Fe overload conditions. Humans and rats both have three layers of skin, but, rat skin is more loosely attached compared to human skin [10]. This is however a result of the structure of the hypodermis, not the epidermis or dermis. The epidermal thickness in rat skin ranges from approximately 15 to 170 μm with the thickest skin being found during adolescence [11]. The average epidermal thickness in human skin is approximately 100 μm, with a range of 50 μm to 1 mm [12]. However, human epidermal thickness varies strongly with location with the thickest skin in the human body being found on the plantar aspect of the foot (average thickness 600 μm) with the thinnest being found in the pubic and genital areas of the body (average thicknesses 31 and 45 μm) [13] .However, neither of these epidermal thickness extremes are likely sites for a point-of-care *in vivo* measurement. The more likely sites of the volar or dorsal forearm, wrist or dorsum of the hand, have average thicknesses from 75 to 94 μm. There is therefore some overlap in the thickness of the human epidermis that would be measured *in vivo* and the epidermis thickness in rats.

The penetration of 6.4 keV Fe X-rays within skin is limited, and our previous work has shown that Fe of depth greater than 0.5 mm does not contribute significantly to the signal. If elevated Fe levels are located within the epidermis, then the majority of Fe content in the skin of both rats and humans should be measurable by the PXRF system. Consequently, the rationale behind this study is that the disparity in skin thickness between human and rat skin is unlikely to significantly impact XRF measurements, making rat skin a viable model for studying the potential performance of the portable ^{109}Cd XRF system for measurements of Fe overload in human skin.

Sample Preparation

The skin samples used in this study were obtained from rats that were loaded with Fe in two experiments in a prior published study [14] which aimed to determine whether Fe loading resulted in elevated levels of Fe in skin. Groups of male Wistar rats, purchased from Charles River Laboratories, were injected intraperitoneally with Fe dextran over a period of three weeks followed by an eight day pause to allow Fe levels to reach equilibrium. A control group of rats were injected intraperitoneally with deionized water. The rats were fed a standard rodent diet and permitted to freely drink deionized water.

The groups of rats, the total administered Fe doses, the dosing regime, and the number of skin samples obtained from each group are shown in Table 1.

Group	Total Administered Fe Dose	Dosing regime (injections per week)	Number of skin samples
A	0 mg Fe^{+2}	1 x 0.8 ml	8
B	80 mg Fe+2	1 x 0.8 ml	6
C	160 mg Fe^{+2}	1 x 1.6 ml	5
D	160 mg Fe^{+2}	2 x 0.8 ml	4
E	60 mg Fe^{+2}	3 x 0.2 ml	2
F	75 mg Fe^{+2}	3 x 0.25 ml	1
I	120 mg Fe^{+2}	3 x 0.4 ml	2

Table 1: The total dose in mg Fe^{+2}, the dosing regime and the number of measured skin samples

After sacrifice, skin samples were cut from the animals and stored in an ultra-low temperature freezer. Samples were released to the authors of this work, and the skin hairs were then removed, and the skin was cut into a 4 cm diameter circle to fit in a phantom holder used in the PXRF calibration procedure [2]. The rat skin was approximately 2 mm thick and included a little of the underlying fat layer. The skin was fitted into the phantom with a paraffin wax base underneath the skin to simulate the scattering properties expected from the tissue below the skin. Twenty eight skin samples were prepared from twenty eight

different animals, ranging from 0 mg Fe dose (normal Fe levels) to 160 mg Fe dose (Fe overload).

Experiment

Measurement with the ^{109}Cd PXRF system

The rat skin samples were measured with the portable PXRF system, which utilizes a silicon drift detector (SDD) and ^{109}Cd as the excitation source. Characteristic Fe X-rays are produced when skin samples are irradiated with the Ag X-rays from the source and the detector measures the Fe K_α X-rays. The source was collimated in a source holder and consequently irradiated a 1 cm diameter circle of the sample [25]. Each sample was measured for a real time measurement of 1800 seconds. The signals were amplified and analyzed by an Ortec Digital Gamma Ray Spectrometer (DSPEC with Gamma Vision software. The Fe X-ray peak areas were extracted from the XRF spectrum using Origin Pro software. A mathematical model was fitted to the spectrum, with Gaussian functions being used to model the X-ray peaks. Figure 2 shows the experimental arrangement for rat skin Fe measurements.

Measurement with the laboratory XRF system

The skin samples were also measured with a laboratory-based XRF system that had been described in the initial rat Fe loading study [14], to allow for a point of comparison between the results of the PXRF system and the rat loading study. That study was able to show that there was a relationship between skin Fe level and liver Fe level. If the PXRF system measurements of skin correlated with the laboratory skin measurements, then the portable skin Fe measurements should correlate with liver Fe level. The laboratory XRF system is also equipped with a silicon drift detector, but in the laboratory system the fluorescing source is an X-ray tube. The X-ray tube has a molybdenum target microfocus tube that produces a monochromated beam of energy 17.5 keV which is focused to obtain a beam of 2 mm-by-2 mm incident on the sample. The samples were placed in a sample holder and covered with 4 μm thick Ultraline X-ray film on both sides. The detector was mounted at

an angle of 90 degrees to the incident beam. Each sample was measured for a live time of 1 hour.

Normalization to Ni

There was a prominent Ni peak in the spectra obtained from both the ^{109}Cd PXRF and laboratory XRF systems due to the presence of Ni in the SDD detectors. The area of the Fe K_α peak and the area of the Ni K_α peak are both extracted from the spectrum in each system. The Fe K_α peak was normalized to the Ni K_α peak, as we have shown in previous work [15] that this reduces the effect of phantom distance on the results in the portable ^{109}Cd XRF system. In addition to the Ni peak, the laboratory XRF system also features a prominent argon peak. The study [14] utilized the argon peak for normalization purposes and measured each sample once. Consequently, to enhance comparability, the measurement of each sample using PXRF was not repeated.

Results

Spectral features in rat skin and phantoms

The PXRF system spectra obtained from a rat skin sample (estimated concentration 10 μg g^{-1}) and a 10 μg g^{-1} calibration phantom, both measured for 1800 seconds, are compared in Figure 3. The spectra are similar, but the background under the Fe and Ni K_α X-rays in the 10 μg g^{-1} phantom spectrum is higher than the background under the Fe and Ni K_α X-rays in the rat skin sample. The ratio of the backgrounds is a factor of 1.4. However, while the background appears larger in the phantom spectra, the uncertainties in the measurements of the rat skin sample (not dosed with Fe) and a 10 μg g^{-1} water-based phantom are not significantly different. The average measurement uncertainty of rat skin samples was 11 ± 2.8 μg Fe g^{-1}, while the average measurement uncertainty of phantoms was 10.0 ± 1.8 μg Fe g^{-1}. In general, while the background may be larger, the spectral shape and measurement uncertainty suggest that the water-based phantoms are good representation of rat skin Fe measurement spectra. A limitation of the phantoms may be that they are water-based phantoms with homogeneously distributed Fe content, which may not be an accurate model of the Fe distribution in the rat skin.

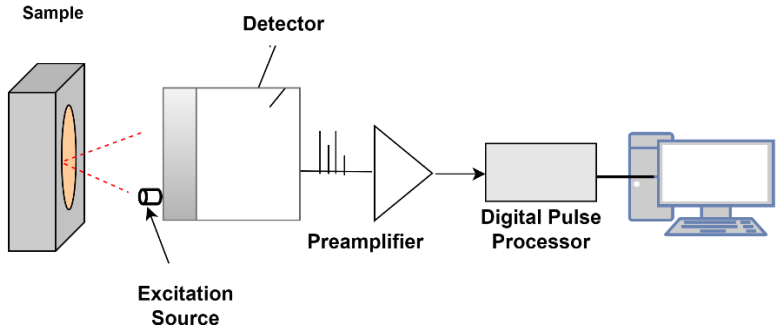

Figure 2: Experimental arrangement for measuring rat skin sample with PXRF system [3].

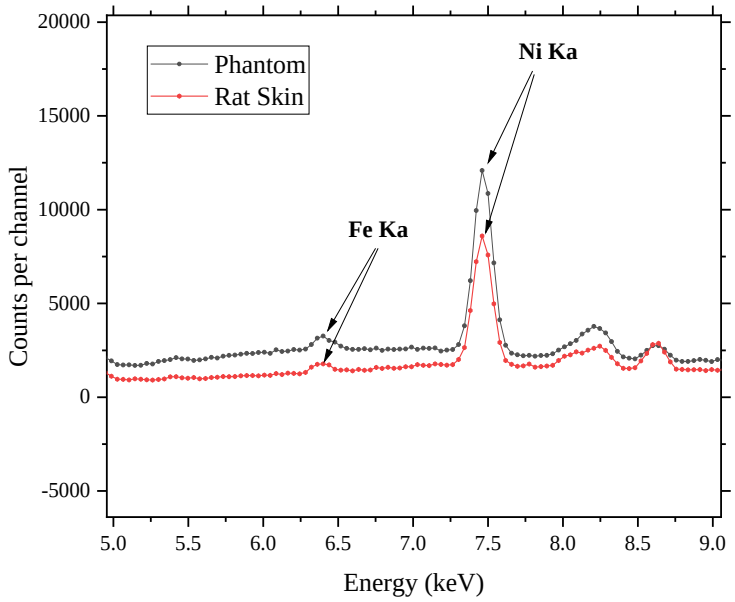

Figure 3: Comparison of a 10 µg Fe g^{-1} phantom spectrum with an individual rat skin measurement spectrum.

PXRF system ability to predict rat dosage level

The rats whose skin was measured in this study received different doses of injected Fe as previously summarised in Table 1. In order to determine whether the PXRF system can distinguish between the Fe levels of the different dose groups, t-tests were applied between groups with five or more than five animals. Testing was therefore performed for groups A,

B and C, who had received doses of 0, 80 and 160 mg $Fe^{2+,}$ respectively. Each rat group distribution was tested for normality using Anderson-Darling methods with a rejection level of p = 0.05. The mean of group B (83.4 ± 13.8 μg Fe g^{-1}) was found to be significantly higher than the mean of group A (10.7 ± 1.3 μg Fe g^{-1}), ($p < 0.003$) and the mean of group C (197.8 ± 7.2 μg Fe g^{-1}) was found to be significantly higher than the mean of group B, ($p < 0.0002$). The PXRF system was therefore able to distinguish between three different groups (each with 5 or more than 5 animals) with Fe dosage steps of 80 mg Fe^{2+} from 0 to 160 mg Fe^{2+}.

To further test the ability of the PXRF system to distinguish between Fe dosage levels, and to include data from dosage groups with less than 5 animals, a linear regression was performed of mean group PXRF measurement versus group Fe dosage level as shown in Figure 4. The measured skin Fe level was found to be strongly correlated with group dosage level (R^2 of 0.88) and increases by 1 μg Fe g^{-1} per mg of Fe dose. The regression is significant at the 95% confidence level (p=0.05).

The intercept was found to not be significantly different from zero: 5.1 ± 15.6 μg Fe g^{-1}. Using the variance data from t-tests, we can assume a standard deviation of approximately 30 μg Fe g^{-1} in the mean estimate of Fe content in a group of Fe dosed rats. This suggests that a group of five animals with mean skin levels of approximately 40 μg Fe g^{-1}) would be identified as being Fe dosed. This corresponds to a dose of 35 mg Fe^{2+}. A PXRF measurement can thus identify rat groups treated with Fe and distinguish them from a group of 'normal' animals even at the lowest doses measured in this study.

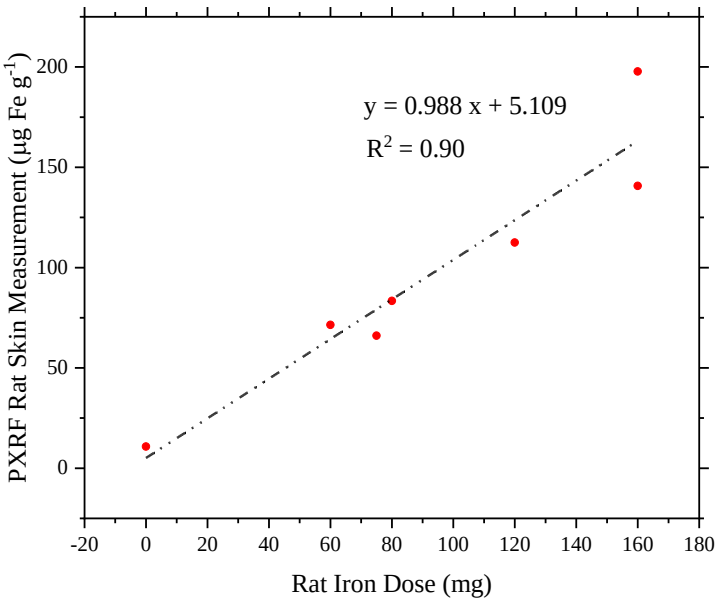

Figure 4: The plot of the regression of group average Fe concentration (µg Fe g^{-1}) measured in rat skin by PXRF versus rat-administered Fe dose in mg.

To test the ability of the system to determine whether an individual rat has been dosed with Fe, a regression was performed of individual rat skin Fe levels measured by the PXRF system in µg Fe g^{-1} against the Fe dose delivered to rats in mg Fe^{+2}. The plot of the regression is shown in Figure 5. The two variables were strongly correlated, R^2= 0.84, and the relationship was highly significant, p <0.0001. Like the correlations between group skin Fe and dosage levels, the slope predicts that individual rat skin Fe levels will increase by 1 µg Fe g^{-1} per mg of Fe dose. The intercept was 7.7 ± 9.2 µg Fe g^{-1}. This suggests that the PXRF system can determine whether an individual rat has been dosed with Fe, using this regression curve, if the skin level is above approximately 25 µg Fe g^{-1}. This equates to an Fe dose of 18 mg Fe^{2+}. The individual rat Fe dose prediction is better than the group prediction because the regression data for individual animals is more precise than the regression data for the groups. The system can identify whether a individual animal has Fe levels that are above 'normal' for all dose levels in this study.

PXRF system comparison to laboratory XRF system

The rat samples' skin Fe concentrations were measured with both a laboratory XRF system and the PXRF system with the laboratory system having been used in the prior rat dosing studies [13]. It had been found that measurements of Fe levels in skin samples using the laboratory system could be correlated to Fe levels in liver samples from the same animal. By comparing the ^{109}Cd PXRF skin estimates to the laboratory skin estimates, we can assess whether the PXRF measurements can be used as a surrogate for liver Fe measurement. The Fe/Ni ratio obtained for rat skin samples by the PXRF system was therefore regressed against the laboratory system Fe/Ni ratio from the same samples, as shown in Figure 6. The graph shows a strong linear correlation between the system measurements with R^2 of 0.85. The relationship is highly statistically significant ($p<0.0001$).

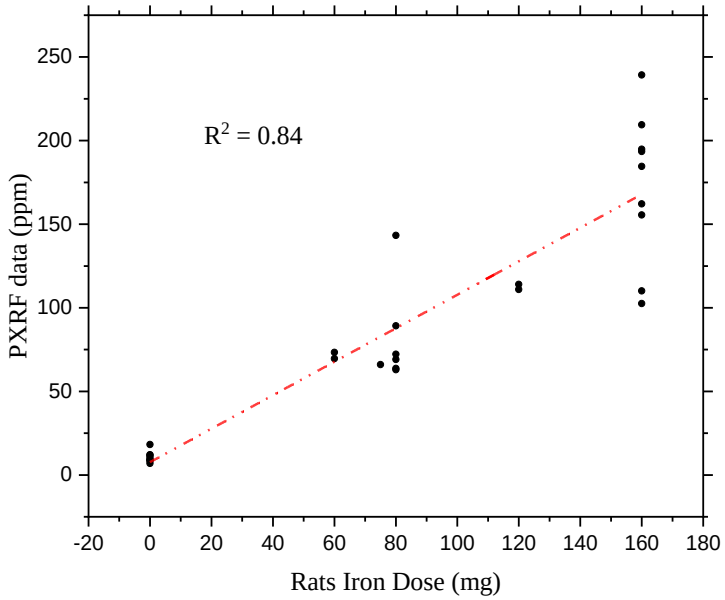

Figure 5: A plot of the regression of individual rat skin Fe concentration measured in μg g^{-1} by PXRF versus individual rat Fe dose administered in mg.

This initial regression analysis assumes that the laboratory XRF estimates have no or negligible measurement uncertainty, which is not valid. The uncertainties in the laboratory estimates are smaller than for the PXRF system estimates, but they are not negligible. To

assess the limits of the relationship, the laboratory XRF results were then regressed against the PXRF results and the equation rearranged to provide a relationship for the PXRF in terms of the laboratory XRF. The results are shown in Table 2 and the regression line can be seen in Figure 6. Neither regression has an intercept that is significantly different than zero, so there is no evidence of an offset in the relationship between the two systems. The results indicate a linear relationship between the PXRF and the laboratory skin Fe estimates and as the laboratory skin Fe estimates are correlated with the liver estimates, then the PXRF skin measurements are expected be correlated with the liver Fe levels in these animals. A measurement of elevated skin Fe level by the PXRF system can be assumed to be a surrogate measurement indicating elevated liver Fe levels in Fe dosed animals.

Regression	**Slope**	**Intercept**
Portable v/s laboratory	0.119 ± 0.010	0.038 ± 0.022
Laboratory v/s portable	0.172 ± 0.015	-0.021 ± 0.017

Table 2: The slopes and intercepts determined for the relationship PXRF versus laboratory XRF obtained from regressions of y and x and x against y.

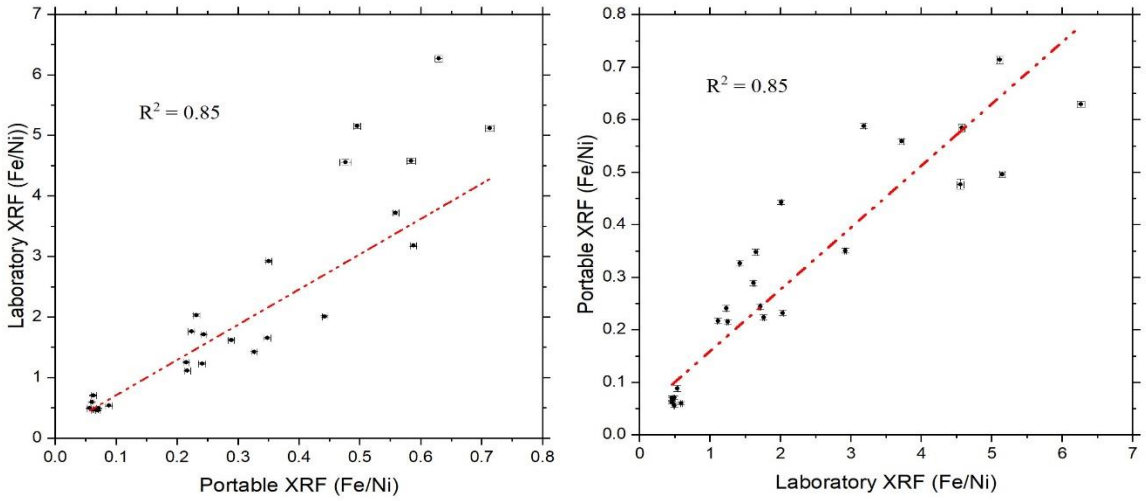

Figure 6: A plot of the regressions of the results of the PXRF system versus laboratory XRF system for rat skin Fe measurements. The regression was performed in both directions to account for the factor that both variables have uncertainties.

Discussion

The monitoring of Fe levels in real time is essential for clinical treatments such as chelation therapy, or phlebotomy, to deliver the best advantage to a patient from a treatment. The results of the *ex vivo* work indicate that the PXRF system shows potential not only for use in monitoring group levels in rats over time but is likely able to monitor changes in individual animals. However, the level at which the system can determine 'elevated' Fe in an individual rat *in vivo* will depend on the establishment of a strong set of baseline *in vivo* low Fe level data against which an individual rat's Fe level can be compared. The ability to determine the dose an animal received by a measurement of skin Fe alone, will depend on the establishment of a precise calibration line obtained from measurements in an *in vivo* study. This work shows that such a study may be worth undertaking.

However, the goal behind this work is to create a device for *in vivo* measurements in humans, not a pre-clinical system for studies in rats. Whether this work indicates potential in human measurements strongly depends on how well measurements of rat skin indicate the ability to measure levels in human skin. The question of whether these measurements

in rat skin are an indication of performance of this system in human measurements depends on how well rat skin matches human skin and whether the PXRF system measures the same layers of the skin in the two species.

Rat skin is notably thinner and more loosely attached compared to human skin and human skin is more complex than rat skin. However, the skin types do share fundamental similarities in structure and function. Rats and humans both have skin composed of layers: at the surface the stratum corneum, then the epidermis, dermis and hypodermis.

As previously discussed, there is some overlap in the thicknesses of the epidermis in rats and humans, and in some regions of skin, the thickness of the rat epidermis closely approximates that of human skin. For instance, the thickness of the epidermis on the feet of rats (ranging from 350 to 450 μm) is comparable to the average thickness of the epidermis on the human palm and soles of the feet (ranging from 300 to 400 μm) [6].

The stratum spinosum is present in humans as well as in the thick skin found in rats, such as the skin on their paws, esophagus, and stomach [5]. Keratinocytes within this layer continue to differentiate and undergo significant transformations, a process that is similar in both human and rat skin. The next layer, stratum granulosum, is clearly marked in rat skin. The primary function of this layer in both humans and rats is to produce certain lipids and proteins responsible for the maturation and waterproofing of the skin cells [6].

Beneath the basal layer lies the dermis, a layer of skin. There are few anatomical differences between the dermis of rats and humans, apart from their thickness. The dermis in both rats and humans consists of connective tissues and elastic fibres that provide strength to the dermis[16]. Both rat and human skin are equipped with nerve endings responsible for sensory perception. The dermis is also supplied with blood vessels to deliver nutrients and oxygen to the skin [6]. However, the density and distribution of blood vessels and nerve endings may be different in rat and human skin. The thickness of the dermis in human skin varies from 1 to 4 mm [17] depending upon the location of the skin, while it ranges from 0.1 mm to 3 mm in rat skin [16]. The boundary between the dermis and epidermis is not

flat in human skin; instead, it has downward epidermis extensions, known as rete ridges, that are absent in rat skin [18].

Our prior work shows that the ^{109}Cd PXRF system predominantly measures Fe at the surface layer of the skin. Differences between rat and human dermis are possibly less important than differences between rat and human epidermis. Rat and human epidermis show some overlap in skin thickness and structure.

However, it is not known whether the distribution of Fe in skin will be the same in rats and humans under conditions of both health and disease. Overall, studies of Fe distributions in skin are somewhat limited. There is some data on the distribution of Fe in human skin [19]–[24]. Several of these publications suggest that levels in the stratum corneum may depend on the health status of the person. Generally, they indicate that Fe is concentrated at the epidermal/dermal boundary in healthy individuals but may be increased in the epidermis and stratum corneum under conditions of disease such as psoriasis or eczema. Levels also increase in upper layers of the skin in patients with hemochromatosis, but the Fe distribution appears to depend on the treatment status of the patient. Our own work [25], utilizing synchrotron μXRF measurements to analyze Fe distribution in pig skin has shown increased levels of Fe in the superficial layers of the skin, with the thickness of the Fe layer being up to 100 μm thick (Figure 7).

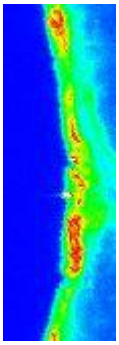

Figure 7. A 5 μm resolution μXRF map of Fe in the surface of pigskin diffused with saline. The skin surface is in the centre of the image and the scan moves deeper into the skin towards the right. The higher Fe layer is 80 to 100 μm thick.

Our simulations of Fe distributions in pig skin samples have suggested that when a high Fe layer is present at the skin's surface, the overall XRF signal predominantly measures the Fe concentration in the front layer, with lesser contribution from the lower Fe concentrations in the deeper layers [25].

If high Fe concentrations resulting from overload are localized at the skin's surface, it is plausible to infer that the overall thickness difference between human and rat skin would have a negligible impact on XRF results, and these rat skin measurements likely indicate that the PXRF system can distinguish between high and low Fe levels in humans. However further work in either a small human *in vivo* feasibility study or *ex vivo* skin studies will be required to validate this hypothesis.

Conclusion

A ^{109}Cd PXRF system for measurement of Fe in skin was found to be able to differentiate between normal and Fe overloaded rat skin samples. The system was both able to differentiate between the skin Fe levels of small groups of rats loaded with different levels of Fe and, further, identify whether an individual rat was from an Fe loaded or normal group based on measurement of skin Fe level. Rat skin Fe measurements using the ^{109}Cd PXRF system were found to be highly correlated with a laboratory XRF system which had determined that rat skin levels were correlated with liver Fe levels in Fe overloaded rats. The results indicate that the ^{109}Cd PXRF system measurements of skin Fe should be a surrogate measurement for elevated liver Fe levels in rats. Further work is required to verify the performance of the system in human populations.

References

[1] H.-W. Yuen and W. G. Gossman, "Iron Toxicity," *StatPearls*, Jun. 2022, Accessed: Apr. 27, 2023. [Online]. Available: https://www.ncbi.nlm.nih.gov/books/NBK459224/.

[2] M. J. Farquharson and A. P. Bagshaw, "Monitoring body iron burden using X-ray fluorescence (XRF)," *Radiat. Phys. Chem.*, vol. 61, no. 3–6, pp. 599–601, Jun. 2001, doi: 10.1016/S0969-806X(01)00344-9.

[3] S. U. K. Bangash, F. E. McNeill, M. J. Farquharson, and D. R. Chettle, "Feasibility of a 109Cd-based portable XRF device for measuring skin iron concentration in anaemic and β−Thalassaemic patients," *Biomed. Phys. Eng. Express*, vol. 8, no. 6, p. 065034, Nov. 2022, doi: 10.1088/2057-1976/AC9E02.

[4] M. Y. Wells *et al.*, "Histomorphology and Vascular Lesions in Dorsal Rat Skin Used as Injection Sites for a Subcutaneous Toxicity Study," doi: 10.1177/0192623309357953.

[5] R. L. Maynard and N. Downes, "The Skin or the Integument," *Anat. Histol. Lab. Rat Toxicol. Biomed. Res.*, pp. 303–315, Jan. 2019, doi: 10.1016/B978-0-12-811837-5.00024-1.

[6] P. M. Treuting, S. M. Dintzis, and K. S. Montine, "Comparative anatomy and histology : a mouse, rat and human atlas," p. 552.

[7] "Skin-Layer, Structure, and Functions." https://www.geeksforgeeks.org/skin/ (accessed Jan. 08, 2024).

[8] I. Youssry *et al.*, "Skin Iron Concentration: a Simple, Highly Sensitive Method for Iron Stores Evaluation in Thalassemia Patients," *http://dx.doi.org/10.1080/03630260701503833*, vol. 31, no. 3, pp. 357–365, Jul. 2009, doi: 10.1080/03630260701503833.

[9] M. J. Farquharson, A. P. Bagshaw, J. B. Porter, and R. D. Abeysinghe, "The use of skin Fe levels as a surrogate marker for organ Felevels, to monitor treatment in cases of iron overload," *Phys. Med. Biol.*, vol. 45, no. 5, p. 1387, May 2000, doi: 10.1088/0031-9155/45/5/320.

[10] H. Takeuchi *et al.*, "Usefulness of Rat Skin as a Substitute for Human Skin in the in Vitro

Skin Permeation Study," *Exp. Anim*, vol. 60, no. 4, pp. 373–384, 2011.

[11] S. Zaki Soliman Fakeeh Hospital, J. Cytol Histol, and S. Mohamed Zaki, "Characteristics of the Skin of the Female Albino Rats in Different Ages:Histological, Morphometric and Electron Microscopic Study Characteristics of the Skin of the Female Albino Rats in Different Ages: Histological, Morphometric and Electron Microscopic Study," *Artic. J. Cytol. Histol.*, vol. S, p. 3, 2015, doi: 10.4172/2157-7099.S3-004.

[12] N. M. A-F and M. Niczyporuk, "Rat skin in experimental medicine Received: 07.11," *Prog. Heal. Sci.*, vol. 8, no. 2, pp. 2018–223, 2018, doi: 10.5604/01.3001.0012.8351.

[13] D. A. Lintzeri, N. Karimian, U. Blume-Peytavi, and J. Kottner, "Epidermal thickness in healthy humans: a systematic review and meta-analysis," *J. Eur. Acad. Dermatology Venereol.*, vol. 36, no. 8, pp. 1191–1200, Aug. 2022, doi: 10.1111/JDV.18123.

[14] E. Dao, "X-RAY FLUORESCENCE MEASUREMENT OF IRON ACCUMULATION IN SKIN AS A SURROGATE MARKER FOR IRON LEVELS IN CRITICAL ORGANS AND TOTAL BODY IRON BURDEN," 2017, Accessed: Feb. 28, 2023. [Online]. Available: https://macsphere.mcmaster.ca/handle/11375/22121.

[15] S. U. K. Bangash, F. E. McNeill, M. J. Farquharson, and D. R. Chettle, "Feasibility of a 109Cd-based portable XRF device for measuring skin iron concentration in anaemic and β−Thalassaemic patients," *Biomed. Phys. Eng. Express*, vol. 8, no. 6, Nov. 2022, doi: 10.1088/2057-1976/AC9E02.

[16] M. N.-P. in H. Sciences and undefined 2018, "Rat skin as an experimental model in medicine," *Bibl. NiczyporukProgress Heal. Sci. 2018•bibliotekanauki.pl*, Accessed: Nov. 06, 2023. [Online]. Available: https://bibliotekanauki.pl/articles/1918822.pdf.

[17] H. PINKUS, "Anatomy of the skin.," *Dermatologica*, vol. 108, no. 1, pp. 37–59, 1954, doi: 10.1159/000256718.

[18] R. L. Maynard and N. Downes, "Anatomy and histology of the laboratory rat in toxicology and biomedical research," *Anat. Histol. Lab. Rat Toxicol. Biomed. Res.*, pp. 1–359, Jan. 2019, doi: 10.1016/C2016-0-02030-2.

[19] Y. Werner-Linde, J. Pallon, and B. Forslind, "PHYSIOLOGICALLY IMPORTANT

TRACE ELEMENTS OF PARALESIONAL PSORIATIC SKIN," *Scanning Microsc.*, vol. 12, no. 4, pp. 599–608, 1998.

[20] J. Pallon, K. G. Malmqvist, Y. Werner-Linde, and B. Forslind, "Pixe analysis of pathological skin with special reference to psoriasis and atopic dry skin.," *Cell. Mol. Biol. (Noisy-le-grand).*, vol. 42, no. 1, pp. 111–118, Feb. 1996, Accessed: Dec. 13, 2023. [Online]. Available: https://europepmc.org/article/med/8833672.

[21] P. Moretto, J. E. Surleve-Bazeille, D. Lieu, C. Michelet, and P. Stoedzel, "Microanalysis of the human skin structure: preliminary results," *Nucl. Instruments Methods Phys. Res. Sect. B Beam Interact. with Mater. Atoms*, vol. 158, no. 1–4, pp. 386–392, Sep. 1999, doi: 10.1016/S0168-583X(99)00346-8.

[22] Y. Inoue *et al.*, "ZIP2 protein, a zinc transporter, is associated with keratinocyte differentiation," *J. Biol. Chem.*, vol. 289, no. 31, pp. 21451–21462, Aug. 2014, doi: 10.1074/jbc.M114.560821.

[23] I. Guinote *et al.*, "Using skin to assess iron accumulation in human metabolic disorders," *Nucl. Instruments Methods Phys. Res. Sect. B Beam Interact. with Mater. Atoms*, vol. 249, no. 1–2, pp. 697–701, Aug. 2006, doi: 10.1016/J.NIMB.2006.03.120.

[24] T. Pinheiro *et al.*, "Distribution and Quantitation of Skin Iron in Primary Haemochromatosis: Correlation with Total Body Iron Stores in Patients Undergoing Phlebotomy," *Acta Derm. Venereol.*, vol. 94, no. 1, pp. 14–19, 2014, doi: 10.2340/00015555-1601.

[25] S. U. K. Bangash *et al.,* "Investigation of the Accuracy of Portable ^{109}Cd XRF system for the Measurement of Iron in Skin" unpublished.

Chapter 5

Conclusions and Future Work

In this thesis, I modified and developed an XRF-based detection system to measure skin Fe concentration accurately in animal models of both normal and Fe overloaded states. The thesis is divided into three papers, collectively fulfilling the project's overall expectations. The thesis begins with investigations concentrated on the development of a PXRF system, the creation of phantoms, a dosimetry study, and the calculation of the system's MDL in Paper I. Additionally, information is presented that shows the backscattered signal from phantoms is significantly influenced by the position and distance of the phantom from the detector. This effect, which potentially alters measured Fe levels, is rectified through the normalization of Fe K_α X-rays to Ni K_α X-rays. Paper II focuses on validation of the accuracy of the system through measurements of pig skin samples. The study also involves an investigation into the distribution of Fe in normal skin samples, and the impact of inhomogeneous Fe distribution on the measured XRF signal is examined through Monte Carlo simulation. Paper III is a preclinical study conducted on skin samples of rats loaded with varying amounts of Fe, focusing on the ability of the system to distinguish between Fe dosed and non-dosed animals and correlation of our XRF system measurements against those of a laboratory benchmark system. The study demonstrates the system's capability not only to classify animals to Fe overload conditions but also to potentially predict the dosage level of Fe.

This thesis has initiated the exploration of numerous questions regarding the distribution and measurement of Fe in the skin. However, certain areas remain unresolved and

necessitate further research, primarily due to the limited scale of the studies conducted thus far, which exclusively focused on animal skin.

The upcoming section outlines potential research areas to enhance the XRF detection system. It aims to offer insights into measuring Fe levels in the skin of patients with beta thalassemia and hemochromatosis. The chapter concludes with an overall summary.

5.1 Future Improvements in PXRF System Performance

5.1.1 Selection of Excitation Source

The system achieved an excellent detection limit but for a measurement time of 1800 s. The goal of the work is to use the system in clinics, and this time is too long for a point-of-care measurement. For the system to be useful in a hematology clinic, results will need to be almost immediate. In addition, the measurement time can be a significant concern for patients who may feel anxiety and mild discomfort from holding still during the measurement. The system needs to be further developed to have a reduced measurement time.

This measurement time could be reduced by using a higher activity spot ^{109}Cd source or a combination of sources or as a ring source. The system would need to be recalibrated, and the effects of dead-time, throughput and system settings will need to be thoroughly investigated. Faster electronics could help with a more active source. The, ^{109}Cd ‘spot’ sources as used in this thesis work can be difficult to purchase and are expensive. The small ‘spot’ sources cost approximately 24,000 CAD and need to be replaced every three years. Alternative sources could be investigated, such as ring sources which are easier (and thus cheaper) to manufacture.

^{109}Cd is utilized to excite Fe atoms in both phantoms and animals' skin, specifically in this thesis in rats and pigs. The decay scheme of ^{109}Cd is detailed in Chapter 1, subsection 1.5.5.1. The primary photon energies emitted by ^{109}Cd that are used for XRF excitation are the Ag X-rays at 22 keV and 24.9 keV. The photoelectric cross-section for these excitation

energies in relation to Fe is approximately 19 $cm^2 g^{-1}$ for 22 keV and 15 cm^2g^{-1} for 24.9 keV. The K shell absorption edge for Fe is at 7.1 keV. The magnitude of the photoelectric cross-section at the absorption edge is approximately 406 $cm^2 g^{-1}$. By employing a lower excitation energy, ideally slightly higher than the Fe K-edge, the probability of interaction with the Fe atoms can be increased. This increased probability of the photoelectric effect amplifies the generation of Fe characteristic X-rays, consequently enhancing the sensitivity and detection limits of the instrument. This improvement may also contribute to a better signal-to-noise ratio, facilitating the detection and quantification of Fe in the sample. While ^{241}Am (13.76 and 13.95 keV), ^{244}Cm (14.28 keV), and ^{238}Pu (11.62, 13.44 and 13.62 keV) could be promising candidates as excitation sources as their excitation energies are close to K-edge of Fe atoms, factors such as source availability, purchasing cost, safe handling, and dose estimation would have to be considered.

5.1.2 Measurement of Inhomogeneous Fe Distribution in Skin

The water-based phantoms utilized in the calibration of this XRF instrument have a uniform distribution of Fe. However, the creation of non-homogeneous phantoms will be essential for a more accurate simulation of the inherent variability in Fe distribution within the skin. These non-homogeneous phantoms would have to be developed with layered concentrations of Fe at different depths within the skin. This could involve simply varying the concentration of Fe exponentially and/or linearly with depth to investigate its impact on the overall XRF signal.

5.2 Pre-Clinical Measurements

In the validation study presented in this thesis, the assessment of Fe concentration in pig skin utilized specimens likely obtained from the same herd, without exposure to excessive Fe loading. Therefore, it could be beneficial to extend the research by conducting a further study using pig skin from animals under Fe overload.

To enhance the comprehensiveness of the study, various breeds of pigs could be incorporated. This approach will allow the exploration of trends in Fe distribution among

different breeds with potentially different skin thicknesses. By establishing correlations between Fe distribution trends in cases of Fe overload and the XRF Fe measurements, it may be possible to identify potential correction factors if the distribution differs from that in normal skin.

After animal measurements, the first step in in in vivo testing of biomedical devices in humans is to conduct a safety and feasibility test to determine the best set-up and safety design for in vivo measurements as phantom and human measurements can be very different in practise. For example, phantoms do not move, and a device may need to be developed to hold a human in place and to avoid touching and damaging the detector window. After this initial testing, the system should proceed to measurement of skin Fe concentration in a small cohort of volunteers who have undergone blood tests in clinical settings. Both the initial safety testing and the small cohort Fe measurements would necessitate approval from an ethics review board such as the Hamilton Integrated Research Ethics Board (HiREB), and full consent would be required from the participating volunteers and/or patients. The study of a small cohort of patients whose blood information was made available would allow testing of whether measured skin Fe concentrations from this group of patients are correlated with their levels of hemoglobin and ferritin. Testing whether skin Fe correlates with liver Fe levels in patients would require a riskier study that would incorporate biopsies to measure patients' liver Fe concentrations. This comprehensive approach would enable a more thorough understanding of the relationship between skin Fe levels and various physiological markers.

5.3 Clinical Measurements

After measuring volunteers, this system could be utilized in a clinical trial in a clinical setting for patients suffering from Fe overload or Fe deficiency. At present, the system performance suggests that skin Fe levels in patients with Fe overload may be possible. The XRF skin Fe measurement could be conducted before starting phlebotomy, and subsequent measurements could be undertaken at various stages of the therapy. This approach would aid in understanding the pattern of skin Fe levels over time and potentially the effectiveness

of the treatment at different stages of the disease by comparing the results of skin Fe measurements with those obtained from the patient's liver biopsy. This comparative analysis could enhance the understanding of the correlation between skin Fe and liver Fe concentrations at different disease stages, thereby assisting healthcare professionals in optimizing therapy. The same approach is applicable to chelation therapy in cases of beta thalassemia.

The application of radioisotope based XRF systems in clinical settings will necessitate careful consideration of safety measures, stemming from the utilization of a radioisotope to excite Fe atoms in the skin in an area with significant patient and staff traffic. It is imperative to minimize potential exposure to the general public and staff resulting from the radiation emitted by the radioactive source. To ensure the safe handling of the source, staff involved in measurements will require comprehensive training. This training is essential not only for the proper execution of the measurements but also to mitigate any risks associated with the use of radioactive materials. As such, a thorough understanding of safety protocols will be crucial to guarantee the well-being of both clinicians and patients involved in the XRF procedures.

Finally, as the system progresses toward clinical measurements, a more friendly user interface will be required to make for simpler measurements by healthcare professionals. The XRF system currently serves as a tool for physicists to conduct elemental analysis. This process involves exciting the sample, with the resulting outcomes presented on the screen as a spectrum. Analyzing this spectrum is typically a complex task, and healthcare professionals will not possess the necessary training nor have the time for the analysis. To enable the use of the system in clinical settings, it will be crucial to design a user-friendly interface. This interface will need to allow health professionals to interact with the system effortlessly, removing the need for them to understand the complex technical details of spectral analysis. To facilitate this, a computer programming code needs to be developed. This code should be designed to handle the raw spectrum, extracting the necessary significant information. Tasks would include identifying peaks corresponding to specific elements and determining their concentrations. The code would then transform this

processed data into an easily readable format, presenting the concentration of elements in a clear and understandable manner and in the context of the likely health implications for the patient.

5.4 Study Limitations

The findings presented in Paper II suggest that a PXRF detection system is viable for measuring skin Fe concentration in normal, healthy pig skin samples. This study, however, suggests that Fe is not evenly distributed in the skin; instead, it exhibits a high concentration near the outer surface of the epidermis. It is important to note that this investigation focused on a specific breed of animal, and it remains uncertain whether the distribution of Fe would be consistent across all animal breeds. Additionally, the testing of the PXRF system was limited to normal and Fe overloaded conditions in *ex vivo* measurements.

Due to time constraints and the need for approval from the Human Research Ethics Board (HiREB), *in vivo* measurements on human skin were not performed for the work in this thesis. Consequently, there is a chance that the distribution of Fe in human skin under normal and Fe overload conditions may vary compared to *ex vivo* measurements on animal skin samples.

5.5 Conclusions

The assessment of skin Fe concentration through XRF for monitoring Fe levels in individuals with beta thalassemia and hemochromatosis is an expanding field of study. A PXRF system has been developed, demonstrating enhanced detection limits, better performance in phantoms, accuracy in measuring both normal and Fe overloaded skin samples and an ability to distinguish skin samples from normal and Fe loaded rats. The system accuracy is verified against established commercial system that trace back to national standards. In conclusion, the original objectives outlined at the start of this thesis have been achieved, and the developed XRF system proves effective for the non-invasive measurement of skin Fe concentrations in samples from animals with Fe overload and thus

shows potential for measurement of Fe levels in humans with Fe overload disease. Moreover, the system has the potential to be utilized in assessment of Fe deficiency due to its low detection limit. Thus, this system holds promise for clinical applications, addressing current inquiries and contributing to the understanding of Fe distribution in human skin.